

POLITECNICO DI TORINO

Corso di Laurea Magistrale
In Ingegneria Meccanica

Tesi di Laurea Magistrale

Experimental investigation of PCM thermal energy storage system for office ventilation



Relatore

Prof. Marco Carlo Masoero

Correlatore

Prof. Uroš Stritih

Candidato

Daniele Dominici

A.A.2017/2018

ABSTRACT

The air heating for residential ventilation concerns a significant part of the energy consumption in buildings. Nowadays a high boost in favor of more efficient and sustainable energy systems is being recorded. This work wants to analyze a new system conceived for office ventilation. The system, installed at the Faculty of Engineering in Ljubljana, is composed of a solar air collector and a latent heat thermal energy storage unit which, in turn, is constituted by phase changing material plates. The system has been designed to carry out experiments and to verify savings that could be obtained for space ventilation. Analogue systems, for different purposes and applications, have been studied by other researchers and a quick review is initially carried out in Chapter 1. Once, operating principles and the elements that compose the system are described, the results obtained through temperature and velocity measurements are reported. Chapter 2 ends with a further experiment in a hypothetical operating time of the ventilation system with an overall analysis of the system performances. In order to evaluate the behavior of the system throughout the heating season a TRNSYS software simulation tool was used. The model of the storage was implemented at Brno University of Technology. In Chapter 3, data obtained through experimentation is compared with the results of the simulated system in TRNSYS with the purpose of validating the results of the software. Validation is carried out either for the PCM system and for the solar air collector. Once the results were validated, the annual simulations of the system were carried out to verify the possible improvements and thus, the energy savings. The behavior throughout the overall heating season was evaluated also after the integration of an air recuperator in the system in order to compare the results with those of the previous layout and hence, to analyze whether this addition was positive or not.

NOMENCLATURE

GDP	Gross Domestic Product
IEA	International Energy Agency
EPBD	European Performance of Buildings Directive
TES	Thermal Energy Storage
PCM	Phase Change Material
MEPCM	Microencapsulated Phase Change Material
FPSAH	Finned Plate Solar Air Heater
ICS	Integrated Collector Storage
FMHPA	Flat Micro-Heat Pipe Array
HST	Heat Storage Tank
HIM	Heat Insulation Material
HTF	Heat Transfer Fluid
SAC	Solar air collector
PMMA	Polymethylmethacrylate
EPS	Expanded Polystyrene
CSM	Compact Storage Modules
TISS	Thickness Insensitive Spectrally Selective
MAE	Mean Absolute Error

CONTENTS

CHAPTER 1 INTRODUCTION TO PCMS WITH SOLAR AIR COLLECTORS	1
1.1 LATENT HEAT THERMAL ENERGY STORAGE SYSTEMS FOR ENERGY SAVINGS IN BUILDINGS.	1
1.2 PCM PROPERTIES FOR LHTES SYSTEMS.....	2
1.3 CLASSIFICATION OF PCMS.....	4
<i>1.3.1 Paraffins</i>	5
1.4 PCM: ENCAPSULATION.	6
1.5 PCM APPLICATIONS.....	7
<i>1.5.1 PCMs in building envelope</i>	7
<i>1.5.2 Solar collector with LHTES usage</i>	9
CHAPTER 2 EXPERIMENTAL INVESTIGATIONS	20
2.1 INTRODUCTION TO THE SYSTEM INSTALLED AT THE UNIVERSITY OF LJUBLJANA.	20
2.2 HEATING AND COOLING OPERATION MODE OF THE SYSTEM.....	21
<i>2.2.1 Charging and discharging period in the heating mode</i>	23
2.3 DESCRIPTION OF THE ELEMENTS OF THE EXPERIMENTAL SET-UP.	24
2.4 TEMPERATURE MEASUREMENTS.	29
<i>2.4.1 Temperature measurements from 30/11/2017 to 5/12/2017</i>	31
2.5 VELOCITY MEASUREMENTS.	34
<i>2.5.1 Velocity measurements in the duct center</i>	34
<i>2.5.2 Velocity measurements along the duct cross section</i>	39
2.6 SYSTEM ANALYSIS DURING VENTILATION TIME.	43

CHAPTER 3 TRNSYS SIMULATIONS OF THE SYSTEM.....	54
3.1 INTRODUCTION TO TRNSYS SIMULATION ENVIRONMENT	54
3.2 THE NUMERICAL MODEL OF THE LHTES UNIT.	54
3.3 PROFORMA OF TYPE256 TRNSYS COMPONENT.....	60
3.4 THE NUMERICAL MODEL OF THE SOLAR COLLECTOR.....	62
3.5 PROFORMA OF TYPE1B FLAT-PLAT SOLAR COLLECTOR COMPONENT	64
3.6 VALIDATION OF THE LHTES UNIT MODEL.	65
3.7 VALIDATION OF THE SOLAR AIR COLLECTOR.	69
3.8 ADDITION OF AN AIR RECUPERATOR IN THE SYSTEM.	72
3.9 ANNUAL SIMULATIONS.....	79
3.9.1 Results.....	81
CHAPTER 4 FINAL CONCLUSIONS	93
4.1 CONCLUSIONS.....	93
REFERENCES.....	96

Chapter 1

Introduction to PCMs with solar air collectors

1.1 Latent heat thermal energy storage systems for energy savings in buildings.

Over the last few years there has been a growing interest in reducing energy use in buildings in contrast with the rapid economic growth worldwide that has led to an increase in the supply of the overall energy consumption. Globally, gross domestic product (GDP) increased by more than 95% from 1990 to 2015, whereas total primary energy supply grew by 56% [1]. In 2014, in the International Energy Agency (IEA) member countries, the residential sector accounted a share of 19% of overall energy consumption and space heating accounted for over half of the energy consumption in the residential sector [1], as shown in Figure 1.

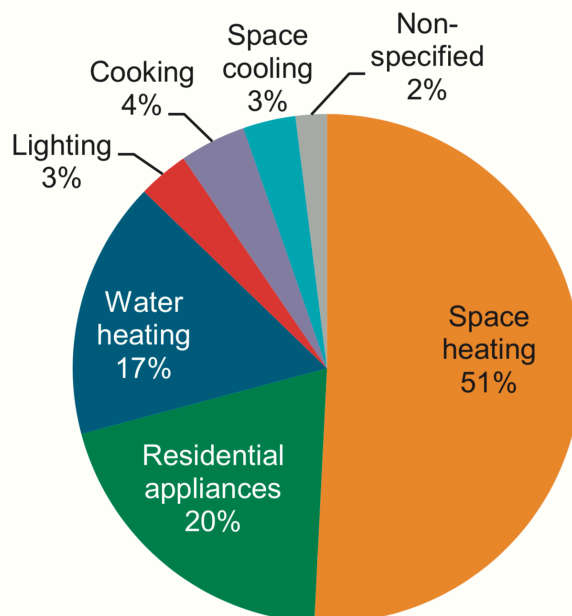


Figure 1. Shares of residential energy consumption in 2014 for IEA members [1].

From this it can be noted how it is important to find new ways to improve building energy efficiency. To curb the energy consumption of the building sector the European Union through the European Performance of Buildings Directive (EPBD) established that Member States shall ensure by 31 December 2020 all new buildings should be nearly zero-energy buildings. Nearly zero-energy buildings have very high energy performance and the low amount of energy that these buildings require comes mostly from renewable sources. To reduce the space heating energy consumption of a building, the most direct and effective way is improving the building envelope performance and the efficiency of building energy consumption system. Thermal energy storage (TES) represents a good solution for this issue. TES using phase change material (PCM) is called latent heat thermal energy storage (LHTES). The latter plays a very important role when energy required and supplied are not equal and is an efficient way to conserve the waste heat and the excess energy available of a form of renewable energy such as solar energy. Excess energy available in the off-peak time can be stored in the TES devices for later use. For example, solar energy is available only during sunshine hours, thus, the excess heat may be stored during the day and used later during the night. Unlike conventional storage materials that stored only sensible heat (their temperature rises as they absorb heat), PCMs absorb and release heat at a nearly constant temperature during phase change and this allows to increase the efficiency of heat exchange and to increase by 3-4 times the energy storage density respect to sensible devices in the temperature increment of 20 °C [2] and by 5-14 times than sensible storage materials such as water, masonry, or rock [3].

1.2 PCM properties for LHTES systems.

Below are listed the properties that PCM should have to be used as thermal storage system [4].

Thermal properties:

- suitable phase change temperature. Phase change temperature of PCM should be chosen according to the operating temperature of the system;
- high specific heat. It regards the sensible heat exchanged, and the more is high the more heat is transferred at the same temperature difference;

- high latent heat. It is the amount of energy exchanged during PCM phase transition and a large value of latent heat allows to decrease the volume and so the physical size of the storage;
- high thermal conductivity in liquid and solid phase. It favors the heat flux exchanged and high value should be found to minimize the temperature gradient required for the melting and freezing of PCM.

Physical properties:

- high density. It allows to decrease the size of the storage casing;
- no or small subcooling during freezing. It avoids finding a temperature range during freezing of the PCM and so gives a single value of phase change transition temperature. Subcooling can be suppressed by using a nucleating agent in the PCM;
- low vapor pressure and small volume change. Low values of vapor pressure and volume change help to reduce the containment problem.

Chemical properties:

- prolonged chemical stability. It permits to make continuous freezing and melting cycles maintaining the chemical composition of the PCM;
- compatible with capsule material. PCM doesn't have to react with the construction materials that composed the encapsulation;
- non-toxic, non-flammable, and non-explosive.

Economic properties:

- abundantly available;
- inexpensive.

1.3 Classification of PCMs

Abhat [5] has done a global classification of phase change materials as shown in Figure 2.

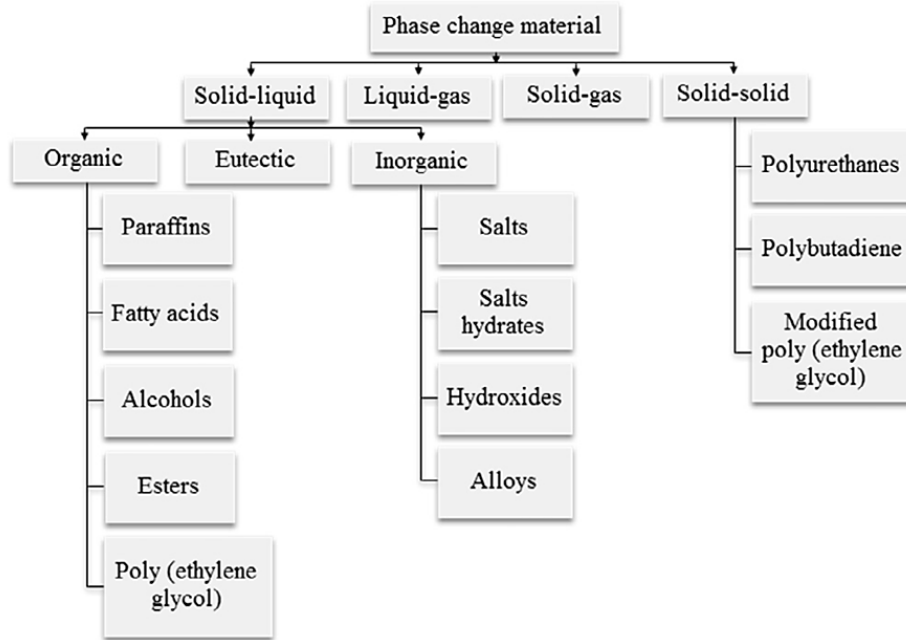


Figure 2. Classification of phase change materials [4].

They are majorly classified as organic, inorganic, and eutectic.

The organic PCM's are the most suitable materials for cooling/heating of building thanks to their congruent melting property without phase segregation over the large number of melting/freezing cycles at the cost of degrading latent heat of fusion and do not suffer from subcooling. On the other hand, organic PCMs have low thermal conductivity ($0.1-0.3 \text{ W m}^{-1} \text{ K}^{-1}$), therefore techniques to increase it have been studied such as dispersion of high conductivity solid particles (micro/nano size) in the PCM [6], insertion of metal matrices [6], chunks of metal (stainless steel and copper) pieces [7], carbon fibers [8], and impregnation of porous graphite matrix in the PCM [9].

Inorganic materials can be further classified as salt hydrate and metallic and they are characterized by high latent heat per unit volume ($\sim 350 \text{ MJ / m}^3$), value of thermal conductivity relatively high ($\sim 0.5 \text{ W m}^{-1} \text{ K}^{-1}$), lower costs in comparison to organic compounds, and are non-flammable. However, they suffer of decomposition and

subcooling and melt incongruently. To overcome the subcooling, thickening agents as Bentonite clay and nucleating agent as Borax are embedded with inorganic materials but they have a negative impact on thermal conductivity.

A eutectic is a minimum-melting composition of two or more components, such as organic-organic, organic-inorganic, inorganic-inorganic, each of which melts and freeze congruently forming a mixture of the crystal components during crystallization.

1.3.1 Paraffins.

Paraffin or paraffin wax is a mixture of straight n -alkanes which is presented by the chemical formula C_nH_{2n+2} , where $20 \leq n \leq 40$. The melting temperature of these compounds increases with increase of number of alkane chains in the molecules [10]. Thermo-physical properties of some paraffins are reported in Table 1. Paraffins display no phase segregation even after many phase transition cycles and no supercooling is presented. Paraffins are safe, reliable, durable, predictable, available abundantly, inexpensive, non-toxic, chemically inert and stable below 500 °C. Furthermore, paraffin mixtures in different mass proportion have a wider phase change temperature range and higher phase change latent heat and this allows a more elastic use of them in different thermal storage fields by adjusting the mixed proportion. These are the reasons why paraffin is the most widespread material in TES systems.

Compound	Melting Temperature [°C]	Latent heat [kJ/kg]	Specific heat [kJ/kg K]	Thermal conductivity [W/m K]	Density [kg/m ³]	Ref.
Paraffin C14	4.5	165	-	-	-	[5]
Paraffin C15-C16	8	153	2.2 (s)	-	-	[5]
Paraffin C16-C18	20-22	152	-	-	-	[11]
Paraffin C13-C14	22-24	189	2.1	0.21	790(l)	[11]
Paraffin C18	28	244	2.16	0.15	814	[5]
Nonadecane	32	222	-	-	785	[12]
Heneicozane	40.2	213	-	-	791	[12]
Paraffin C20-C33	48-50	189	2.1	0.21	769(l)	[5]
Paraffin C22-45	58-60	189	2.1	0.21	795(l)	[5]
Paraffin C23-C45	62-64	189	2.1	0.21	0.915	[5]
Paraffin wax	64	173.6	-	0.167(l)	790(l)	[13]
Biphenyl	71	119.2	-	-	994(l)	[13]
Propionamide	79	168.2	-	-	-	[13]
Tridecane	-5.4	196	2.21(l)	-	753(l)	[10]

Table 1. Thermo-physical properties of some paraffins used as thermal storage [4].

1.4 PCM: encapsulation.

Encapsulation is a technique that allows to keep together the material in an enclosed volume to avoid direct contact between the PCM and the environment, to prevent the leakage of the PCM when it is in liquid phase, and to increase the heat exchange surface. There are two type of encapsulation: micro and macro encapsulation. The first is a technique in which large number of PCM particles of 1-1000 μm diameter are enclosed in a solid shell and keep together in a continuous matrix. There are numerous techniques adopted for microencapsulation such as coacervation, suspension, emulsion, condensation, and polyaddition polymerization [4].

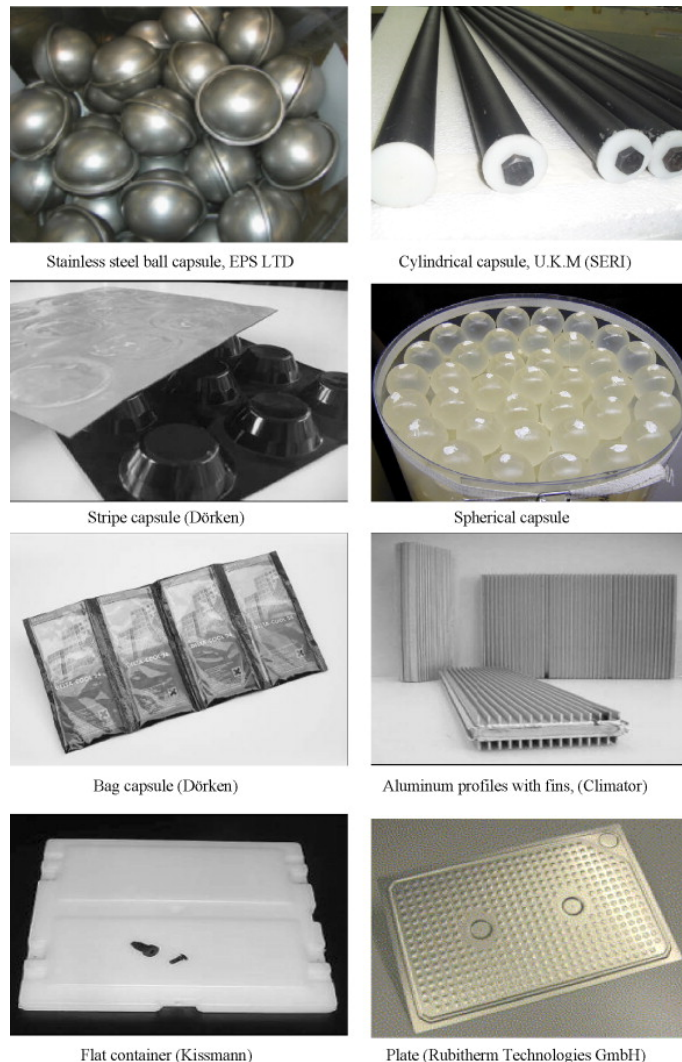


Figure 3. Photographs of macro encapsulation of various geometry [14].

Microencapsulated phase change materials (MEPCMs) possess characteristics like uniform diameter, thermal stability, shell mechanical stability, and penetration abilities. On the other hand, they are characterized by low heat transfer rates due to low thermal conductivity of matrix materials and suffer from evident subcooling phenomenon and are relatively expensive.

Macro encapsulation consists in filling the PCM in macroscopic containment and allows to obtain a various shapes and sizes that give to PCM mechanical stability if the casing is sufficiently rigid. Figure 3 shows some macro encapsulated PCMs in containers and bags made of metal or plastic.

1.5 PCM applications.

Storage of heat or cold is necessary to match availability and demand with respect to time. The energy stored in peak time can be released during off-peak time. When heat is automatically stored or released, depending on indoor or outdoor temperature rises or falls beyond the melting point, a passive system is defined while heat or cold is used only on demand, not automatically, in active systems and for the latter a thermal insulation is required.

PCMs are used in a lot of applications like cooling and heating the buildings, cooling electronic devices, domestic-commercial refrigeration, textile industry, dryer and food packaging.

1.5.1 PCMs in building envelope.

The principle followed in embedding PCM in building envelope, becoming a part of wall structure, is to result a building wall with a large thermal inertia without the large mass that normally would need. As an example, a new construction material composed of gypsum board containing PCM 45 wt% was prepared by Oliver [15]. It was found that a 1.5 cm-thick board of gypsum with PCMs stores 5 times more thermal energy as a 12 cm-thick brick wall within the comfort temperature range (20-30°C). Feldman et al. [16] studied the thermal behavior of PCM impregnated wallboard and observed that its total energy storage capacity in the temperature range of 23-26.5 °C is at least twelve times higher than normal wallboard without PCM.

EM Alawadhi and HJ Alqallaf [17] studied a building roof with conical holes containing PCM to reduce the cooling load by absorbing the incoming energy through the melting process in the roof before the energy reaches the indoor space. The results indicated that the heat flux at the indoor surface of the roof can be reduced up to 39% when the PCM is introduced in the roof.

Yanbing et al. [18], Stritih and Butala [19] analyzed a “free-cooling system” using PCM Packed Bed Storage (Figure 4) and PCM impregnated ceiling board, respectively. The basic principle of free-cooling is divided in two steps; during the night, the cold outside air is blown by the fan through the storage system on the ceiling that stores cold from the air and during the day the blown air is cooled by the storage and then supplied to the room.

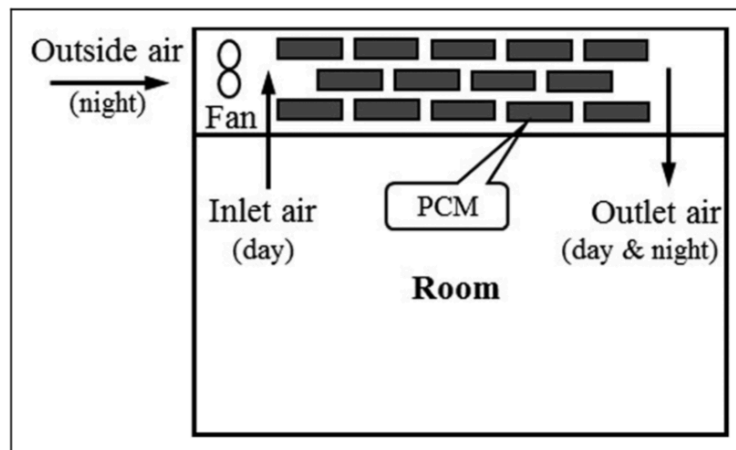


Figure 4. Scheme of the free-cooling system proposed by Yanbing et al.[18].

Floor heating is interesting because may provide high indoor comfort and small indoor temperature fluctuation than convective heating systems. Lin et al. [20], Tsinghua University, Beijing, China, analyzed the thermal performance of a under-floor electric heating system, shown in Figure 5, with a shape-stabilized PCM plates. The system is charged during the night by using cheap electricity and is discharged during the day to heat the room.

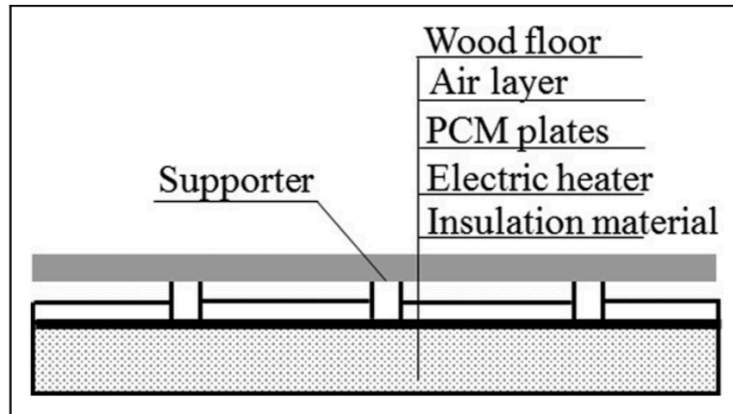


Figure 5. Layers of the under-floor electric heating system [20].

1.5.2 Solar collector with LHTES usage.

LHTES is one of the most efficient way to store energy from a source intermittent such as the solar one. Energy storage process can reduce the mismatch between energy supply and energy demand. Many studies have been carried out and systems with solar air collector and LHTES integrated or separated can be found.

1.5.2.1 Natural circulation solar air heating with PCM as energy storage.

S.O Enibe presented the design, construction and performance valuation of a passive solar powered air heating system, shown in Figure 6, installed in Nsukka, Nigeria, which has potential applications in crop drying and poultry egg incubation [21].

For this kind of applications hot air is to be supplied over a continuous period of several days, including off-sunshine hours and so a form of energy storage, like PCM, is required.

The system was composed by a flat plate solar collector integrated with the heat storage system composed by thin rectangular PCM modules (Figure 7). The rectangular walls that constituted the rigid structure of PCM encapsulation behaved like thin fins. They were made with good thermal conductivity's material. Modules were positioned in equal distance from each other. Air entered through valve A was being heated passing through the space between PCM module pairs and by natural convection flowed through valve B and through the hot air chamber and it was discharged to the environment through valve C. The single-glazed collector of area 1.503 m^2 had a steel absorber plate coated with a non-selective absorber material. The

melting temperature range of the paraffin wax was 58-60 °C, the specific heat 0.9 kJ kg⁻¹ K⁻¹ and thermal conductivity 0.2 W m⁻¹ K⁻¹. The daily global irradiation covered the range between 4.91 and 19.96 MJ m⁻², while the ambient temperature over the period varied within the range 19.6 and 41.8 °C.



Figure 6. Photograph of the system. A, solar air collector and energy storage; B, heated space[21].

It was found that the absorber plate temperature generally varied in sympathy with the global irradiance. The same happened with PCM walls temperatures but more sluggishly in comparison with the absorber plate temperature. This was due to significant heat exchange between plates and PCM. Furthermore, a significant temperature gradient along the vertical side of PCM module walls was found, with temperature peak values lower by about 20-30 K in respect to absorber plate. The airflow rate, as expected, increased its value gradually as the collector heated up from sunrise and fell off as solar irradiance decreased. It was also observed that efficiency increased its value with high solar irradiation and a peak of 50% was observed.

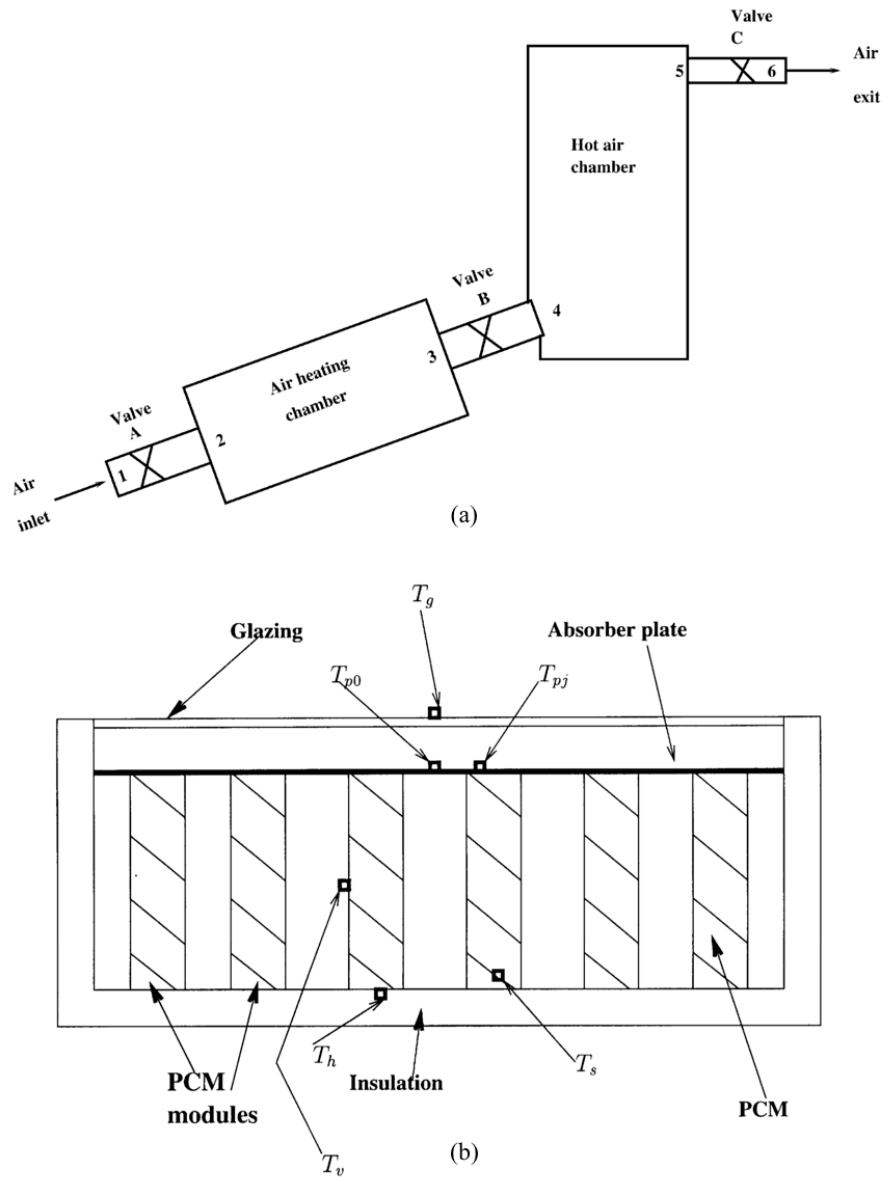


Figure 7. (a) Schematic view of a natural circulation air heater. (b) Cross section of solar air collector with PCM rectangular modules [21].

1.5.2.2 Solar wall collector with PCM.

Pisut Thantong and Preeda Chantawong carried out experimentation about performance of a solar wall collector with PCM toward the natural ventilation of two model houses [22]. Houses, with the same volume of 4.05 m^3 , were built on the attic of Building 65 in the College of Industrial Technology, North Bangkok. Solar air collector-PCM wall system was installed into the south facade of Home 1 and Home 2 was made only by single concrete walls so that to compare the results.

The passive system was composed of a solar wall collector with PCM panel, an air gap, and an inner wall made of concrete material. One of the two opening areas was located at the bottom, that connects the internal environment through the wall chimney, and the second in the upper part which leads air outdoor. The solar collector-PCM wall was 1.40 m high and 0.80 m width and had a similar thickness to that of internal concrete wall of 15 cm. The system is shown in Figure 8.

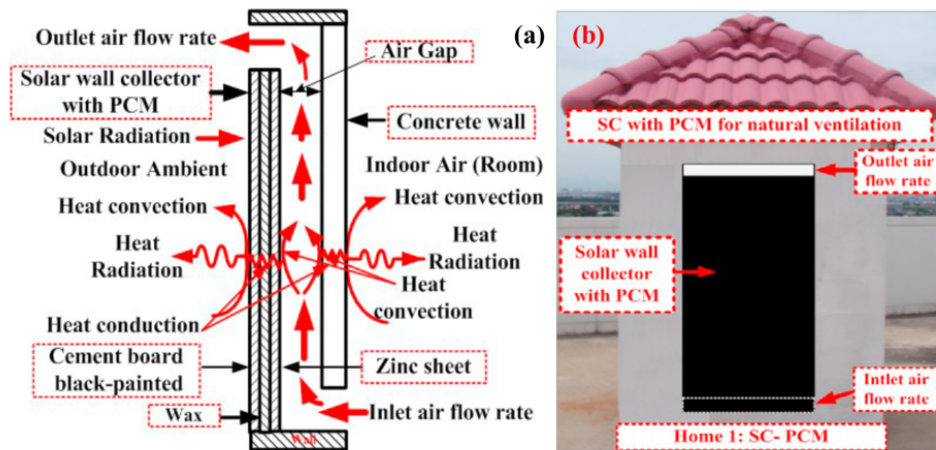


Figure 8. (a) Solar wall collector with PCM and (b) the south facade of experimental house [22].

The outer wall was a triple-layer wall. The first layer was a black-painted cement board to act as a solar radiation absorber. The second layer was PCM (paraffin wax) to act as a heat accumulator. The third layer was a zinc sheet intended primarily for accumulating and transferring heat to indoor air gap. The inner wall was a lightweight concrete that helped protect against heat penetration into the interior of the house. The heat transferred to the gap thanks to the solar radiation, made sure that air temperature in the gap was higher than that of the indoor room such that inducing the buoyant force of the air inside the gap helping the indoor air to move out, reducing indoor air temperature and improving indoor air circulation. The experiments were undertaken on February 5, 2017 without air conditioning in the two experimental houses. Data from temperatures, indoor and outdoor wind speed, amount of heat flow on the south walls of the two houses were collected to value the performance of solar collector-PCM wall. The solar radiation reached its peak of 712 W / m^2 at 12:30, as shown in Figure 9(a). The indoor air temperature of Home 1, in Figure 9(b), appeared to be

lower than the ambient temperature and, than the indoor air temperature of Home 2 about 0.15 to 2°C. Other temperature data showed that the temperature difference between external black-painted surface of solar collector-PCM wall and internal concrete wall of Home 1 covered range of 2.68 °C and 17.79 °C. This revealed that solar collector-PCM system acted as a good thermal insulator in respect to heat that entered in the traditional single concrete wall.

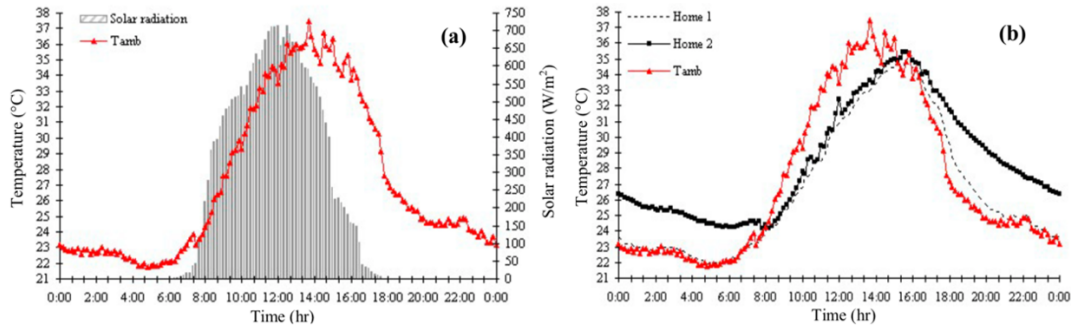


Figure 9. (a) Solar radiation and ambient temperature profile. (b) Comparison between temperature profiles of Home 1 and 2 [22].

The data from velocities revealed that Home 1 had a well circulated indoor air circulation with faster velocity than Home 2 by about 96.62%. The outlet air velocity of solar collector-PCM wall was around 1.2-3.48 m/s. These confirmed that solar collector-PCM system could improve air circulation and could act as an indoor ventilation system. Furthermore, it noted that solar air collector-PCM wall reduced the heat exchange during the day by 59.63% if compared to the traditional single concrete south wall.

1.5.2.3 Finned plate solar air heater with PCM.

The thermal performance of a finned plate solar air heater (FPSAH) integrated with paraffin wax (melting temperature 54 °C, latent heat of fusion 190 kJ / kg, thermal conductivity 0.21 W m⁻¹ K⁻¹) as PCM, was investigated by Kabeel, Khalil, Shalaby and Zayed [23] under weather circumstances of Tanta town, Egypt. The system is shown in Figure 10. A sheet of foam covered by galvanized iron sheet was used as the side's walls and the base of the heater. The top of the heater was covered by thick glass plate to minimize the heat losses. The finned absorber plate shown was manufactured

using a copper sheet and rectangular fins were added along the longitudinal dimension of the absorber (parallel to air flow) with the aim to improve the heat transfer area and the thermal efficiency as consequence.

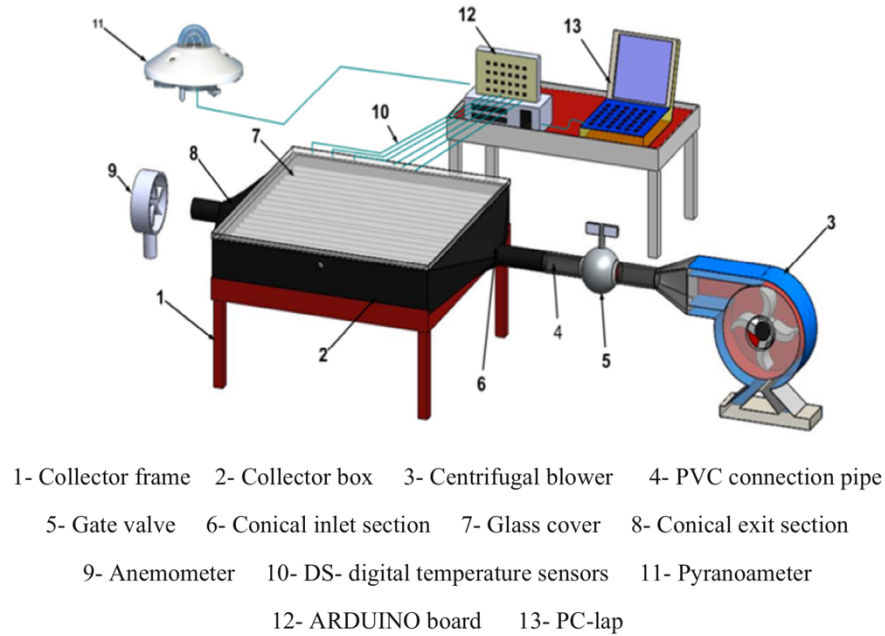


Figure 10. Schematic view of the experimental setup [23].

As shown in Figure 11, air flowed between glass plate and absorber plate and PCM was poured between the finned plate absorber and the base of the heater. Tests were done with PCM or without PCM and with 0.062, 0.028, 0.009 kg/s of air flow rates.

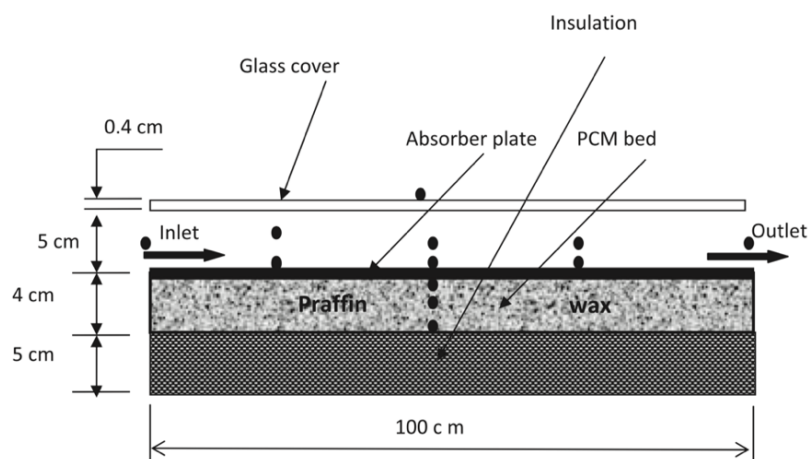


Figure 11. Longitudinal section of solar air collector-PCM system [23].

It was achieved that absorber plate, glass cover, ambient and outlet air temperatures increased concurrently with the solar radiation, reaching the peak at solar noon and gradually decreased until ambient temperature value at sunset. Different trend showed PCM temperature which remained approximatively constant during phase change and continued to increase after solar noon, sign that PCM was storing heat. Significant positive influence of PCM usage was seen 2.5 hours after the sunset in which the air outlet temperature was higher than the ambient temperature by 1.5-6.8 °C. The difference between outlet air temperature and ambient temperature decreased by increasing the air mass flow rates from 0.009 kg/s to 0.062 kg/s with or without PCM usage. Instantaneous efficiency increased with increasing mass flow rate. Without PCM the instantaneous efficiency followed the same trend of the solar radiation curve, reaching its maximum value at sun noon and then it gradually decreased until zero at sunset. The curve trend changed with PCM: at 4:30 pm the instantaneous efficiency started again to increase until a maximum value and then reached zero value after PCM discharging period. The improvement in instantaneous efficiency during no solar hours certainly was at the expense of it during sunshine period. Indeed, the instantaneous efficiency when using PCM was less than that one's without PCM at the period from 8:00 am to 4:30 pm. By integrating the instantaneous efficiency during day time the cumulative efficiency was obtained. The cumulative efficiencies of the FPSAH with using the PCM were 21, 41 and 47,5% when air mass flow rate was 0.009, 0.028 and 0.062 kg/s, respectively. While the corresponding values obtained without using the PCM were 18.6, 37, 41.8%, respectively.

1.5.2.4 Solar air collector integrated with PCM and flat micro-heat pipe arrays.

Wang, Diao, Liang, Zhao, Zhu and Bai conducted a work about an integrated collector storage solar air heater based on latent heat storage and flat micro-heat pipe arrays [24] based in Beijing. This study proposed a new type of integrated collector storage (ICS) that used a highly efficient heat transfer element, namely, flat micro-heat pipe array (FMHPA).

Figure 12 shows the structure of the device, with an overall dimension of 1436 mm × 76 mm × 1765 mm.

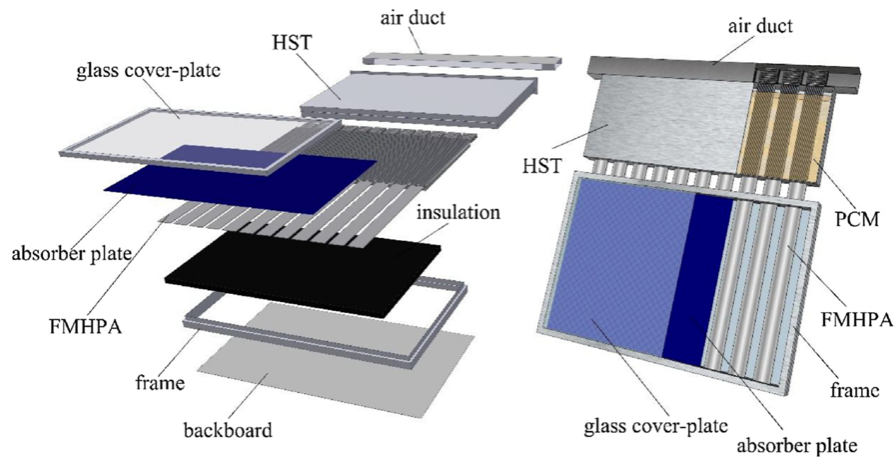


Figure 12. Different parts that compose the system [24].

It was constituted by different layers: 12 FMHPAs (formed through aluminum one-time pressing using multiple micro heat pipes with independent grooves), glass cover plate, absorber plate, collector frame, back board, heat storage tank (HST), air duct, and heat insulation material (HIM). FMHPA was used as a heat transfer component through the phase transition of the working fluid, from evaporation to condensation. As shown in Figure 13, FMHPA was divided into three parts, which were collection, storage, and extraction. The collection section was linked with endothermic black film, the storage section was surrounded by PCM and extraction section was attached with an aluminum-made louver fin to reduce the contact thermal resistance. The sides of the collector frame, collector back board, thermal storage container, and air duct were thermally isolated and a layer of aluminum foil was attached to reflect solar radiation from insulation. The neat area of the heat collector was 0.93 m^2 .

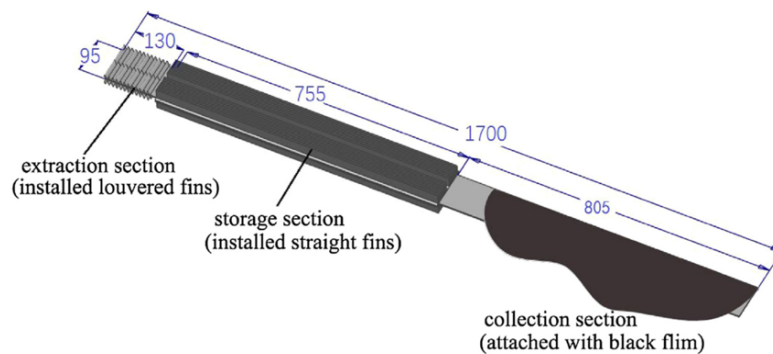


Figure 13. The three section that compose the FMHPA [24].

The PCM used in HST was 52# paraffin wax (melting temperature 52°C, latent heat of phase change 153.4 kJ/kg, specific heat 2.83 kJ/kg K, thermal conductivity 0.11 W/m K) which exhibited a mass of 45.8 kg and air in the duct was used as heat transfer fluid (HTF) to extract the energy from the PCM.

The working principle of the device was divided into charging and discharging modes. During charging mode, in Figure 14(b), the black film was heated by solar radiation, and heat was transferred to FMHPA and it caused the evaporation of the liquid working medium at the bottom of the collector and the gaseous working medium shifted to the storage section. Therefore, PCM was heated from gaseous working medium that in turn condensed and returned to the collection section for repeat the energy conversion. Figure 14(c) shows the operation principle of discharging mode. Before extracting energy stored in the PCM, the working medium in the FMHPA was in equilibrium, that is, the working medium was in liquid state at the bottom of FMHPA and the rest of the space was in gas state. When the HTF flowed through the air duct and energy was exchanged in the form of convective heat transfer between the extraction section and HTF, the equilibrium was broken and the HTF was heated by thermal energy released through reflux condensation of the gaseous medium in the extraction section. When the condensate flowed back to the storage section and came contact with heat transferred from the PCM around the FMHPA, the liquid medium evaporated again and ascended to the extraction section.

Data were recorded from 8:00 to 16:00 as concern the charging mode. During this time air duct was closed. The discharging mode started at 19:00 in which the air duct was opened, and the fan and air inlet duct were connected by corrugated pipe. Previous studies indicated that the use of corrugated surfaces not only increase the heat transfer area but also increase the turbulence of the air flow stream which result in improving the thermal performance of the system [25], [26]. The volume air flow was set at 100, 150 and 200 m³/h. A 3D coordinate system has been defined for HST to observe the spatial temperature profile of the PCM.

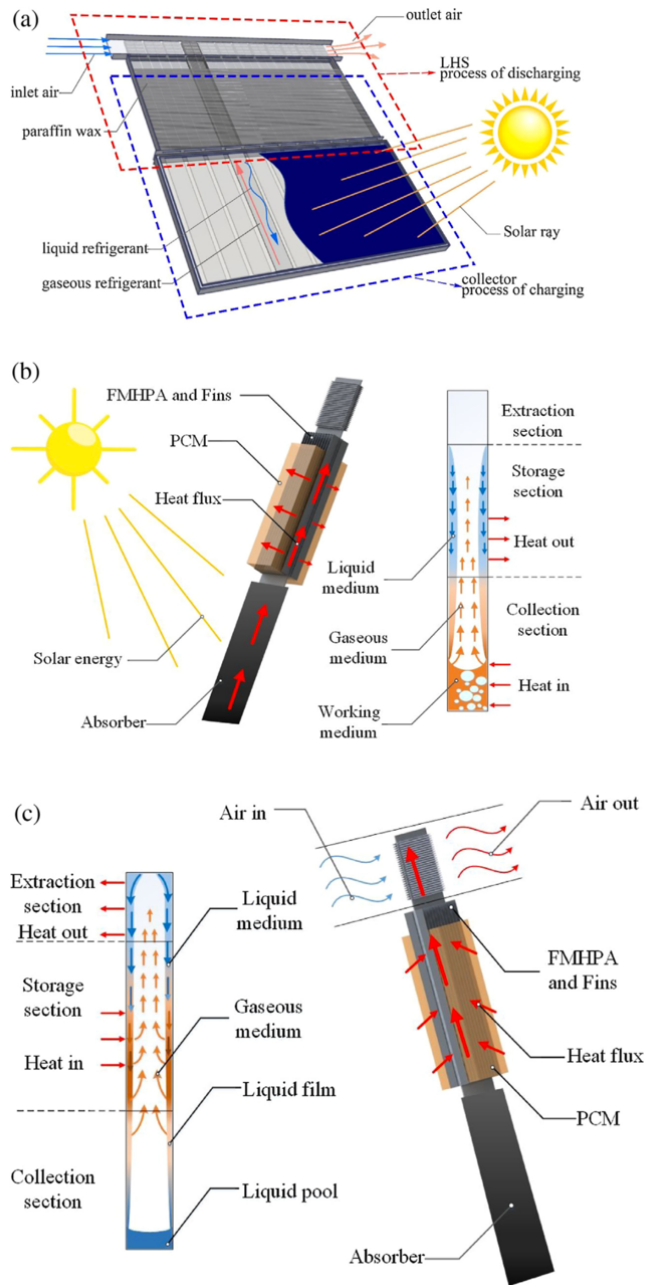


Figure 14. (a) Longitudinal section of the system. (b) Charging process. (c) Discharging process [24].

Charging experiment was conducted from the end of March to early July, when the initial phase of the PCM was solid. It was found also that the average temperature of the absorber was always higher than PCM average temperature and this is due to thermal resistance between them. The maximum value of this temperature differences was $4.2\text{ }^{\circ}\text{C}$ that decreased to zero when the PCM completely melted and this was due

to the low solar radiation intensity that brought the system to thermodynamic equilibrium.

It was demonstrated that as the volume flow rate increased from 100 m³/h to 150 m³/h and to 200 m³/h, the extraction power (amount of energy extracted from HTF in the air duct in unit time during discharging) increased by 10% and 26% and the heat extraction time (time needed to extract all the heat from PCM) decreased by 8% and 20%, respectively.

Chapter 2

EXPERIMENTAL INVESTIGATIONS

2.1 Introduction to the system installed at the University of Ljubljana.

The investigated system, shown in Figure 15, is mainly composed of a solar air collector (SAC), LHTES unit, ductwork and a fan.

The system is installed in one office in the Faculty of Engineering at the University of Ljubljana. The LHTES unit is in the internal space of the room and connected to the SAC exposed in the parapet just behind the window, through the ductwork.

Osterman [27] initially designed the LHTS unit for cooling and Kofalt [28] updated the system adding a SAC to guarantee also a heating usage. The particularity of this system is, therefore, that it could be utilized throughout the year whether it is heating season or cooling season. Subsequently, Kozelj [29] studied the behavior of the system as ventilation system, through experimental investigations and an overall analysis was carried out throughout the heating season with TRNSYS software simulations. The experimental analyzes carried out in this chapter integrate and continue those performed by Kozelj. After explaining the operating modes of the system, the experimental set up is then described and the results of the temperature and velocity measurements are subsequently shown. A further experimental analysis is carried out to study the factual work of the system in feasible office opening hours, from 9 am to 5 pm.

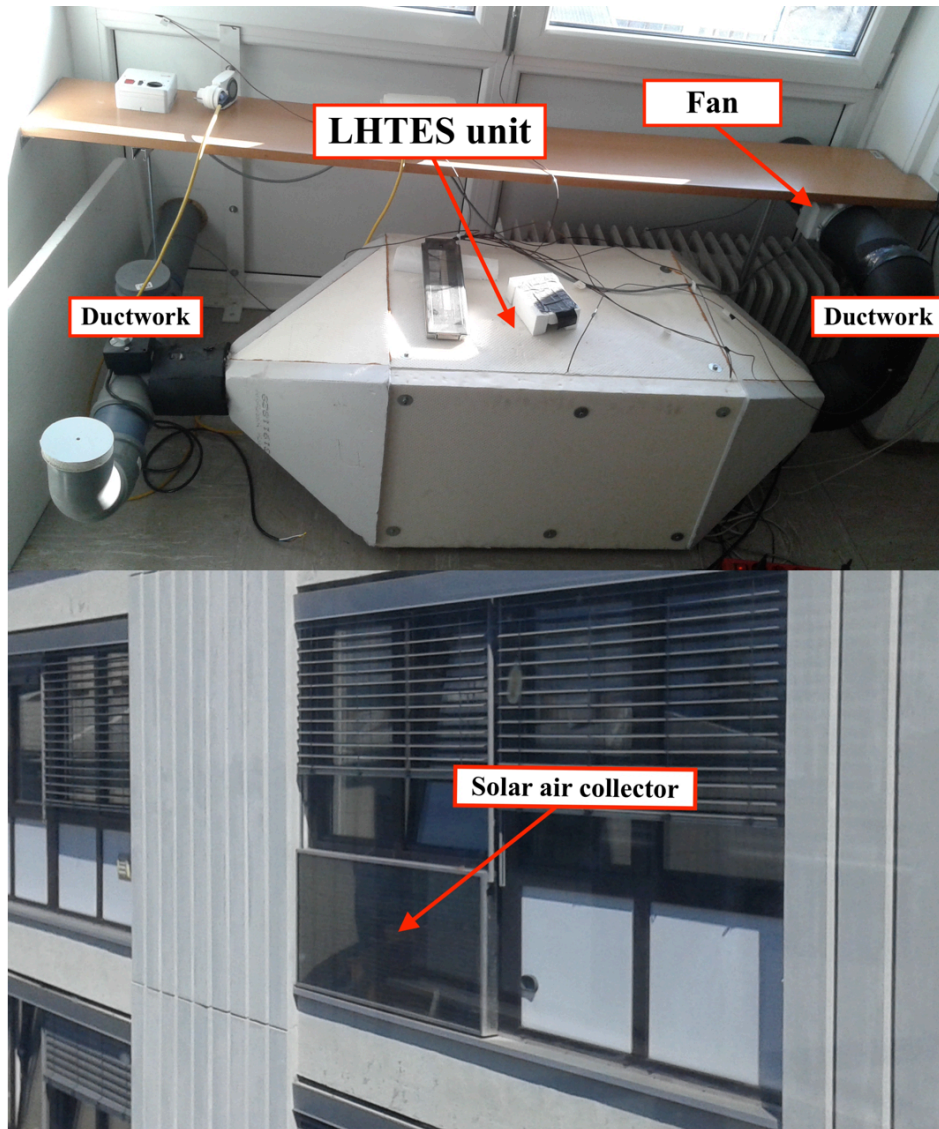


Figure 15. The system installed at the University of Ljubljana.

2.2 Heating and cooling operation mode of the system.

Two different operation modes need to be distinguished; the heating mode in the heating season and the cooling mode in the cooling season. Figure 16 illustrates a scheme that helps to understand these two modalities.

In the heating mode, during the daytime, the air is taken from outside by a fan and goes through the SAC (point 1) that heats the air by solar radiation. The heated air then goes through the LHTES unit and PCM melts and stores thermal energy. When the solar energy is not sufficient or absent, that is, during no solar hours or on cloudy days,

the PCM releases the heat, previously stored, to the air and solidifies. The air is then supplied to the office.

The cooling mode is divided into two cycles, obviously, without SAC utilization. The first cycle is carried out during the night when the cold outside air is supplied to the LHTES unit through the opening in the facade (point 2) to reject heat from the PCM which solidifies to store the cold. The air can then be supplied to the room for night cooling (point 4) or redirected outdoors (point 3). The second cycle is carried out during the day when the warm outside air is drawn (point 2) and goes through the LHTES unit. The PCM starts to melt and the air is cooled before it is supplied to the room (point 4).

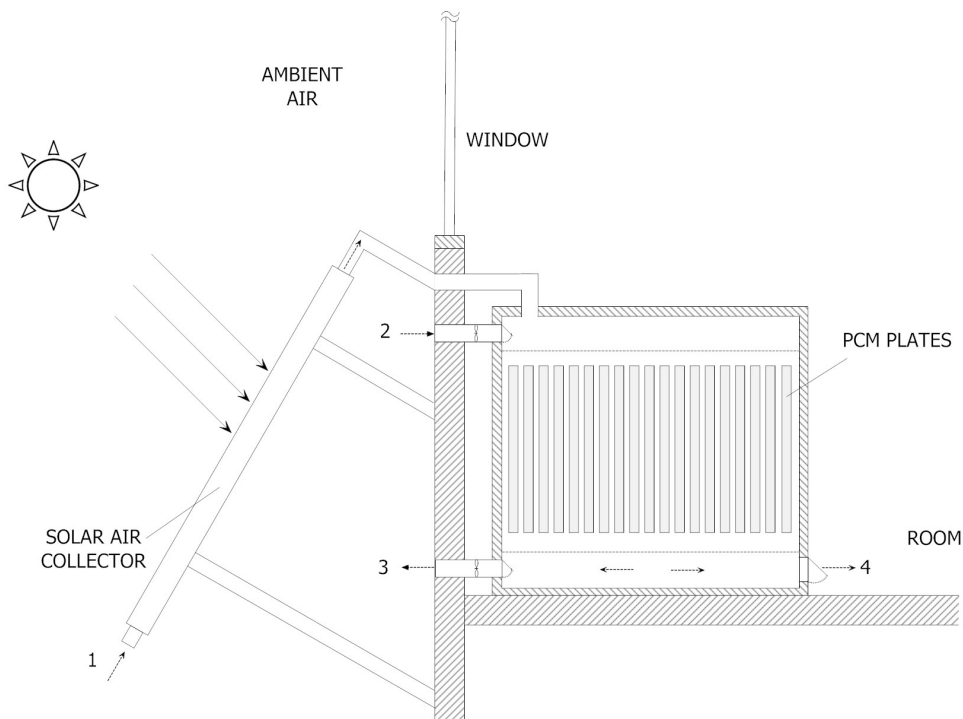


Figure 16. Schematic representation of the system [30].

As previously mentioned, the analysis of the cooling season with the validated numerical model of the system was widely presented by Osterman [27] and the latter topic goes beyond the field of study of this work. Thus, from here on, only the heating mode is taken into account.

2.2.1 Charging and discharging period in the heating mode.

The LHTES unit can store or release heat depending on whether it is in charging or discharging period, respectively. The charging period, summarized in Figure 17(a), takes place when the cold outside air is heated by the sun through the solar collector reaching high temperature values.

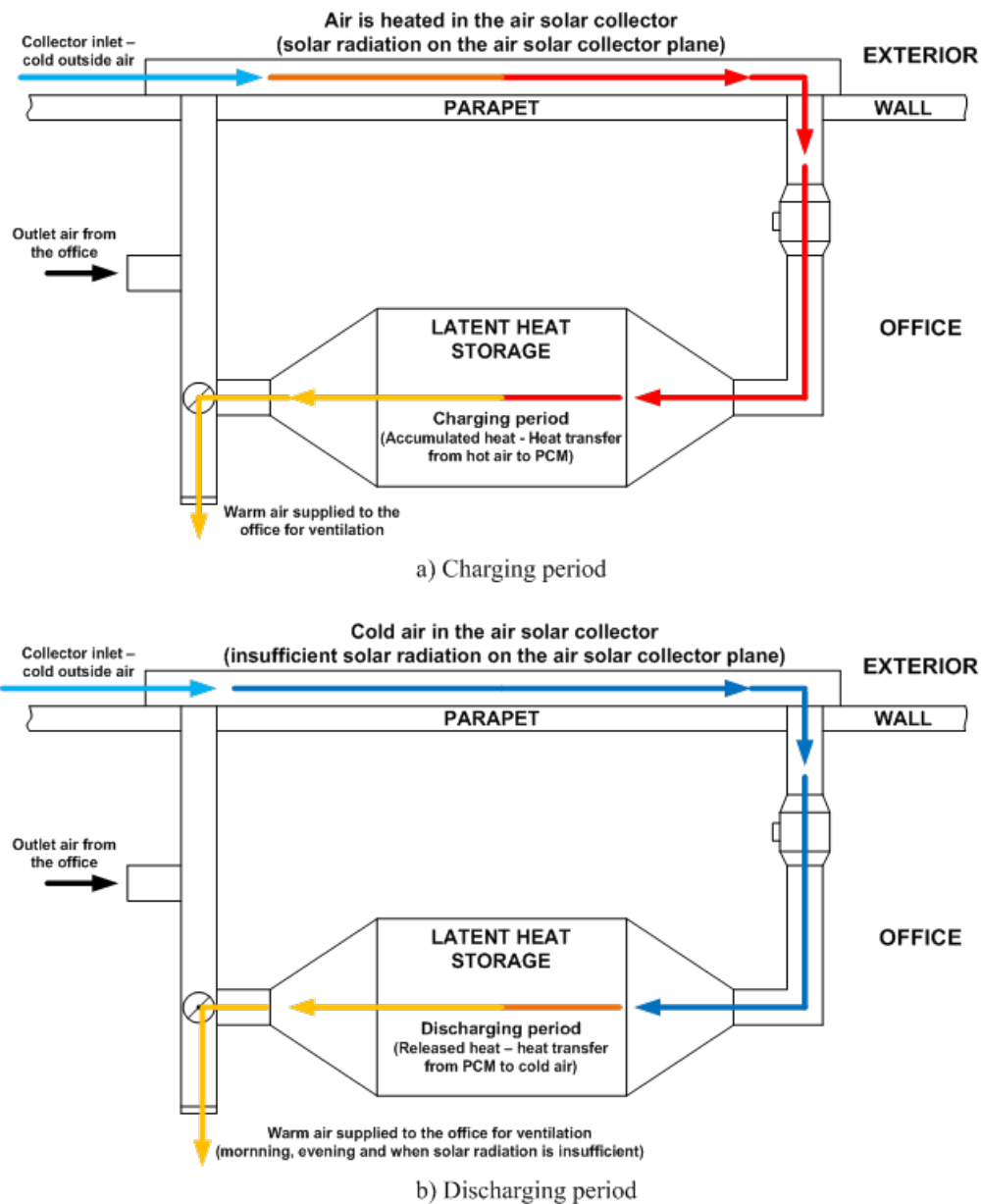


Figure 17. Charging and discharging period in heating mode.

Then hot air goes into the LHTES unit and transfers heat to PCM that melts and stores thermal energy and then air is supplied to the room for ventilation. Charging period happens when heat goes from air to PCM so when air temperature is higher than PCM temperature. In fact, solar radiation heats air more than it needs to reach the 20-23 °C for ventilation and in this way the surplus of heat is given to PCM that will release heat when there is no solar radiation or when the latter is insufficient.

As just mentioned, discharging period, in Figure 17(b), takes place when air temperature is lower than PCM temperature and so, particularly, when there is no sun, when solar radiation isn't high enough, during cloudy days or during the night. The air isn't heated or solar radiation is insufficient and so it remains relatively cold and passing through the LHTES unit it receives thermal energy from PCM which solidifies and releases heat stored in the charging period. Air is then supplied to the room for ventilation.

2.3 Description of the elements of the experimental set-up.

The casing of the LHTES unit is made of 0.8 mm thick polymethylmethacrylate (PMMA) and the external dimensions are 0.725 m × 0.460 m × 0.420 m. The LHTES unit is insulated with 50 mm thick expanded polystyrene (EPS). The LHTES unit contains 29 compact storage modules (CSM) filled with paraffin Rubitherm RT22HC whose characteristics are listed in

Table 2.

Rubitherm RT22HC	Melting temperature range [°C]	Heat storage capacity ¹ [kJ/kg]	Specific heat [kJ/kg K]	Heat conductivity [W/m K]
Typical values	20-23 Main Peak: 22	200 ± 7.5%	2	0.2

¹ Combination of latent and sensible heat in a temperature range of 14 °C to 29 °C

Table 2. Paraffin Rubitherm RT22HC most important properties.

The phase change temperature interval of the PCM was chosen in a way to ensure maximum melting and solidification for both heating and cooling operation modes. Regarding cooling mode, according to Yanbing et al.[18], the melting point of the

PCM should be close to the designed room temperature or according to Medved and Arkar [31] it should be 2 K above average ambient temperature in the Summer months. In charging period in heating operation mode, melting temperature shouldn't be too high because PCM might not be sufficiently charged and on the other hand, PCM melting temperature during discharge period should not be too low trying to keep the air temperature within the comfort level expected for the internal ambient (lower PCM melting temperature values than 20 °C would lead air temperature below the comfort ventilation level more frequently). Therefore, the proposed melting point for the Ljubljana climate was chosen between 22°C and 23 °C.

The dimensions of the CSM plates are 0.45 m × 0.30 m × 0.015 m and they are arranged in two columns: one of 15 plates and one of 14 plates (one plate was removed to perform experimental measurements). The plates are horizontally positioned with the longer side perpendicular to the air flow direction. The distance between the plates of the same column is 10 mm (Figure 18). Two truncated pyramidal shape armor complete the casing of the LHTES unit and work as a thermal insulation.

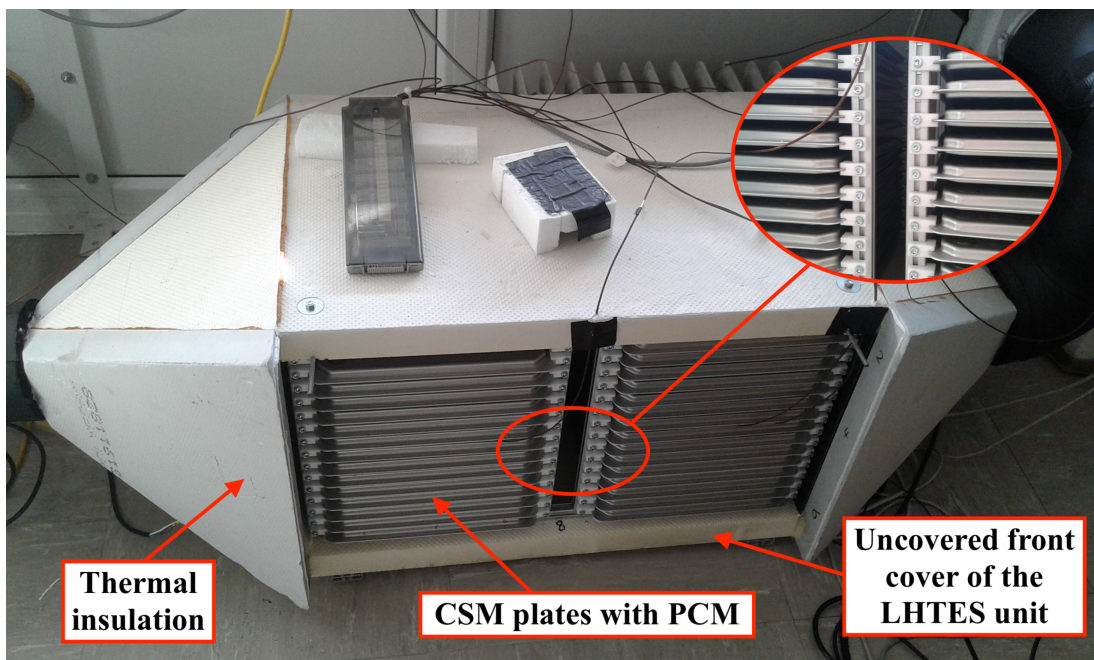


Figure 18. View of the CSM plates inside the LHTES unit casing.

The average mass of the filled CSM plates is 1361 gr, the weight of RT22HC in the CSM plate is 1003 gr and the volume of each plate is 1.42 l. Approximately 9% of the

CSM plate volume is empty to allow the volume expansion passing from solid to liquid phase and to avoid deformation of the CSM plates due to higher pressure.

The number of plates are chosen in respect to the average ventilation heating load per day according to the test reference year for Ljubljana in the heating season that is 4920 kJ/day. Considering the heat storage capacity of 200 kJ/kg reported in the RT22HC data sheet and the PCM weight of 1003 gr in one CSM plate, the LHTES unit would need only 25 plates, but to cover the heat load of ventilation losses on the coldest day, an overall number of 29 CSM plates are used with total heat capacity of 5817 kJ.

The SAC, designed by SolAir Company, has an area of 1638 m² and is installed vertically on the parapet below the office window (Figure 15). Therefore, the tilt angle of the solar air collector is 90°. Figure 19 illustrates a SAC schematic section that helps to understand its structure.

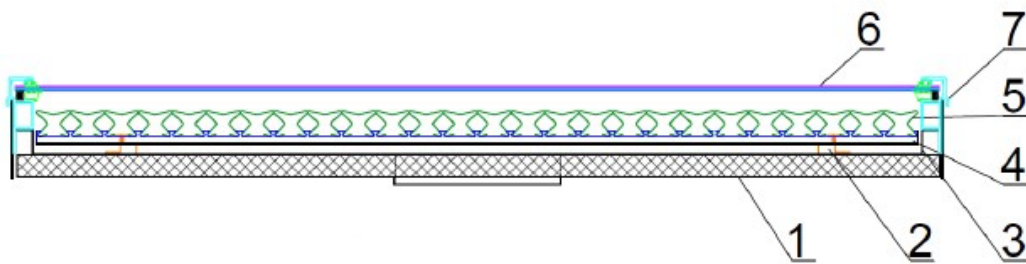


Figure 19. Structure of the solar air collector [30].

Different layers are distinguished:

- 1- thermal insulation made of polyethylene and it is located on the back of the solar air collector (there is no side insulation);
- 2- spacer made of a heat-resistant plastic;
- 3- back assembly of galvanized steel sheet;
- 4- absorber holder-stainless sheet;
- 5- absorber plate made of aluminum with 0.2 mm fin thickness and 30 mm fin width. Solar absorptance of the absorber is 93% with the tolerance of $\pm 2\%$. Its hemispherical emittance is 35% with the tolerance of $\pm 3\%$. The absorber is painted with a black thickness insensitive spectrally selective (TISS) paint;

- 6- polycarbonate sheets Macrolux® of 4 mm thick constitute the glazing of the solar air collector with solar transmittance of $90\% \pm 1\%$.

SAC performance measurements were made at Fraunhofer Institute for Solar Energy Systems ISE in Freiburg, Germany [32]. Power output of a SAC was obtained through measurements under the steady-state conditions with the calorimetry method. An efficiency value of 0.703 was obtained with radiation normal incidence angle, solar irradiation on the solar air collector surface of 961 W/m^2 , thermal power output of 1290 W and air mass flow rate of 250 kg/h. Figure 20 shows SAC power output over temperature differences between the mean air temperature in the SAC (ϑ_m) and the ambient air temperature (ϑ_a) at 1000 W/m^2 of solar irradiation [32].

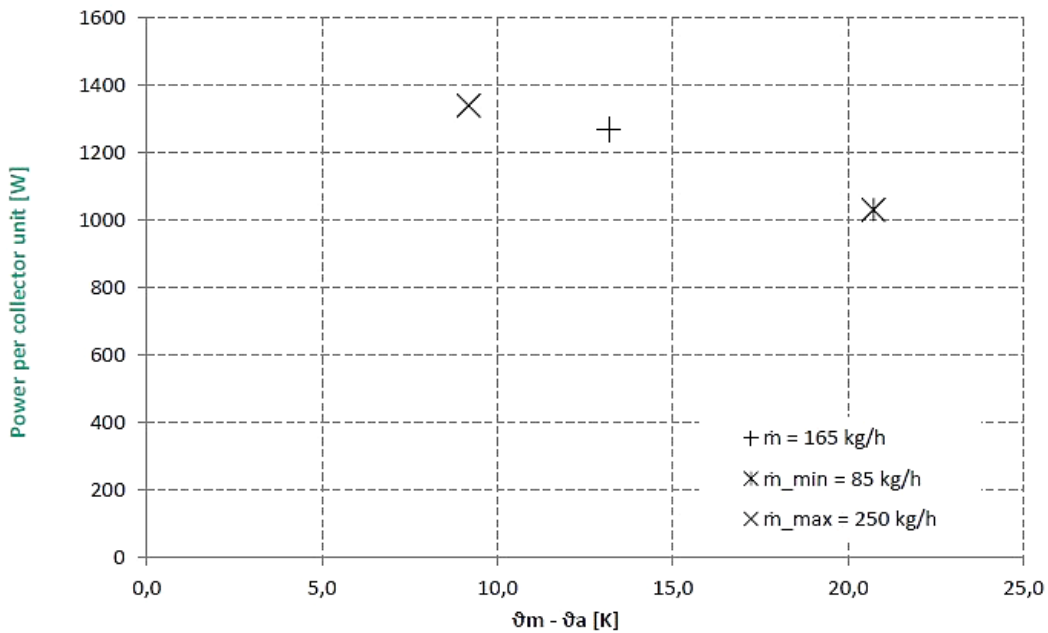


Figure 20. Power output per solar air collector unit [32].

The ductwork consists of 100 mm diameter ducts. The ductwork that connects solar air collector to LHTES unit and the ductwork that exits from the LHTES unit is coated with 20 mm thick Armaflex insulation. Figure 21 shows the main elements that composed the layout of the experimental measurements. A fan with input power within 21 W and 33 W pushes the air through the entire system. The fan is connected to a

Wall-air controller that allows to set up to 5 different fan rotation speeds. A switching hatch in the T-curve that follows the LHTES unit can direct the air flow to the office room or to the outlet duct of the system which leads outside. A motor can rotate the switching hatch of 90° changing the air flow direction inward or outward. The control system is powered with 230 V. The function of the extraction duct positioned along the outlet duct is to draw automatically, through natural ventilation, heavy air that needs to be changed (in the center of this duct the velocity measurements described in Paragraph 2.5.1 were performed).

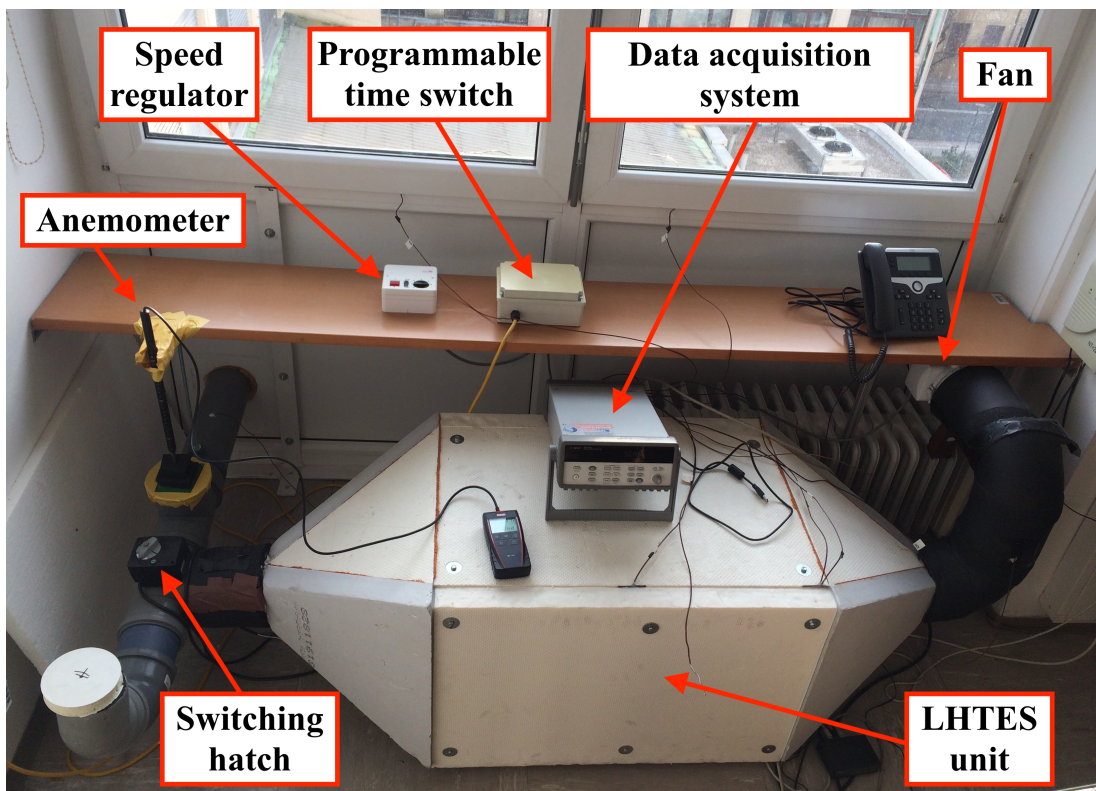


Figure 21. Main elements of the experimental set-up.

Lastly, Figure 22 shows the schematic layout of the system and gives information about how the experimental measurements were performed. It provides the air flow direction in each kind of measurements, the position of the thermocouples in temperature measurements and in which points of the system the velocity measurements were carried out.

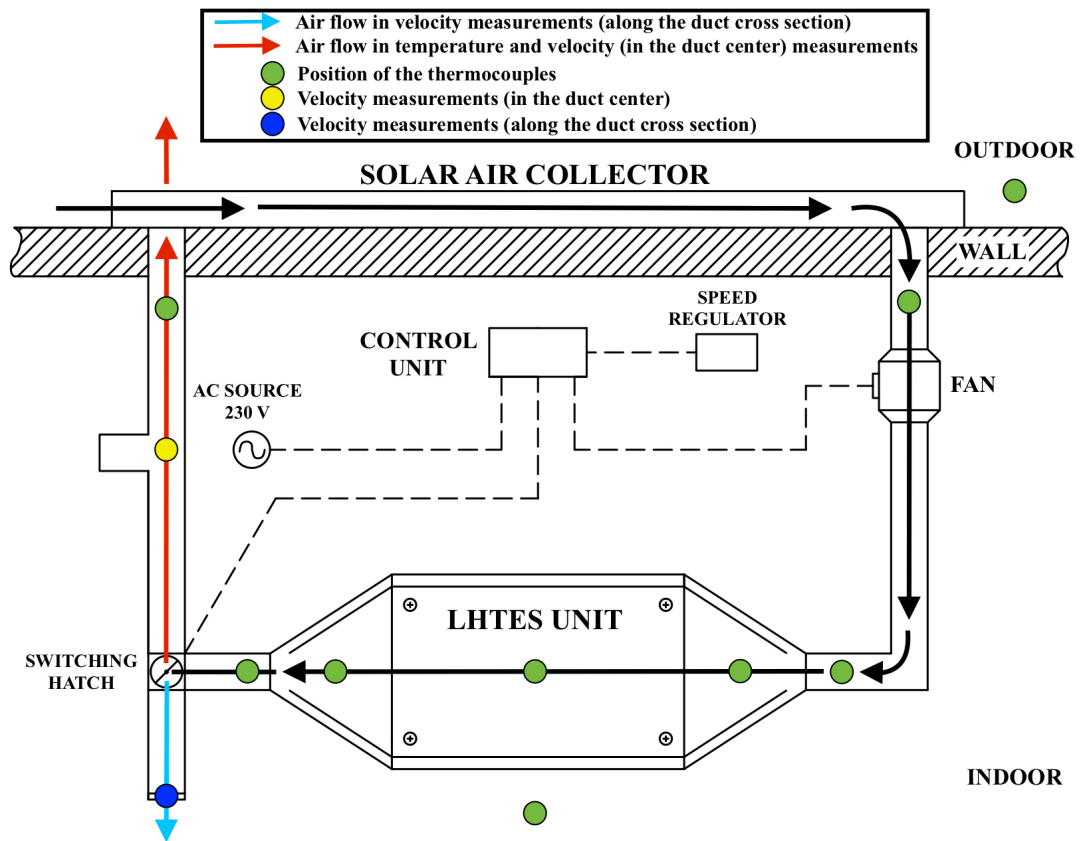


Figure 22. Scheme of the experimental set-up.

2.4 Temperature measurements.

Temperature experimental measurements were performed with constant air mass flow rate through the system, guaranteed with constant value of fan rotation speed imposed to the maximum value (level 5 on the Wall-air controller). As a result, maximum heat stored and released in the LHTES unit were achieved. The switching hatch was fixed in such a way to direct the air to the outlet duct which lead outside. It is important to underline that this system doesn't work for factual ventilation of the room, whether it is for heating or cooling season, but it was designed to perform studies and measurements for future applications and so it was not necessary to let the air enter the office room. In fact, the air exiting the LHTES unit would have been sometimes much higher than 20 °C on sunny days and sometimes much lower than 20°C on cold, cloudy or rainy days and this would have brought to high thermal discomfort in the room.

Temperature measurements were performed with Thermopar type T thermocouples that have a measuring range from $-270\text{ }^{\circ}\text{C}$ to $+400\text{ }^{\circ}\text{C}$ and an accuracy of $\pm 0.119\text{ }^{\circ}\text{C}$. Nine thermocouples were placed at various locations, as shown in Figure 22, those in the storage unit were positioned in the centerline, between two CSM plates (detail in Figure 18). Thermocouples were connected to the data acquisition system Agilent 34970A (Figure 21). RS-232a interface cable was used to connect data acquisition system to a computer in which BenchLink Data Logger 3 was installed so that data could be collected and displayed directly on it.

To clarify, only some of these nine temperatures, considered the most representative, are reported in the following figures:

- office room air temperature – it should be between 20 and $23\text{ }^{\circ}\text{C}$ and it is necessary to calculate ventilation losses from the room and heat losses of the system;
- solar collector inlet air temperature – it corresponds to the outdoor air temperature but its factual value is surely higher. This is due to the outlet duct that does not lead the air directly outside but it ends on the back face of the SAC installed on the outdoor opposite surface of the room wall (Figure 23 and Figure 22). A probable mixing of the air exiting the system and the fresh air that is taken from outside occurs, which leads to higher real solar air collector inlet temperatures. The real phenomenon that occurs is not known but no significant differences are evident in calculations. From here on, if it is not specified, the outdoor temperature is equal to the solar collector inlet air temperature;
- LHTES unit inlet air temperature – this can be considered equal to the solar air collector outlet temperature except for thermal losses in the duct that leads air from the solar air collector to the LHTES unit;
- LHTES unit outlet air temperature – air temperature that has just left the LHTES unit to value the effective work of the storage.

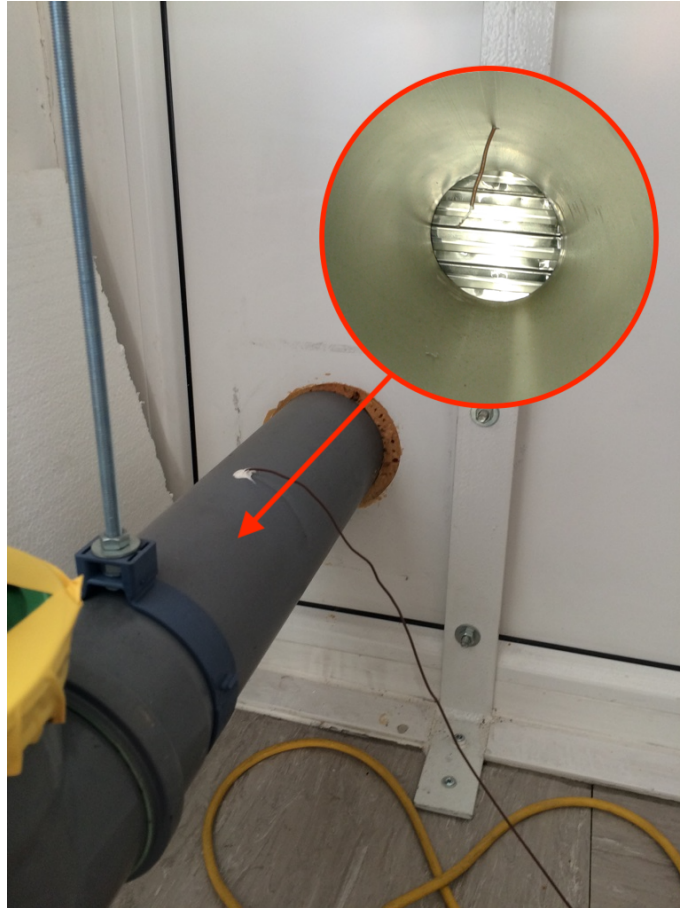


Figure 23. Particular of the outlet duct with the sectional view.

2.4.1 Temperature measurements from 30/11/2017 to 5/12/2017.

Instantaneous temperature values were taken every 2 minutes from all the nine thermocouples and the data was later analyzed in excel. Figure 24 gives information about the temperature profiles taken in 6 days from November 30, 2017 to December 5, 2017.

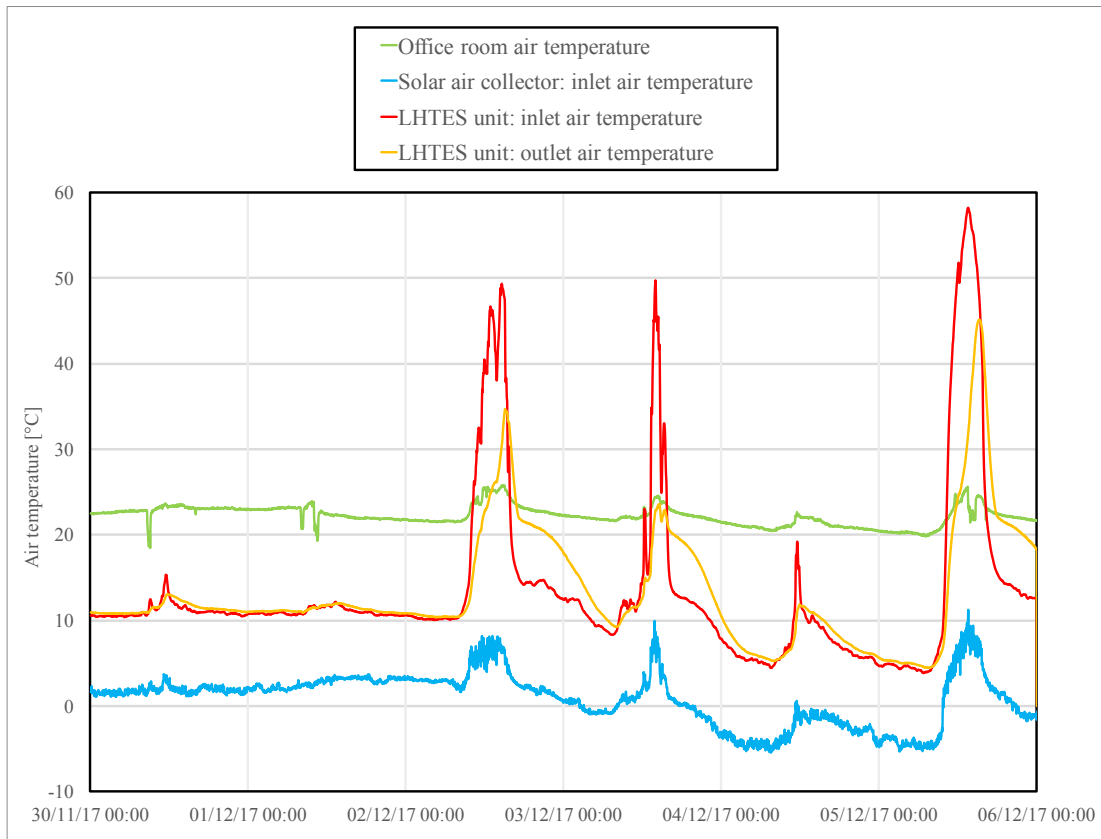


Figure 24. Temperature profiles from November 30 to December 5.

Office room air temperature downward peaks are due to the opening of the window in the office room. The outdoor air temperature depends tightly on solar radiation because of the thermocouple position close to the building facade that is heated by solar radiation which, in turn, heats the surrounding air. This phenomenon favors higher inlet air temperatures in the SAC. It can be immediately observed that the first two days were cloudy-rainy days and solar radiation that heated the air was practically irrelevant. Instead, December 2, December 3 and December 5 were sunny days with maximum values of outlet solar collector air temperature of 49 °C, 50 °C and 58 °C, respectively (Table 3).

		Nov. 30	Dec. 1	Dec. 2	Dec. 3	Dec. 4	Dec. 5
Solar air collector: inlet air temperature [°C]	Min.	1	2	0	-4	-5	-5
	Max	4	4	8	10	1	11
	Average	2	3	3	1	-3	0
LHTES unit: inlet air temperature [°C]	Min.	10	11	10	8	4	4
	Max	15	12	49	50	19	58
	Average	11	11	19	14	7	19
LHTES unit: outlet air temperature [°C]	Min.	11	11	10	9	5	4
	Max	13	12	35	24	12	45
	Average	11	11	18	15	8	17

Table 3. Main temperature values obtained from November 30 to December 5.

When air temperature that enters the storage is higher than the outlet air temperature it means that the LHTES unit is storing thermal energy, otherwise LHTES unit is releasing heat to the air. On November 30, December 1 and December 4 no particular solar activity was recorded and for this reason these days are not important for the evaluation of the system. On December 2, December 3 and December 5 the LHTES unit stored energy approximately from 9 am and 3:30 pm, about 6 hours and half, and released heat in the following hours. To see the effect of the storage usage, a comparison is made in the air temperatures that would have been achieved, whether air is supplied to the room with the storage or without the storage. The latter means that air would be introduced directly in the room as it exits the SAC. Thus, outlet air temperature from SAC and outlet air from LHTES unit are taken into account with or without storage, respectively. Table 4 shows the time, in hours, in which the outlet air temperature was higher than 20 °C and than 15 °C and the time rate, in percentage, in which this happened on each day. Temperature of air with the storage reached at least the comfort level of 20 °C, 4.5 hours, 0.4 hours and 4.4 hours more in respect to the correspondent values of the system without the storage on December 2, December 3 and December 5, respectively. The differences are even more pronounced on these three days considering the outlet air equal or higher than 15 °C with 6,4 hours, 7 hours, 5.1 hours more of coverage. The system with the storage reached the outlet air

temperature higher or equal to 20 °C the 45% of the time on December 5, and the outlet air temperature higher or equal to 15 °C the 58% of the time on December 2.

		Nov. 30	Dec. 1	Dec. 2	Dec. 3	Dec. 4	Dec. 5
Time in which air supplied ≥ 20 °C [h]	No storage	0	0	6.1	2.9	0	6.5
	Storage	0	0	10.6	3.3	0	10.9
Time in which air supplied ≥ 15 °C [h]	No storage	0.2	0	7.5	4.1	0.6	8.3
	Storage	0	0	13.9	11.1	0	13.4
Time rate in which air supplied ≥ 20 °C [%]	No storage	0	0	25	12	0	27
	Storage	0	0	44	14	0	45
Time rate in which air supplied ≥ 15 °C [%]	No storage	1	0	31	17	3	35
	Storage	0	0	58	46	0	56

Table 4. Comparison between the system with or without the storage from November 30 to December 5.

2.5 Velocity measurements.

Air mass flow rate knowledge is necessary in energy calculations and for this reason velocity measurements were performed along the system. KIMO[®] VT 110 hot wire thermo-anemometer was used in velocity measurements and its main specifications reported in its technical data sheet are summarized in Table 5.

KIMO [®] VT 110	Measuring range	Accuracy		Resolution
Velocity [m/s]	From 0.15 to 30 m/s	From 0.15 to 3 m/s	$\pm 3\%$ of reading ± 0.05 m/s	0.01 m/s
		From 3.1 to 30 m/s	$\pm 3\%$ of reading ± 0.2 m/s	0.1 m/s
Temperature [°C]	From 0 to 50 °C	$\pm 0.3\%$ of reading ± 0.25 °C		0.1 °C

Table 5. KIMO VT 110 specifications.

2.5.1 Velocity measurements in the duct center.

At first, the anemometer was positioned in the extraction vent in the outlet duct, as shown in Figure 25, taking care that the hotwire probe was fixed in the outlet duct

center. As previously done for temperature measurements, air mass flow rate was kept constant by constant fan rotation speed. Velocity profiles were obtained taking the average value every 5 minutes displayed on the anemometer. This was done trying to avoid an incorrect velocity reading due to turbulence phenomena.



Figure 25. Placement of the anemometer probe in the duct center.

The first velocity measurements were performed on December 19, 2017 from 4:30 pm to 7 pm and the velocity trend obtained is shown in Figure 26. No significant perturbations were recorded, the maximum, the minimum and the average values were 0.74 m/s, 0.70 m/s and 0.72 m/s, respectively. No high air temperature difference from the start and the end of these first measurements was registered and for this reason it wasn't possible to see if there was a dependence between air velocity and air temperature.

The standard deviation gives a value of the data dispersion obtained in the measurements and it was calculated through the following equation:

$$s(v) = \sqrt{\frac{\sum_{i=1}^N (v_i - \bar{v})^2}{N - 1}} \quad (2.1)$$

Where:

- $s(v)$ is the standard deviation of the velocity data,
- v_i is the i -th velocity reading value in the measurements,
- \bar{v} is the average velocity value of all the data recorded,
- N is the number of readings (data) recorded.

Another useful statistic parameter is the standard error of the average, that is a measure of the precision of the estimated average in the measurements. The standard error of the average ($S_{\bar{v}}$) depends on both the standard deviation and the number of data recorded by the simple relation:

$$S_{\bar{v}} = \frac{s(v)}{N} \quad (2.2)$$

Standard deviation and standard error of the average values were ± 0.009 m/s and ± 0.002 m/s, respectively. Velocity accuracy, in meter per second, to the first decimal place is already sufficiently accurate in this kind of problem and so no particular influence by the dispersion of the data and the estimate of the average was recorded.

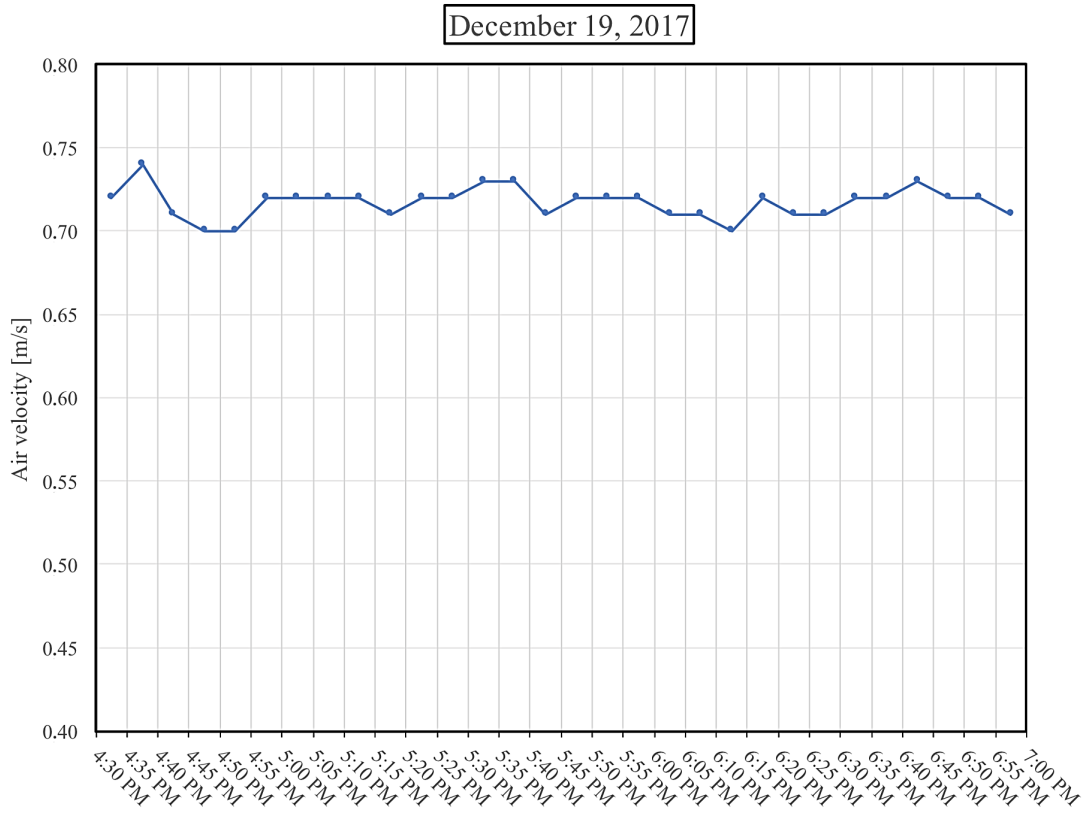


Figure 26. Velocity measurements in December 19.

Other measurements were performed on two sunny days, January 3 and January 4, 2018, within the same time range for 4 hours, from 1:30 pm to 5:30 pm to see the repeatability of the measurements. It is important to note that the hot wire probe was removed after the first velocity measurements performed on December 19 and so probable errors due to imperfect repeatability of the positioning, which was manual, may have worsened the precision of the measurements. Profiles of velocity taken on January 3 and in January 4 are shown in Figure 27. A small increase of the velocity values can be seen for both profiles up to approximately 3 pm when solar radiation was more intense. This may be due to buoyance forces that are stronger when air density is lower and so when air temperature rises.

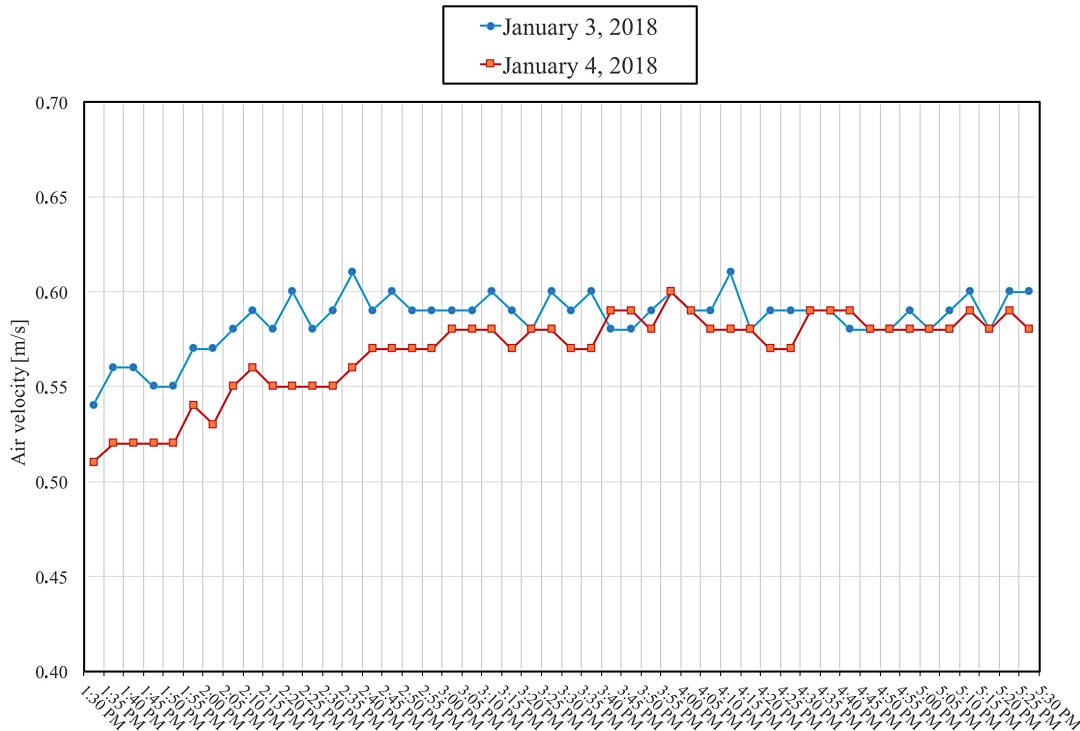


Figure 27. Velocity measurements in January 3 and in January 4.

The results of the three days of velocity measurements are reported in Table 6. The non-perfect repeatability of the hot wire probe positioning can be noted from the more pronounced different values between the 1st velocity measurements and the other two measurements. The average velocity of 0.72 m/s in the 1st was 22% higher than the 2nd and 26% higher than the 3rd. The higher standard deviation and standard errors were found in the 3rd velocity measurements but the errors were however negligible, as already mentioned, compared to the significant numbers that would need the average velocity value searched for mass flow rate calculation.

VELOCITY MEASUREMENTS	1st	2nd	3rd
Date	19/12/2017	03/01/2018	04/01/2018
Max. velocity [m/s]	0.74	0.61	0.60
Min. velocity [m/s]	0.70	0.54	0.51
Average velocity [m/s]	0.72	0.59	0.57
Standard deviation [m/s]	±0.009	±0.015	±0.023
Standard error [m/s]	±0.002	±0.002	±0.003

Table 6. Comparison between the velocity measurements.

2.5.2 Velocity measurements along the duct cross section.

The difference between the 1st and the 2nd and 3rd velocity measurements and the difference from velocity values obtained by Kozelj [29] (almost double) with the same measurement modality of Paragraph 2.5.1, suggested searching velocity values changing the position of the hot wire probe along the duct section. For this reason, only for this kind of measurement, the air flow was directed into the room (Figure 22) so as to have the possibility to read velocity values with the anemometer along the cross section of the duct that admits air into the office.

More appropriate equipment for velocity measurements would have needed a Pitot tube usage. Indeed, ducted air flow measurements are generally carried out following standard methodologies as *Pitot traverse measurement technique* through *Equal Area method*, *Log-Linear method* or *Log-Tchebycheff method*. Taking note from these methods, the decision was made to read velocity along 4 traverses and in each of these there were 4 velocity reading points, as shown in Figure 28.

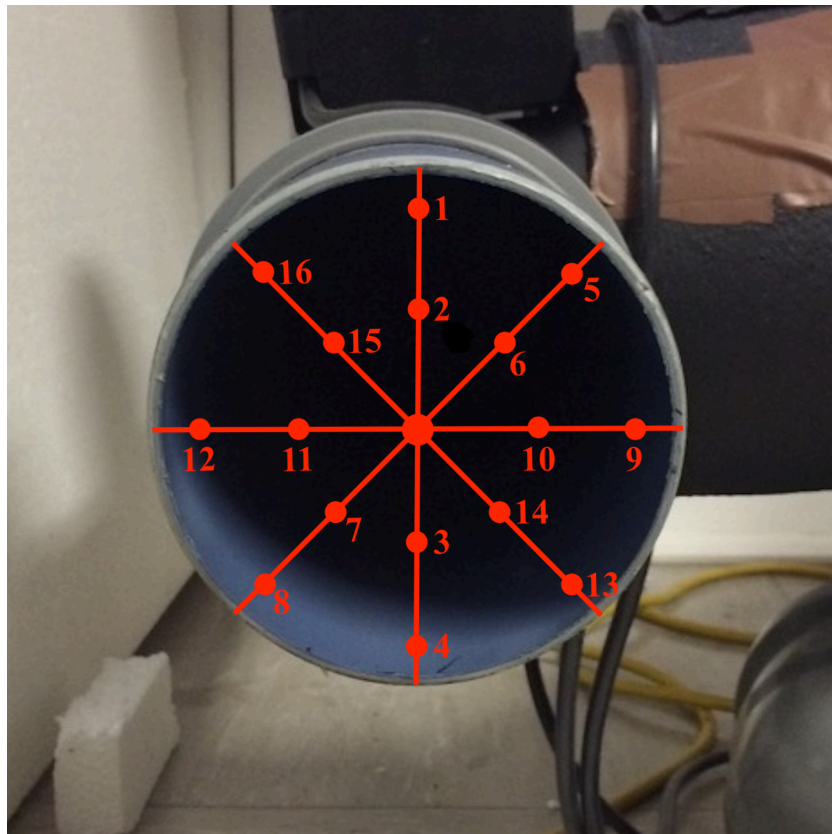


Figure 28. Reading points in the cross section along the four traverses.

No specific distance between one reading point and another was respected because of the difficulty that this kind of measurement would have acquired, but an attempt was made to keep the geometry of the configuration shown in Figure 28. Including the center point, a total of 17 reading points in the duct cross section were established and each reading was performed taking 3-minute average velocity (instead of 5 minutes of the previous velocity measurements) displayed on the anemometer. All the 17 velocity readings needed about one hour to be performed. These were repeated for 6 hours, from 11 am until 5 pm on January 24, 2018. Table 7 gives the values obtained.

	Velocity [m/s]						Average velocity in the point
	11 am 00 pm	12 pm 1 pm	1 pm 2 pm	2 pm 3 pm	3 pm 4 pm	4 pm 5 pm	
Point 1	1.5	1.0	0.7	0.5	0.3	0.5	0.8
Point 2	0.7	0.5	0.6	0.5	0.4	0.5	0.5
Point 3	1.8	1.8	1.8	1.5	1.6	1.8	1.7
Point 4	2.5	2.5	2.5	2.6	2.3	2.7	2.5
Point 5	0.8	0.7	0.6	0.4	0.3	0.6	0.5
Point 6	0.4	0.4	0.3	0.3	0.2	0.4	0.3
Point 7	2.4	2.5	2.5	2.2	2.4	2.4	2.4
Point 8	2.6	2.6	2.7	2.5	2.8	2.9	2.7
Point 9	0.7	0.6	0.6	0.5	0.5	0.6	0.6
Point 10	0.4	0.4	0.3	0.3	0.3	0.4	0.4
Point 11	2.3	2.2	2.1	1.8	2.4	2.5	2.2
Point 12	2.2	1.8	1.7	1.4	1.7	2.1	1.8
Point 13	1.8	1.9	1.9	1.6	1.5	1.9	1.8
Point 14	0.9	1.4	1.0	0.8	0.6	0.6	0.9
Point 15	1.4	1.4	1.3	1.4	1.3	1.6	1.4
Point 16	1.6	1.0	0.8	0.6	0.8	1.3	1.0
Center point	0.8	1.0	0.7	0.7	0.6	0.7	0.8

Table 7. Data from velocity measurements along the cross section.

The center point shown an average velocity of 0.8 m/s, very close to that of the previous 1st velocity measurements of 0.72 m/s and therefore acceptable with what had already been done. This time, values from different positions in the cross section

showed a high dispersion: from 0.2 m/s of point 6 to 2.9 m/s of point 8. Figure 29 gives information about the hourly average air velocities in the cross section (obtained from the previous Table 7 making the average of each column) and the hourly average air temperature read from the thermo-anemometer during measurements. In contrast to what explained in Paragraph 2.5.1, here velocity decreases as the temperature increases. As hourly average air temperature reached its maximum value of 48 °C, in reverse, hourly average air velocity reached the minimum value of 1.1 m/s from 2 pm to 3 pm. The values are reported in Table 8.

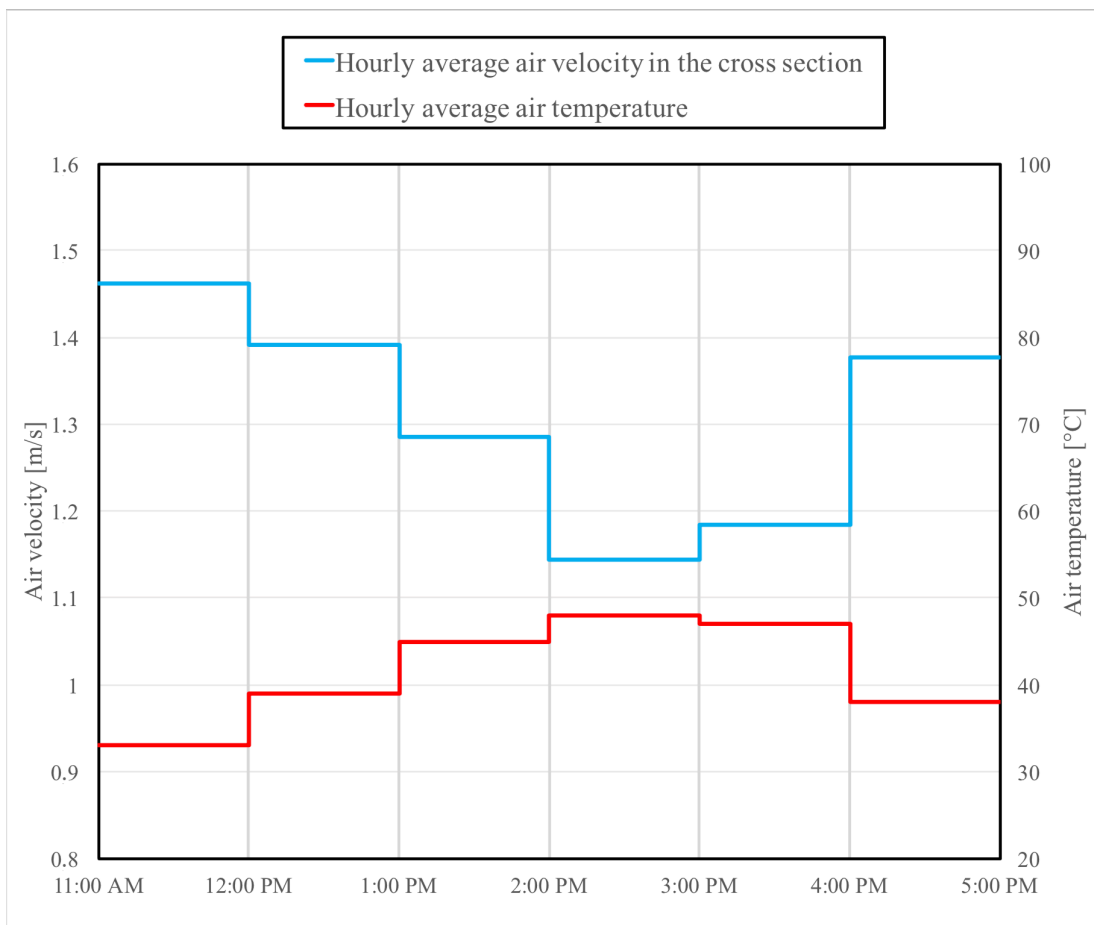


Figure 29. Hourly average air velocity and hourly average air temperature profiles in the cross section.

	11am 12 pm	12 pm 1 pm	1 pm 2 pm	2 pm 3 pm	3 pm 4 pm	4 pm 5 pm
Hourly average air velocity [m/s]	1.5	1.4	1.3	1.1	1.2	1.4
Hourly average air temperature [°C]	33	39	45	48	47	38

Table 8. Data from Figure 29.

A physical interpretation may be that the air temperature growth would have caused the rise of buoyance forces that would have pushed the air upward against LHTES unit casing and CSM plates, bringing to kinetic energy losses in frictions and in turbulences. This dissipation should be more evident in the peripheral points of the cross section and for this reason it wasn't possible to record it in the duct center measurements of Paragraph 2.5.1 in which buoyance forces, on the contrary, lead to a light velocity rise, as normally expected from this phenomenon. It is also highlighted that these last velocity measurements would need a more suitable instrumentation to be more accurate and reliable.

Air volumetric flow rate was found through the following equation.

$$\dot{V} = A \cdot v \quad (2.3)$$

Where:

- A is the cross section area of the duct with 0.1 m diameter;
- v is the air velocity.

Making the average of the hourly average air velocity values, a velocity of 1.3 m/s was obtained to which 36.97 m³/h (10.27 l/s) air volumetric flow rate corresponds. The velocity standard error was ± 0.051 m/s and this meant an error of ± 1.44 m³/h (0.4 l/s) in the evaluation of average air volumetric flow rate. It is also important to emphasize that 10 l/s is the standardized inlet air flow rate to achieve the maximum level of thermal comfort for ventilation.

Air mass flow rate was obtained through:

$$\dot{m} = \rho \cdot \dot{V} = \rho \cdot A \cdot v \quad (2.4)$$

where ρ is air density calculated from air temperature in operating conditions. Thus, from the air volumetric flow rate of 36.97 m³/h a value of air mass flow rate of 0.012 kg/s was obtained. This value of air mass flow rate was considered constant in the following analysis and in TRNSYS simulations.

2.6 System analysis during ventilation time.

Further measurements were performed to investigate the operation of the system for office room ventilation. For this reason, the system was supposed to run in one hypothetical ventilation time from 9am to 5 pm. Thus, air flow was no longer constant throughout the day like previous temperature measurements, but the fan was switched on from 9 am to 5 pm and was switched off in the other hours. Temperature measurements were taken constantly from January 22 to January 26, 2018. Temperature profiles in ventilation time are reported in Figure 30.

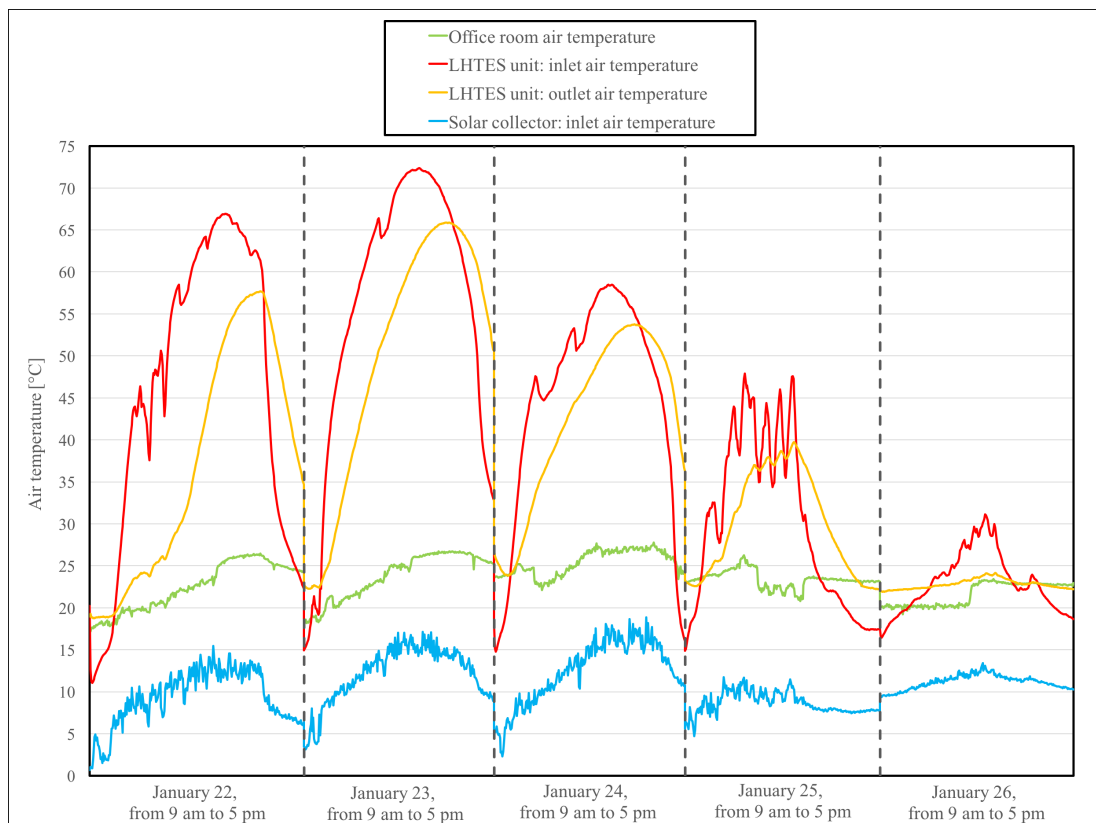


Figure 30. Temperature profiles during ventilation time taken from January 22 to January 26.

Accidentally, these measurements allowed to compare the functioning of the system during different types of weather. The first two days of measurements were sunny days, January 24 was a bit cloudy, and January 25 and January 26 were respectively partly cloudy and cloudy days, as it is noticeable from temperatures of Figure 30.

Therefore, peaks of inlet air temperature in LHTES unit decreased from a maximum of 72°C on January 23 to 31 °C on January 26. Maximum, minimum and average temperatures on each day are reported in Table 9. On the first three days, LHTES unit started to store heat from about 9:30 am to 3:30 pm and released heat in the following operating hours. The sequence of consecutive peaks in the profile of the LHTES unit inlet air temperature on January 25, are due to a decrease of solar radiation when the sun was covered by clouds. For this reason, the heat stored was less than previously and the LHTES unit started to release heat at around 1:45 pm, almost 2 hours before the previous sunny days. On January 26 the heat was stored from about 11:15 am, this delay was caused by the difficulty of air reaching temperatures higher than those of PCM because of insufficient solar radiation.

Ventilation time		January 22	January 23	January 24	January 25	January 26
Office room temperature [°C]	Max	26	27	28	26	23
	Min	17	18	22	21	19
	Average	23	24	25	23	22
Solar collector: inlet air temperature [°C]	Max	15	17	19	12	13
	Min	1	3	2	5	9
	Average	9	12	12	9	11
LHTES unit: inlet air temperature [°C]	Max	67	72	58	48	31
	Min	11	15	15	15	16
	Average	45	56	45	30	23
LHTES unit: outlet air temperature [°C]	Max	58	66	54	40	24
	Min	19	22	24	22	22
	Average	37	50	42	30	23

Table 9. Main temperatures collected from January 22 to January 26.

The heat values described in the following equations are obtained from the temperature instantaneous readings taken every 2 minutes in the measurements. The energy balance of the ventilation system in the room was accounted to calculate ventilation losses:

$$Q_{vent} = \sum_{i=1}^n \dot{m} \cdot c_p \cdot (T_{room,i} - T_{exterior,i}) \cdot \Delta t_i \quad (2.5)$$

Where:

- n is the number of readings within the entire time interval chosen in which the energy balance is carried out;
- Δt_i is the i -th time interval between two consecutive readings that is constant and equal to 2 minutes;
- \dot{m} is the constant air mass flow rate of 0.012 kg/s;
- c_p is air specific heat that can be considered practically constant whether it is valued in temperatures range of the system operating conditions and it is equal to 1013 J/kg K;
- $T_{room,i}$ is the i -th office room air temperature reading;
- $T_{exterior,i}$ is the i -th outside air temperature reading.

Thermal losses in the LHTES unit are calculated with Eq. (2.6):

$$Q_{PCM,loss} = \sum_{i=1}^n UA \cdot (T_{PCM\ avg,i} - T_{room,i}) \cdot \Delta t_i \quad (2.6)$$

Where:

- UA is the product of global heat transfer coefficient and heat exchange surface. Ostermann [33] found its theoretical value, neglecting convection phenomenon and considering only the conduction through the insulation, equal to 1.8 W/K;
- $T_{PCM\ avg,i} = (T_{PCM\ outlet,i} + T_{PCM\ inlet,i})/2$ is the i -th average air temperature along the storage. It approximates the temperature of the LHTES unit.

Thermal losses take place when temperature of the storage is higher than air room temperature and this happened most of the time and corresponds, using Eq.(2.6), to a positive value. Nevertheless, the heat exchange occurs in the opposite direction when the storage air temperature falls below room air temperature and a small heat recovery

is registered, but this phenomenon is practically negligible. Obviously, the thermal losses were higher during ventilation time and so when the air temperature in the storage was supposedly higher, as shown in Table 10. The highest value of 671 Wh was recorded on January 23 unlike the 15 Wh on January 26 when the solar radiation that heated the air was very limited and the storage was almost in thermal balance with the room.

	Heat losses [Wh]	
	From 9 am to 5 pm	All day
January 22	287	370
January 23	393	671
January 24	249	448
January 25	92	137
January 26	18	15
Tot.	1039	1640

Table 10. Heat losses values.

It can also be seen from Figure 30 that the temperature of the air exiting the storage, as soon as the fan was turned on at 9 am, was very close to that of the office room. This suggests that the storage during the 16 hours of no system operation, between two consecutive fan computations, lost nearly all the overall heat stored during sunshine hours.

The heat stored or released in the unit was determined with the equation below:

$$Q_{stor/rel} = \sum_{i=1}^n \dot{m} \cdot c_p \cdot (T_{PCM\ outlet,i} - T_{PCM\ inlet,i}) \cdot \Delta t_i + Q_{PCM,loss} \quad (2.7)$$

If the value of Eq.(2.7) is positive it means that the PCM is globally releasing heat and on the contrary, if the value is negative the PCM is storing thermal energy from hot air.

To obtain a comparison between the system with and without LHTES unit, the total heat gained was calculated according to Eq.(2.8) and Eq.(2.9):

$$Q_{total \text{ without storage}} = \sum_{i=1}^n \dot{m} \cdot c_p \cdot (T_{SAC \text{ outlet},i} - T_{exterior,i}) \cdot \Delta t_i \quad (2.8)$$

$$Q_{total \text{ with storage}} = \sum_{i=1}^n \dot{m} \cdot c_p \cdot (T_{PCM \text{ outlet},i} - T_{exterior,i}) \cdot \Delta t_i \quad (2.9)$$

Where $T_{SAC \text{ outlet},i}$ means the outlet air temperature from the solar collector. Effectively, the system with no storage means that the air would enter the room just after having left the SAC. The difference between the total heat gained with the use of the storage unit and the total heat without the use of the storage unit represents, neglecting the heat losses through the entire system, the heat stored or released in the PCM. Thus, if the latter difference is positive it means that the storage is releasing heat otherwise it is storing heat. Figure 31 gives information about parameters described in the previous equations in the ventilation time on each day.

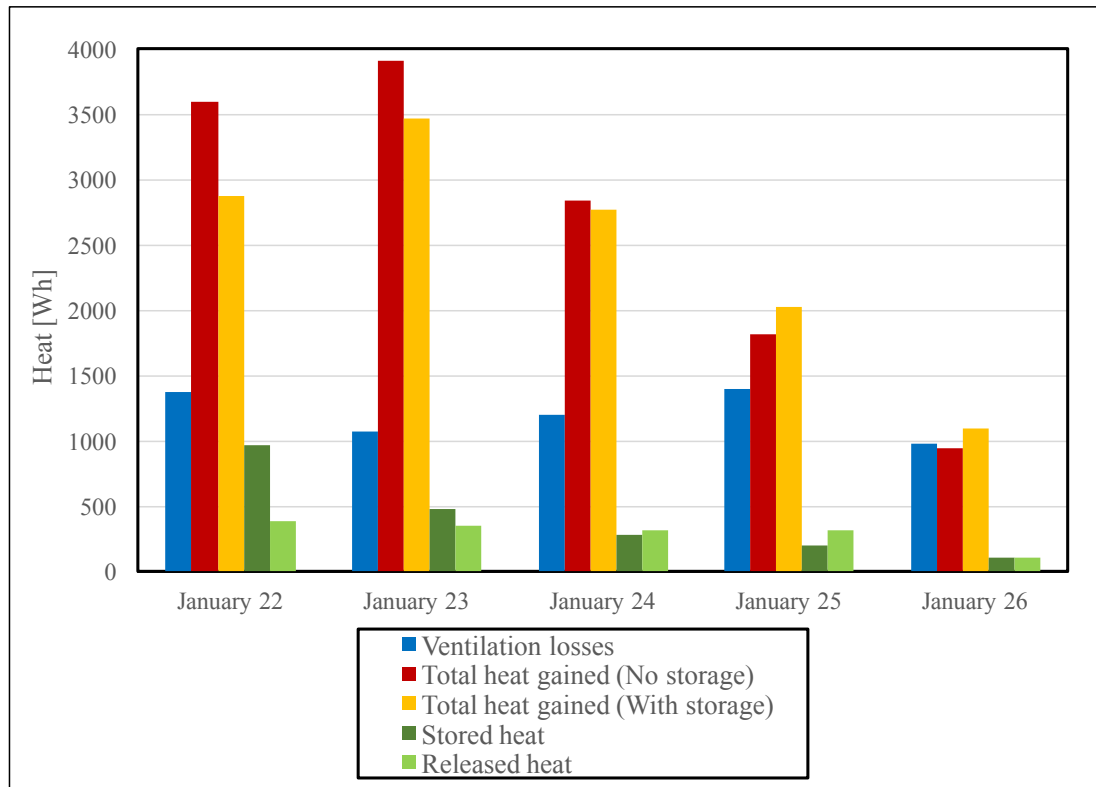


Figure 31. Heat values obtained from January 22 to January 26.

It is noticeable that the total heat of the solar collector on the first two days is markedly higher than the total heat with storage. This is because the heat stored from 9 am to 5 pm was higher than the released heat. By contrast, the total heat gained with the complete system is higher on January 25 because of higher released heat than stored. On January 24 and on January 26 the heat stored was very close to release heat and this is highlighted from almost equal values of both total heats (differences are due to imperfect evaluation of heat losses in the storage and from having neglected the heat losses in the ductwork that connects the SAC to the LHTES unit). Values are listed in Table 11 below.

	Heat required [Wh]	Total heat gained [Wh]		Stored/released heat [Wh]	
	Vent. Losses	No storage	With storage	Stored heat	Released heat
January 22	1373	3591	2876	968	384
January 23	1072	3904	3470	481	347
January 24	1196	2834	2769	282	319
January 25	1392	1818	2028	195	314
January 26	980	937	1091	107	106
Total	6013	13084	12233	2034	1470

Table 11. Main heat values from January 22 to January 26.

It is evident that the total heat gained, except for the system with no storage on January 26, is always higher than ventilation losses. This means that air gained sufficient energy to cover the ventilation losses on each day but the problem is that this energy is not well distributed in time and a part of this is inevitably lost. Leveling the mismatch in time between energy availability and energy demand is exactly the function of the storage. During the operation of the system, if the instantaneous value of the total heat gained, with or without the storage, is higher than ventilation losses, it means that the supplied air temperature is higher than the office room temperature. In this case, a surplus of heat is recorded and the excess of heat represents heat inevitably lost. Therefore, the useful heat corresponds to the ventilation losses because the surplus of heat would be wasted. On the other hand, if the instantaneous value of the total heat is lower than ventilation losses it means that the temperature of the supplied air is smaller than office room temperature and the difference between total

heat and ventilation losses corresponds to the additional heat, the air would need to reach the desired condition and, in this case, the useful heat is the total heat gained. Thus, the useful heat is calculated through the following equations (used for either systems, with or without the storage):

$$\dot{Q}_{useful,i} = \dot{Q}_{total,i} \quad \text{if } T_{outlet,i} < T_{room,i} \quad (2.10)$$

$$\dot{Q}_{useful,i} = \dot{Q}_{vent,i} \quad \text{if } T_{outlet,i} \geq T_{room,i} \quad (2.11)$$

$$Q_{useful} = \sum_{i=1}^n \dot{Q}_{useful,i} \cdot \Delta t_i \quad (2.12)$$

In the bar chart of Figure 32 the amount of useful heat on each day is shown and the values are reported in Table 12.

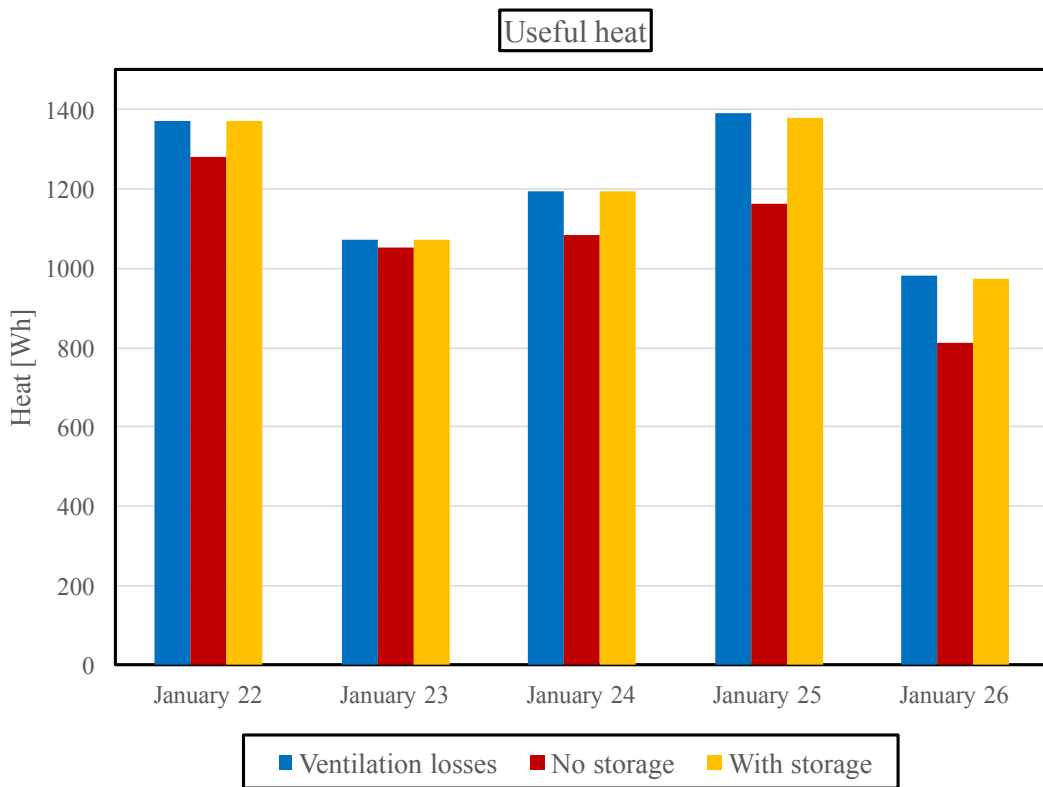


Figure 32. Comparison between useful heat of the system with and without the storage.

It is noticeable that useful heat of the system with the storage reached practically always the value of the heat required from ventilation losses. On the contrary, the

system with only the SAC almost achieved the desired conditions solely on the sunniest day (January 23). The higher daily difference is recorded on January 25, passing from 1161 Wh to 1380 Wh by adding the storage to the SAC with an increase of 219 Wh (+19%). Therefore, it can be seen how the storage decreased the mismatch between supply and demand from the growth of 11.2% of the total useful heat value throughout the 5 days, from 5390 Wh to 5996 Wh.

The coverage rate in Table 12 is obtained by dividing the useful heat with the correspondent value of ventilation losses and expresses the percentage of required heat for ventilation covered by the system. The system with the storage unit, throughout the 5 days, covered the ventilation losses almost that of the overall ventilation time against the 90% of the system with no storage unit. The percentage differences are more evident on January 25 and on January 26, when the solar radiation was not high and the only SAC was insufficient.

	Heat required [Wh]	Useful heat [Wh]		Coverage rate [%]	
	Ventilation Losses	No storage	With storage	No storage	With storage
January 22	1373	1281	1373	93%	100%
January 23	1072	1054	1072	98%	100%
January 24	1196	1082	1196	91%	100%
January 25	1392	1161	1380	83%	99%
January 26	980	812	975	83%	99%
Total	6013	5390	5996	90%	99%

Table 12. Useful heat and coverage rate results.

Reported in Table 13 is the time when the system guaranteed the total coverage of ventilation losses (it means the time when the supplied air temperature was at least equal to the room air temperature) and the percentage of time when this happened (if a time higher than 8 hours occurred it is because the fan wasn't switched on and off exactly from 9 am and to 5 pm respectively, and sometimes the ventilation time lasted some minutes more or some minutes less). The storage increased on each day, the time of total coverage with the largest difference recorded on January 26 with doubled coverage time (increased by 3.1 hours). The coverage time was high for the SAC system on the sunniest days but, in any case, the addition of the LHTES unit lead to a

complete coverage. The storage unit guaranteed 8,3 hours more of coverage, during the 5 days, respect to the system with only SAC with a total coverage time rate of 92% against the 71% of the system without the storage.

	Total coverage time [h]		Total coverage time rate [%]	
	No storage	With Storage	No storage	With Storage
January 22	6.8	8.5	80%	100%
January 23	7.0	7.6	93%	100%
January 24	6.4	7.5	85%	100%
January 25	4.4	6.2	56%	80%
January 26	3.1	6.2	40%	81%
Total	27.7	36.0	71%	92%

Table 13. Total coverage time and total coverage time rate resulted from the analysis of the system.

Additional heat is the external energy needed to reach room temperature when the total heat gained from the system is not sufficient to cover ventilation losses. It is obtained simply through the difference between ventilation losses and useful heat:

$$Q_{additional} = Q_{vent} - Q_{useful} \quad (2.13)$$

As expected, the system without the storage reached the smallest value of additional heat on January 23 because it was the day with the strongest solar radiation while the highest value was recorded on January 25 (Table 14).

	Additional heat [Wh]	
	No storage	With Storage
January 22	92	0
January 23	18	0
January 24	114	0
January 25	230	12
January 26	169	5
Total	622	17

Table 14. Additional heat.

On the other hand, the addition of the storage allowed to reach a complete self-sufficiency system during the first 3 days and very low values on the following two days. Overall, during the 5 days, the system with the storage unit needs only 17 Wh of additional heat, about 3% of the additional heat required for the system without the storage.

The effectiveness of the ventilation system was calculated through the ratio between the useful heat (Q_{useful}), whether it is the system with or without the storage, and the input electrical energy required by the fan ($E_{el.Fan}$):

$$\varepsilon = \frac{Q_{useful}}{E_{el.Fan}} \quad (2.14)$$

Finally, the global effectiveness of the ventilation system was, instead, defined as the ratio between the required heat for ventilation losses (Q_{vent}) and the sum of the input electrical energy ($E_{el.Fan}$) and the additional heat ($Q_{additional}$):

$$\varepsilon_{glob} = \frac{Q_{vent}}{E_{el.Fan} + Q_{additional}} \quad (2.15)$$

The values, including the energies required by the fan, are summarized in Table 15.

	El. Energy [Wh]	Effectiveness		Global effectiveness	
	Fan	No storage	With Storage	No storage	With Storage
January 22	55	23.5	25.1	9.4	25.1
January 23	48	21.8	22.1	16.2	22.1
January 24	49	22.2	24.6	7.4	24.5
January 25	50	23.4	27.8	5.0	22.7
January 26	49	16.5	19.8	4.5	18.1
Total	251	21.5	23.9	6.9	22.5

Table 15. Fan consumptions, effectiveness and global effectiveness.

Ideally, the fan input energies on each day should be equal but small differences are due to an imprecise duration of 8-hours ventilation time in the experiment. It is noticeable that the effectiveness is always larger than global effectiveness and the addition of the storage increased both. The highest difference is recorded on January 25 passing from 23 to 28 and from 5 to 23 regarding the effectiveness and the global effectiveness, respectively. Overall, the effectiveness rose by 2 points and the global effectiveness passed from 7 to 23, more than 3 times higher.

Chapter 3

TRNSYS SIMULATIONS OF THE SYSTEM

3.1 Introduction to TRNSYS simulation environment.

Before reporting the validations and the annual simulation, the chapter starts with a description of the numerical model implemented in the software either for the LHTES unit and for the SAC.

TRNSYS software is a complete and extensible simulation environment for the transient simulation of systems. The software is furnished under a license agreement. The license of TRNSYS 17 used as a simulation tool was provided by courtesy of University of Ljubljana, Faculty of Mechanical Engineering. The software provides about one hundred models of dynamic systems in its library and each component is accompanied by a concise overview and by explanations of mathematical algorithms [34], both are available in the TRNSYS manual. The components are displayed as TRNSYS Type in TRNSYS Simulation Studio that is the main visual interface of the software. Furthermore, the DDL-based architecture allows users and third-party developers to build, using all common programming languages as C++, component models to be used and connected (TRNSYS project is typically setup by connecting components graphically) to those already developed. Each Type of component has a set of matching Proforma in the Simulation Studio. The Proforma has a black-box description of a component: inputs, outputs, parameters, etc.

3.2 The numerical model of the LHTES unit.

A number of models for LHTES systems were applied and implemented by sundry researcher, for instance, Al-Saadi [35] and [36]. The numerical model of LHTES unit installed in Ljubljana was developed at the Brno University of Technology [37] and

implemented as a TRNSYS Type in the TRNSYS simulation tool in the form of a DDL-based architecture. The C++ programming language was used for its implementation.

The first assumption for the implementation of the numerical model, since air gaps between two CSM panels are geometrically the same, was to consider the same air mass flow rate in all air channels. The second assumption was to consider heat conduction exclusively in the direction of the thickness of the CSM panel. Such exemplification was due to the dimensions of the CSM panels. Indeed, the thickness of the panels is considerably smaller than their other two spatial dimensions and for this reason the largest temperature gradient is in the direction of the thickness. Thus, the numerical model was based on the implementation of the 1D heat transfer equation with an internal source of heat:

$$\rho c \frac{\partial T}{\partial t} = \frac{\partial}{\partial y} \left(k \frac{\partial T}{\partial y} \right) + \dot{Q} \quad (3.1)$$

Where:

- ρ represents the density of the PCM;
- c is the specific heat of the PCM;
- k stands for the thermal conductivity of the PCM;
- t is the time;
- T represents the temperature of the PCM;
- y is the spatial coordinate in the direction of the CSM plate thickness;
- \dot{Q} stands for the internal heat source of the latent heat of fusion.

The internal heat source of Eq.(3.1) can be expressed as follow:

$$\dot{Q} = \rho L_f \frac{\partial f_s}{\partial t} \quad (3.2)$$

Where:

- L_f denotes the latent heat of fusion;

- f_s is the solid fraction that represents the ratio between the solid and liquid phases.

The effective heat capacity method was utilized as an approach to modelling of the PCM. This method adopts the effective heat capacity in order to include the latent heat of fusion. The effective heat capacity can be defined as follows:

$$c_{eff}(T) = \frac{1}{\rho} \frac{\partial H}{\partial T} = c - L_f \frac{\partial f_s}{\partial t} \frac{\partial t}{\partial T} \quad (3.3)$$

Where H is the enthalpy of the PCM. Therefore, the more the enthalpy function is sloped in respect to the temperature, the higher the effective heat capacity.

By inserting Eq.(3.3) in Eq.(3.1) results the governing equation of 1D heat transfer equation in PCMs as follow.

$$\rho c_{eff} \frac{\partial T}{\partial t} = \frac{\partial}{\partial y} \left(k \frac{\partial T}{\partial y} \right) \quad (3.4)$$

The dependence of the effective heat capacity on the temperature for a material during phase change is shown in Figure 33.

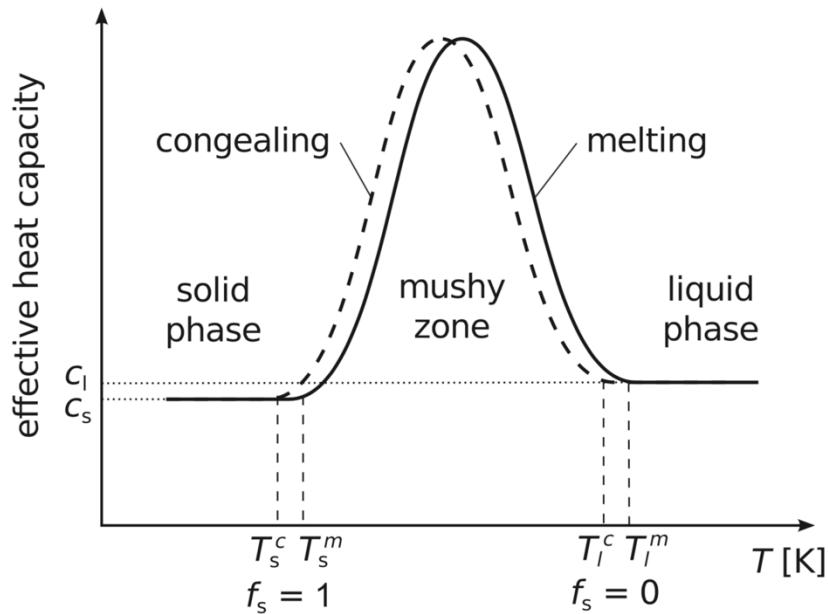


Figure 33. Effective heat capacity profile in respect to temperature [37].

The effective heat capacity corresponds to the respective specific heats in the liquid and solid states of the material outside of the phase change temperature range. The effective heat capacity significantly varies when the material undergoes phase change (when $0 < f_s < 1$) as it comprises the absorption or the release of the latent heat. Furthermore, Figure 33 illustrates the effective capacity for a material with the hysteresis of melting and solidification that is rather typical for most of the PCMs. The hysteresis complicates numerical modelling of the PCM thermal behavior when the material does not fully liquefy or solidify during the working cycle. In the simulated thermal storage cycle the PCM fully liquefied during the heat storage period and fully solidified in the heat discharge period; therefore, one effective heat capacity curve was used for melting and a different one for solidification. The effective heat capacity of Rubitherm RT22HC (Table 2) was proposed in the form of the Gaussian-shape function with both the solid and liquid specific heats of $2000 \text{ J kg}^{-1} \text{ K}^{-1}$. Thus, the effective heat capacity function valid during phase change temperature interval of Rubitherm RT22HC between 20 and 23 °C becomes:

$$c_{eff}(T) = 2000 + c_m \exp \left\{ -\frac{(T - T_{pch})^2}{0.5} \right\} \quad (3.5)$$

Where:

- c_m is the maximum increment of the specific heat due to the latent heat;
- T_{pch} represents the mean temperature of the PCM for melting and congealing.

The model of the LHTES unit built in TRNSYS requests the use of two distinct time steps. The iterations in respect to time in TRNSYS simulation follow the global time step Δt_{glob} specified by the user. Nevertheless, the model of the LHTES unit numerically approximates the time derivative in Eq.(3.4) through the explicit time discretization which is conditionally stable. The conditional stability requires that the maximum time step for the numerical solution is strictly limited. From the stability criteria it is possible to determine the maximum time step $\Delta t_{int,max}$ that is generally much smaller than the global time step added in TRNSYS. Therefore, the model of LHTES unit uses the internal time step Δt_{int} which is obtained as follows.

$$\Delta t_{int} = \frac{\Delta t_{glob}}{N_{t,int}} \quad (3.6)$$

Where $N_{t,int}$ stands for the number of the internal time iterations within the global time iteration and it is rounded off to the closest higher integer. It is calculated with the following equation:

$$N_{t,int} = \frac{\Delta t_{glob}}{\Delta t_{int,max}} \quad (3.7)$$

Figure 34 illustrates a scheme of a generic air gap between two adjacent CSM panels. The air channel can be divided into n -sections in the direction of the air flow (x -direction). Each node (red point in Figure 34) represents a particular section.

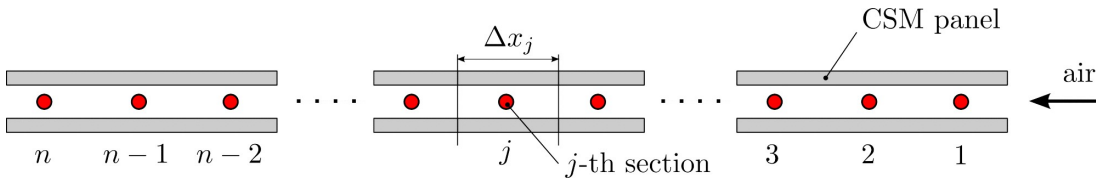


Figure 34. Schematic section of the air channel [36].

The solution of the thermal behavior in each section includes the use of the 1D heat transfer submodel described by Eq.(3.4). Figure 35 shows, specifically, the detail of the computational domain of the CSM panel of a generic section where the submodel is applied (along y -direction).

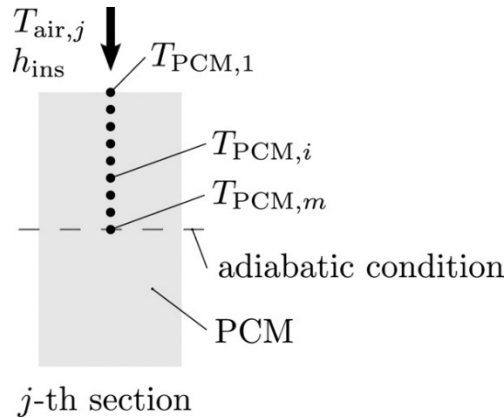


Figure 35. Scheme of the computational domain of the CSM panel [36].

The number of nodes and thus, the number of sections used for the calculations can be specified in the model. The calculation starts in the first section where the temperature of the node is considered equal to the inlet air temperature given as an input ($T_{air,1} = T_{air,in}$). Subsequently, the temperature of the following node $T_{air,2}$ is obtained from the energy balance applied to the previous node. For this reason, it is necessary to know the inlet air temperature $T_{air,1}$, the heat flux to/from the adjacent CSM panels ($Q_{PCM,1}$), and the heat loss to the surroundings ($Q_{loss,1}$). As soon as $T_{air,2}$ is known, the energy balance in the second node allows to obtain the $T_{air,3}$ and so on. This procedure along the air gap is illustrated in Figure 36.

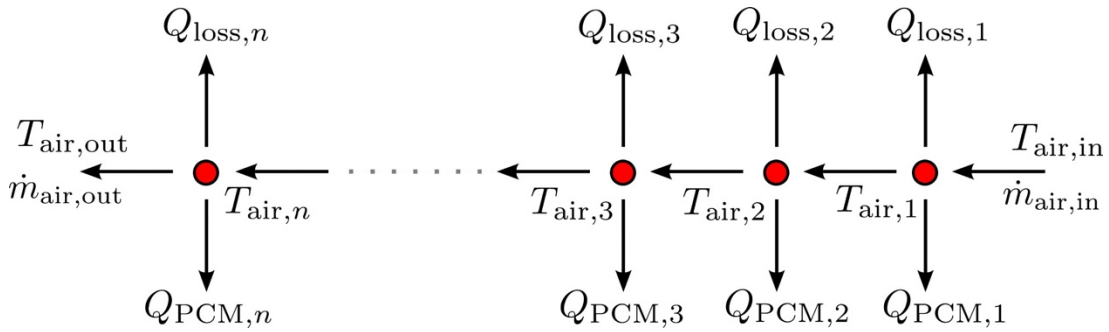


Figure 36. Scheme of the procedure followed in the numerical model [36].

The heat exchanged $Q_{PCM,j}$ (stored or released) between the PCM in the CSM panel and the air flowing the j -th section in the internal time iteration (Δt_{int}) is determined through the following relation:

$$Q_{PCM,j} = 2H\Delta x_j h_{ins}(T_{air,j} - T_{PCM,j})\Delta t_{int} \quad (3.8)$$

Where:

- H is the total length of the leading edge of all CSM panels;
- Δx_j is the length of the j -th section;
- h_{ins} is the heat transfer coefficient at the surface of the CSM panels;
- $T_{air,j}$ is the air temperature on the j -th node;
- $T_{PCM,j}$ is the j -th surface temperature of the CSM panel filled with the PCM.

The heat loss of the j -th section over the internal time step Δt_{int} is calculated with:

$$Q_{loss,j} = \Delta x_j P \left(\frac{T_{air,j} - T_{room}}{\frac{1}{h_{ins}} + \frac{R}{h_{outs}}} \right) \Delta t_{int} \quad (3.9)$$

Where:

- P is the cross section perimeter of the LHTES unit obtained in a plane perpendicular to the air flow direction (x-direction);
- T_{room} is the ambient temperature (office room temperature);
- R is the thermal resistance of the LHTES unit casing including the thermal insulation;
- h_{outs} is the heat transfer coefficient at the outer surface of the LHTES unit casing.

Finally, by making the energy balance the temperature of air flowing the j -th section is obtained as:

$$T_{air,j} = T_{air,j-1} - \frac{Q_{loss,j-1} + Q_{PCM,j-1}}{\dot{m} c_p \Delta t_{int}} \quad (3.10)$$

Where:

- \dot{m} is the air mass flow rate through the LHTES unit;
- c_p is the air specific heat.

3.3 Proforma of Type256 TRNSYS component.

The LHTES unit component built is saved as Type256 in TRNSYS simulation studio. The Type 256 proforma (that comprehends parameter, input and output values of the component) are listed in Table 16.

PARAMETER	Symbol	Value or symbol	Unit
Initial PCM temperature	$T_{PCM,in}$	-	[°C]
PCM heat conductivity	λ	0.2	[W m ⁻¹ K ⁻¹]
PCM density	ρ	730	[kg / m ³]
Mean temperature of PCM for melting and congealing	T_{pch}	21.5	[°C]
First parameter of the effective heat capacity	-	2000	[J kg ⁻¹ K ⁻¹]
Second parameter of the effective heat capacity	c_m	136000	[J kg ⁻¹ K ⁻¹]
Third parameter of the effective heat capacity	-	0.5	[K ²]
Ambient (room) temperature	T_{room}	20	[°C]
Thickness of CSM plate	-	0.015	[m]
Number of nodes in CSM plate	m	10	-
Length of CSM panel in the air flow direction	-	0.6	[m]
Cross section perimeter	P	1.68	[m]
Number of nodes along air flow direction	n	20	-
Thermal resistance of LHTES unit wall	R	0.5	[m ² K / W]
Number of CSM plates in one column	-	15	-
Heat transfer coefficient at the inner surface of the LHTES wall	h_{ins}	10	[W m ⁻² K ⁻¹]
Heat transfer coefficient at the outer surface of the LHTES wall	h_{outs}	10	[W m ⁻² K ⁻¹]
Air specific heat	c_p	1013	[J kg ⁻¹ K ⁻¹]
Total length of the leading edge of all CSM panels	-	0.45	[m]
INPUT			
Air mass flow rate	\dot{m}	0.012	[kg / s]
Inlet air temperature of the LHTES unit	$T_{air,in}$	-	[°C]
OUTPUT			
Outlet air temperature of the LHTES unit	$T_{air,out}$	-	[°C]
Heat losses in the LHTES unit	$Q_{loss,PCM}$	-	[J]
Heat stored/released in the LHTES unit	Q_{PCM}	-	[J]
Air mass flow rate	\dot{m}	0.012	[kg / s]

Table 16. TRNSYS proforma of the LHTES unit.

Parameters must be defined before starting the simulation and they are constant value except for the initial PCM temperature that corresponds to a boundary condition and must be chosen in respect to which PCM temperature user wants to start the simulation. Instead, input values can be modelled as constant values by deciding them before the run of the simulation or can be matched in the program to outlet values of other components of the simulation. Doing so, during the run of the simulation, the outlet value of the first component given in each time step of the transient is equal to the matched inlet value of the second component. Thus, the outlet values in Type256 can, in turn, be matched to inlet values of another Type in the simulation studio.

3.4 The numerical model of the solar collector.

The model of the solar collector implemented in the simulation was already present in the standard TRNSYS library. The Type 1b component was considered which represents a model of a flat-plate solar collector whose mathematical references are described in TRNSYS manual [34]. The thermal performance of the overall collector array is obtained by the number of modules in series and the features of each module. It is necessary to provide the efficiency function in respect to the ratio ($\Delta T/I_T$) of the temperature difference between HTF (air in this case) and ambient temperature (ΔT) to solar radiation (I_T). According to European Standards on solar collectors, the HTF temperature to insert is the average temperature in the collector, as shown in Eq.(3.11), if it is assumed that the efficiency versus the ratio $\Delta T/I_T$ curve can be modeled as a quadratic function:

$$\Delta t = t_{avg} - t_{amb} \quad (3.11)$$

Correction can further be applied to the slope, intercept and curvature parameters to account for the presence of heat exchanger, identical collectors in series, and flow rates other than those at test conditions. In Type1 there are also 4 possibilities for considering the effects of off-normal solar incidence. A general equation for solar thermal collector efficiency can be obtained from the Hottel-Whillier equation:

$$\eta = \frac{Q_u}{AI_T} = \frac{\dot{m}c_p(t_{outlet} - t_{inlet})}{AI_T} = F_R(\tau_\lambda\alpha_\lambda)_n - F_RU_L \frac{t_{avg} - t_{amb}}{I_T} \quad (3.12)$$

Where:

- η is the solar collector efficiency;
- Q_u stands for the useful energy gained by HTF in the solar collector;
- A is the collector aperture area;
- I_T is the global irradiation incident on the solar collector (tilted surface);
- F_R stands for the overall collector heat removal efficiency factor;

- $(\tau_\lambda \alpha_\lambda)_n$ is the product of the short-wave transmittance of the solar collector cover τ_λ and the short-wave absorptance of the absorber plate α_λ at the normal incidence;
- U_L is the overall thermal loss coefficient of the collector per unit area.

The overall thermal loss coefficient U_L is not exactly constant and a better expression is obtained by taking into account a linear dependency of U_L respect to the temperature difference $T_{avg} - T_{ambient}$. Thus, Eq.(3.12) becomes:

$$\eta = F_R(\tau_\lambda \alpha_\lambda)_n - F_R U_L \frac{t_{avg} - t_{amb}}{I_T} - F_R U_{L/T} \frac{(t_{avg} - t_{amb})^2}{I_T} \quad (3.13)$$

Where $U_{L/T}$ represents the thermal loss coefficient dependency on temperature.

Thus, Eq.(3.13) can be rewritten as:

$$\eta = a_0 - a_1 \frac{\Delta T}{I_T} - a_2 \frac{\Delta T^2}{I_T} \quad (3.14)$$

Where:

- a_0 it is called optical efficiency because it corresponds to the maximal efficiency of the solar collector and depends on the optical properties of the glazing and of the absorber;
- a_1 represents heat losses of the solar collector that identifies the slope of the efficiency curve. It is equal to the negative first-order coefficient in the solar collector efficiency equation;
- a_2 it is also a negative value but of the second-order coefficient in the efficiency equation.

Thus, equation (3.14) is the general equation of solar collector thermal efficiency used in TRNSYS Type 1b model, where a_0 , a_1 and a_2 are the coefficients to be determined as input data in the model. Parameter values were obtained from the solar collector test measurements at Fraunhofer [32], while the coefficients a_1 and a_2 were calculated using the equations in the discussed section.

3.5 Proforma of Type1b flat-plate solar collector component

The same conditions of Type256 are valid for the solar collector component. In Table 17 below are listed the parameter, input and output values associated to Type1b.

PARAMETER	SIMBOL	VALUE	UNIT
Number of collector in series	-	1	-
Solar collector area	A	1.638	[m ²]
Air specific heat	c_p	1013	[J kg ⁻¹ K ⁻¹]
Efficiency mode ¹	-	2	-
Mass flow rate in test conditions	-	130	[Kg h ⁻¹ m ²]
Optical efficiency	a_0	0.8	-
First-order coefficient	a_1	10.2	[W m ⁻² K ⁻¹]
Second-order coefficient	a_2	-0.0041	[W m ⁻² K ⁻²]
Optical mode of modification of non-normal incidence angle	-	2	-
First-order factor modifying a non-normal incidence angle in test conditions	-	0.2	-
Second-order factor modifying a non-normal incidence angle in test conditions	-	0	-
INPUT	SIMBOL	VALUE	UNIT
Air inlet temperature	t_{inlet}	-	[°C]
Air mass flow rate	\dot{m}	0.012	[kg / s]
Ambient temperature (external temperature)	t_{amb}	-	[°C]
Incident radiation (direct and diffuse) on the surface	-	I_T	[kJ h ⁻¹ m ⁻²]
Total solar radiation (direct and diffuse) on the horizontal surface	-	-	[kJ h ⁻¹ m ⁻²]
Diffuse radiation on the horizontal surface	-	-	[kJ h ⁻¹ m ⁻²]
Global reflectance or albedo of the environment (constant)	-	0.2	-
Incidence angle of solar radiation on the surface	-	-	[°]
Solar collector slope (constant)	-	90	[°]
OUTPUT	SIMBOL	VALUE	UNIT
Air outlet temperature	t_{outlet}	-	[°C]
Air mass flow rate	\dot{m}	0.012	[kg / s]
Useful energy	Q_u	-	[J]

¹ 2 is inserted if the efficiency parameters are given as a function of the average air temperature.

Table 17. TRNSYS proforma of Type1b

3.6 Validation of the LHTES unit model.

In order to validate the numerical model implemented in TRNSYS for the LHTES unit it is necessary to compare the data obtained in the measurements to the values resulting from the simulation. The aim is, indeed, to use the data from temperature measurements performed from November 30 to December 5 (Paragraph 2.4.1) as a means for this purpose. Figure 37 illustrates the scheme of the simulation viewed in TRNSYS Simulation Studio. Type9a in Figure 37 allows to read data from an external file at regular time intervals to make data available to other components as time-varying forcing functions. Each function read by Type9a correspond to a column of values in the external file and values from line to line must be at constant time intervals. Thus, two columns, one correspondent to data of inlet LHTES unit air temperature and one correspondent to the outlet LHTES unit air temperature obtained from temperature measurements, were copied in the external file and the value of the constant time interval equal to 2 minutes was set up in the parameters of Type9a because the measurements were collected every 2 minutes. Type65d in Figure 37 is an auxiliary component and it is not fundamental for the running of the simulation but it is used to display selected system variables while the simulation is processing to help the users immediately understand if the simulation is performing as desired (one Type65d was used to display the heat rates and one to display the temperatures). The calculator icon in Figure 37 named “Equa” is not a component but a TRNSYS tool that allows to collect functions as inputs and to use them to perform set calculations during the simulation. The new functions obtained from inputs can be used as outputs. Type25f is the printer component and it is used to print simulation information as a header in a set output file.

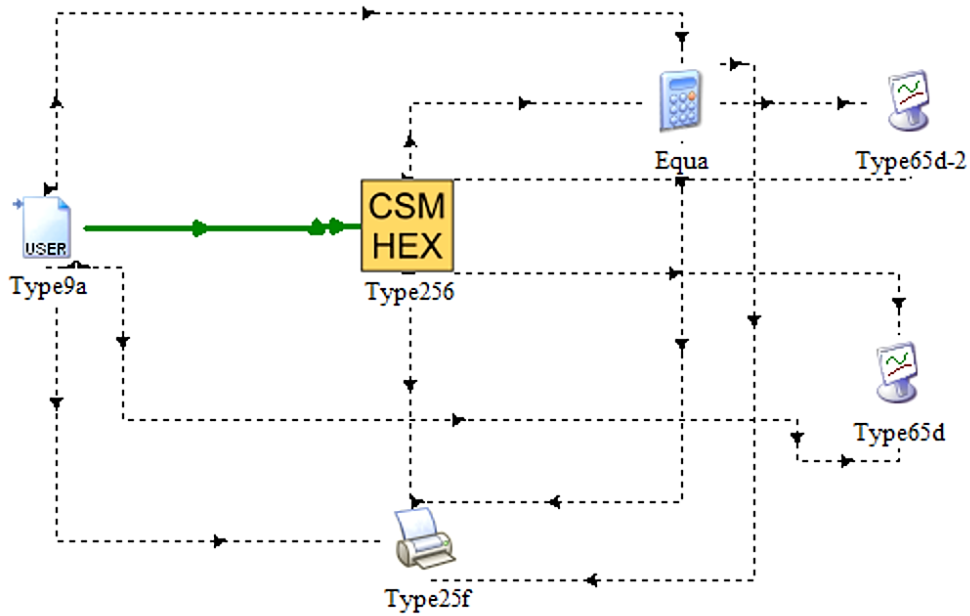


Figure 37. Scheme of the LHTES unit validation in TRNSYS software.

The lines (dashed or not) in Figure 37 show connections between different components and the arrows indicate the direction of the connection obtained by matching output/outputs of one component as input/inputs of the linked component.

The purpose of the validation is to compare the outlet LHTES unit air temperature obtained from experiments with the outlet LHTES unit air temperature given from the simulation, starting from the same inlet LHTES unit air temperature achieved from experiments.

Before starting, it was also necessary to define the time of the year from when the simulation had to start (00:00 am of November 30 corresponds to the 7992-th hour of the year) and the time of the year when the simulation had to end (00:00 am of December 6 corresponds to the 8136-th hour of the year) and a constant value of 0.012 kg/s air mass flow rate was imposed as input in Type256.

During the performing of the simulation, the LHTES unit component reads as input, in each time step, the inlet LHTES unit air temperature value from experiment given by Type9a and provides the correspondent value of the outlet air temperature resulted from the numerical model, and at the same time Type25f prints the value in the external file. This is repeated for all time steps until the simulation stop time is reached.

Figure 38 compares the resulted outlet LHTES unit air temperatures, both from experiment and from simulation for the same inlet LHTES unit air temperature. Immediately a good visual agreement between temperature profiles can be seen. Less discrepancies are visible mainly in the steeper part of the curve, in correspondent to the striking growth of the temperature when high solar radiation is present. On the other hand, higher differences are recorded when the slope of the curve is less marked and thus when the derivate of the temperature in respect to time increase or decrease quite slowly. This happens, above all, from when the solar radiation no longer reaches the surface of the collector (at around 5:30 pm on December 2, 3 and 5) and it happens in the down peaks (on December 4 and 5) that precede the sunshine hours. The one-dimensional assumption in the numerical model makes the storage component built in the simulation less affected by slow temperature changes and so it needs more time to reach the right slope of the experimental temperature curve. In any case, a good agreement between experiment and simulation is achieved. The absolute error ($e_{a,i}$), and the mean absolute error (MAE) are calculated as follows:

$$e_{a,i} = |T_{sim,i} - T_{exp,i}| \quad (3.15)$$

$$MAE = \frac{1}{n} \sum_{i=1}^n e_{a,i} = \frac{1}{n} \sum_{i=1}^n |T_{sim,i} - T_{exp,i}| \quad (3.16)$$

Where:

- $T_{sim,i}$ stands for the i-th simulation temperature;
- $T_{exp,i}$ stands for the i-th experiment temperature;
- n is the number of data take into account.

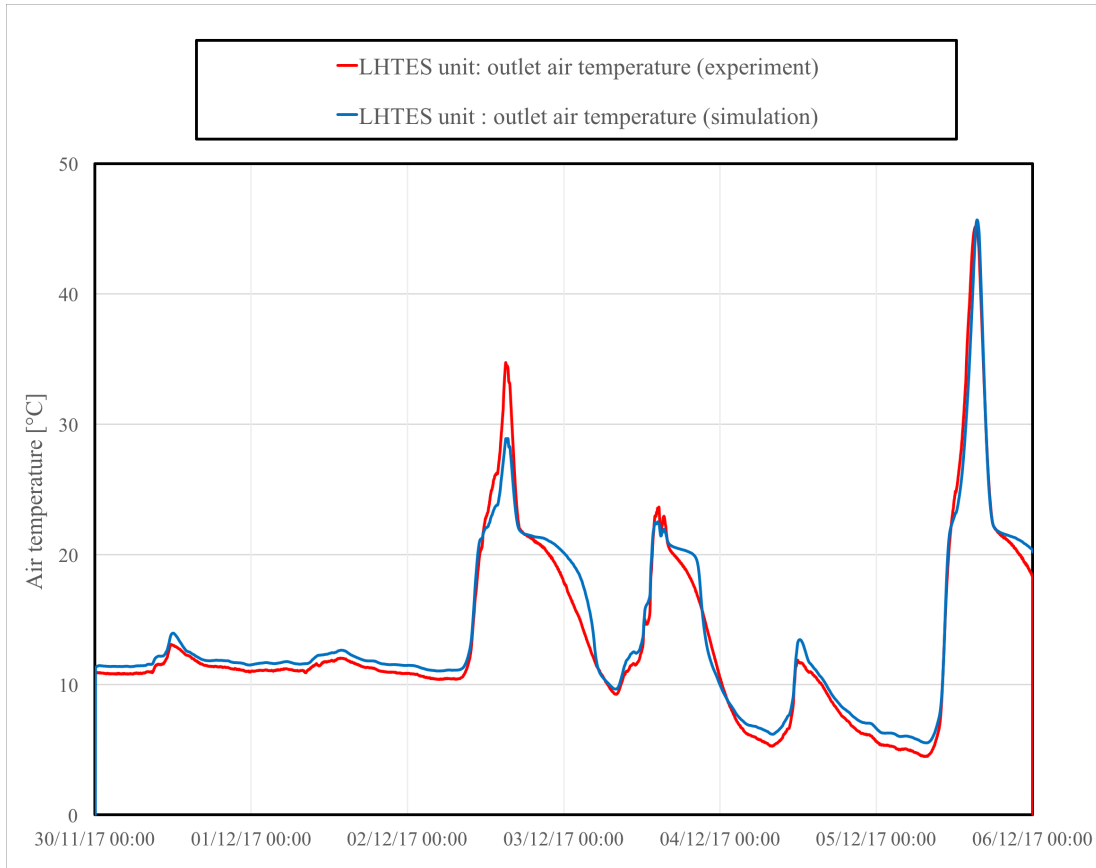


Figure 38. Validation of the LHTES unit.

The maximum absolute error ($e_{a,max}$) and the MAE , on each day and over the entire six days, due to simulation are summarized in Table 18.

Day	$e_{a,max}$ [°C]	MAE [°C]
November 30	0.9	0.5
December 1	0.8	0.6
December 2	5.9	1.2
December 3	3.4	1.3
Dcember 4	1.8	0.8
December 5	4.4	1.1
Total	5.9	0.9

Table 18. Errors between experiment and simulation.

Though the maximum value of the absolute error is equal to 5.9 °C, found at 3:33 pm on December 2 in correspondence to the daily temperature peak, a general agreement is recorded. Indeed, it is noticeable that the MAE is very low on each day with an overall value of 0.9 °C throughout the six days and with a maximum value greater only of 0.4 °C reached on December 3. The latter implies a good agreement with the data.

3.7 Validation of the solar air collector.

A second validation was performed to verify the agreement of the SAC model. Data was always taken from measurements performed from November 30 to December 5. The scheme as it appears in TRNSYS software is shown in Figure 39. Type9a read an external file which included the data of the ambient temperature, the inlet solar collector air temperature, the outlet solar collector air temperature, the total solar radiation on the horizontal surface and the diffuse radiation on the horizontal surface. The first three were taken from experiment measurements and the last two data were collected from the archives of the Slovenian Environmental Agency (Agencija Republike Slovenije za Okolje-ARSO) available on the site [38].

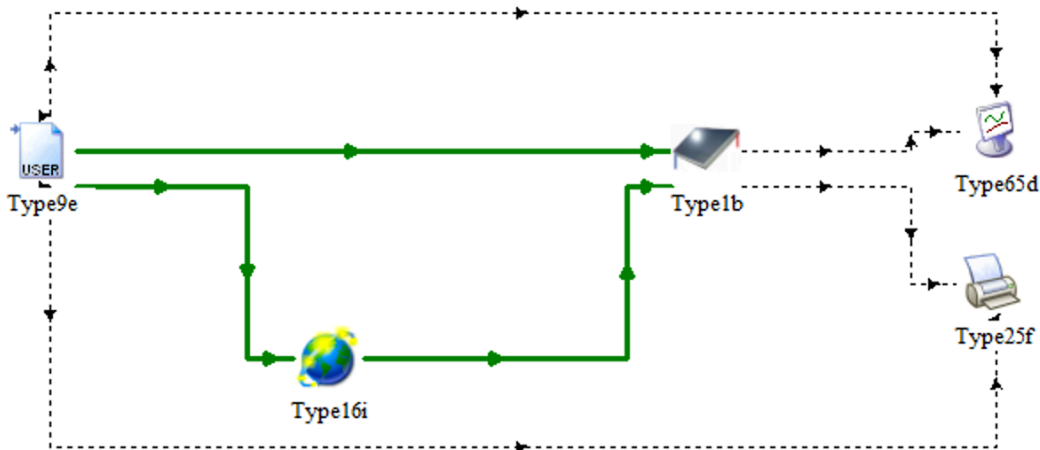


Figure 39. Scheme of the SAC validation in TRNSYS software.

The solar radiation data available from ARSO are collected in a meteorological station based in Bežigrad (Ljubljana) close to the Faculty of Mechanical Engineering. Each radiation data in ARSO is reported taking into account a time frame of 30 minutes and for this reason the temperature data obtained from experiment was adapted to this time step by averaging temperatures every 30 minutes. The total solar radiation and the diffuse radiation on the horizontal surface are taken as input functions by Type16. Starting from these and inserting known fixed orientation parameters, Type16 can estimate radiation on titled surfaces as the one of the solar collector installed in Ljubljana. In Type16 the latitude of Ljubljana (46.05°), the slope of the collector surface (it is vertical and so it is equal to 90°), the azimuth of collector surface (it is the angle between the projection of the normal of the collector surface into the horizontal plane and the local meridian and this is equal to 17°) and a constant value of the global reflectance (equal to 0.2) were imposed. Therefore, the inputs of solar collector Type1b (Table 17) are covered by Type9e concerning the ambient and the inlet air temperature while the inputs concerning the solar radiation are fully covered by Type16 and only air mass flow rate and the global reflectance constant and equal to 0.012 kg/s and 0.2, respectively were imposed. Type25f printed results of the simulation on an external file.

The comparison between the solar collector outlet air temperature obtained either through experiment and through simulation is shown in Figure 40.

The visual agreement is less marked than that of the LHTES unit validation. The two curves maintain a small offset that underestimate the outlet air temperature in simulation of about 3°C in no solar radiation hours while high absolute errors are recorded in correspondence of solar radiation peaks. As shown in Table 19, the maximum absolute error over the 5 days is 21.5°C reached on December 5 but also values of 20.5 and 15.8 were recorded on December 3 and December 2, respectively. Though these values are high, the MAE are sharply lower and this is a sign of bad results restricted only within sun peaks. December 5 is the worst day both for the MAE (6.9°C) and for the maximum absolute error and this confirms that high sun radiation worsens the results of simulation. The MAE throughout the 6 days is 4.4°C and though it is not as good as that of LHTES unit validation, it is, in any case, an acceptable value to validate the model.

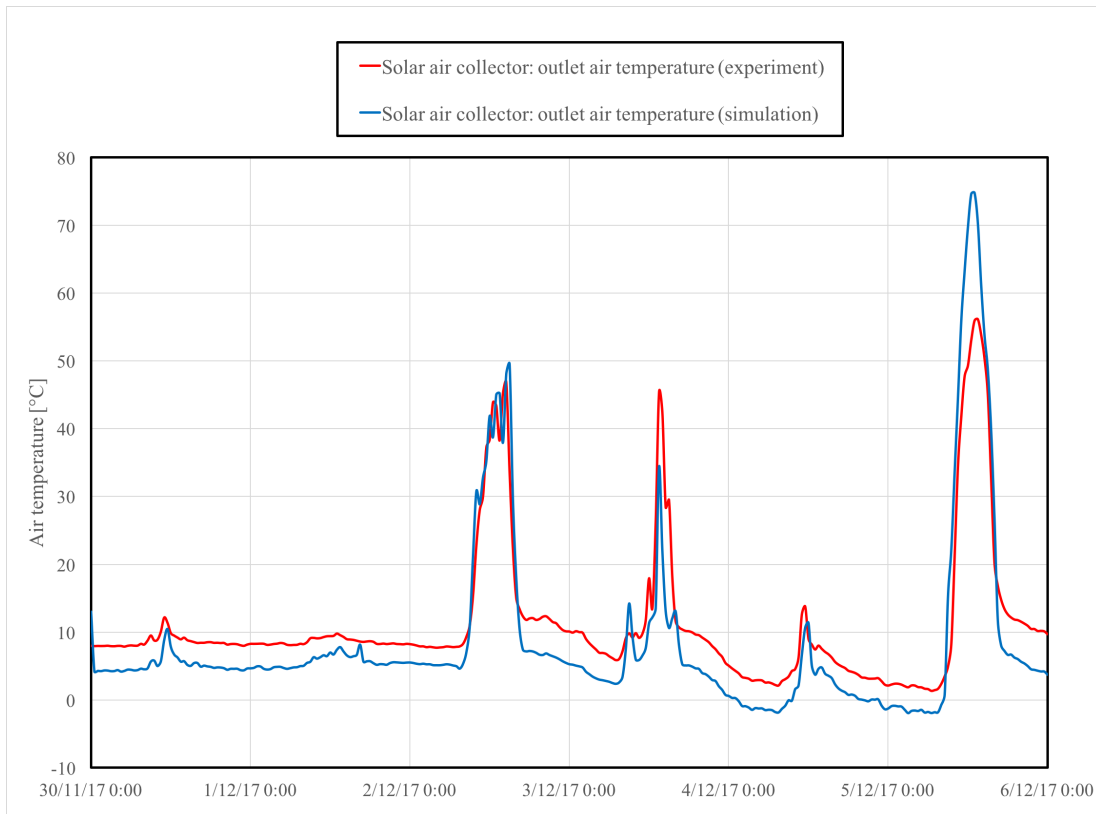


Figure 40. Validation of the SAC.

Day	$e_{a,max}$ [°C]	MAE [°C]
November 30	4.4	3.5
December 1	3.7	3.0
December 2	15.8	4.1
December 3	20.5	5.4
Dcember 4	6.0	3.7
December 5	21.5	6.9
Total	21.5	4.4

Table 19. Error values for the solar collector validation.

3.8 Addition of an air recuperator in the system.

Before analyzing the system throughout the year, it had evaluated the possibility to increase the performance of the system by adding an air recuperator in the TRNSYS simulated system. The purpose was to evaluate, with the simulation, the improvements that the system could make with the factual introduction of the air recuperator to lead to future developments.

A Type5e component from TRNSYS library was chosen that is a cross flow (both sides unmixed) sensible heat exchanger. A scheme of the heat exchanger is shown in Figure 41. The cold side (subscript “c”) fluid and the hot side (subscript “h”) fluid are distinguished. The capacitances of cold and hot side of the heat exchanger are calculated with:

$$C_c = \dot{m}_c c_{pc} \quad (3.17)$$

$$C_h = \dot{m}_h c_{ph} \quad (3.18)$$

Where:

- C_c is the capacitance of the cold side fluid;
- C_h is the capacitance of the hot side fluid;
- \dot{m}_c is the mass flow rate of the cold side;
- \dot{m}_h is the mass flow rate of the hot side;
- c_{pc} is the specific heat of the cold side fluid;
- c_{ph} is the specific heat of the hot side fluid.

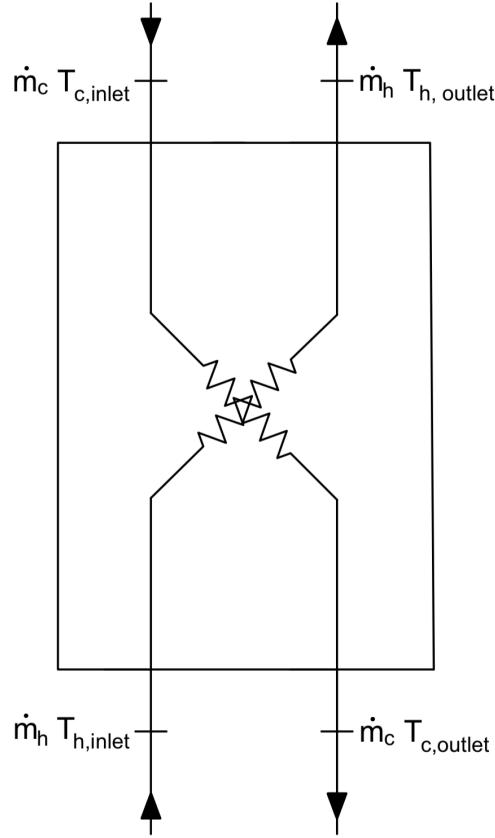


Figure 41. Scheme of the recuperator.

The model relies on an effectiveness minimum capacitance approach and by setting the heat exchanger overall heat transfer coefficient, the model calculates the effectiveness of the heat exchanger. The equation used to calculate the effectiveness of the heat exchanger in the model is:

$$\varepsilon = 1 - \exp \left[\left(\frac{C_{max}}{C_{min}} \right) \left(\frac{UA}{C_{min}} \right)^{0.22} \left\{ \exp \left[- \frac{C_{min}}{C_{max}} \left(\frac{UA}{C_{min}} \right)^{0.78} \right] - 1 \right\} \right] \quad (3.19)$$

Where:

- C_{max} is the maximum value between C_c and C_h ;
- C_{min} is the minimum value between C_c and C_h ;
- UA is the overall heat transfer coefficient of the heat exchanger.

In this case, the same fluid (air) and the same flow rate (0.012 kg/s) on both sides are taken into account and then, C_c C_h and C_{max} C_{min} are coincident. Type5e proforma is shown in Table 20.

PARAMETER	SIMBOL	VALUE	UNIT
Cross flow mode ¹	-	5	-
Specific heat of hot side fluid	c_{ph}	1013	[J kg ⁻¹ K ⁻¹]
Specific heat of cold side fluid	c_{pc}	1013	[J kg ⁻¹ K ⁻¹]
INPUT	SIMBOL	VALUE	UNIT
Hot side inlet temperature	$T_{h,inlet}$	20	[°C]
Hot side flow rate	\dot{m}_h	0.012	[kg / s]
Cold side inlet temperature	$T_{c,inlet}$	-	[°C]
Cold side flow rate	\dot{m}_c	0.012	[kg / s]
Overall heat transfer coefficient	UA	107	[W / K]
OUTPUT	SIMBOL	VALUE	UNIT
Hot side outlet temperature	$T_{h,outlet}$	-	[°C]
Hot side flow rate	\dot{m}_h	0.012	[kg / s]
Cold side outlet temperature	$T_{c,outlet}$	-	[°C]
Cold side flow rate	\dot{m}_c	0.012	[kg / s]
Heat transfer rate	\dot{Q}_{rec}	-	[kJ / h]
Effectiveness	ε	0.8	-

¹ Refers to the general heat exchanger model and 5 indicates a cross flow arrangement with both fluids unmixed.

Table 20. Type5e TRNSYS proforma.

Nowadays, the effectiveness of air recuperators reach values even higher than 90% but for this analysis an effectiveness of 80% was chosen which, following the model described through Eq.(3.19), is maintained constant by a constant value of the overall heat transfer coefficient. Thus, the value of the overall heat transfer coefficient as input (Table 20) was set up to reach the value of effectiveness desired. The effectiveness of the recuperator can be calculated also from the general effectiveness equation used for heat exchanger:

$$\varepsilon = \frac{\dot{Q}_{rec}}{\dot{Q}_{max}} = \frac{C_c(T_{c,outlet} - T_{c,inlet})}{C_{min}(T_{h,inlet} - T_{c,inlet})} = \frac{C_h(T_{h,inlet} - T_{h,outlet})}{C_{min}(T_{h,inlet} - T_{c,inlet})} \quad (3.20)$$

Where:

- \dot{Q}_{rec} is the heat transfer rate in the recuperator (Table 20) that can be found whether for the hot side fluid or for the cold side fluid;

- \dot{Q}_{max} stands for the maximum heat theoretically obtainable.

The case studied here takes into account the same fluid (air) and the same flow rate (0.012 kg/s) on both sides and thus the effectiveness can simply be calculated with:

$$\varepsilon = \frac{\dot{Q}_{rec}}{\dot{Q}_{max}} = \frac{(T_{c,outlet} - T_{c,inlet})}{(T_{h,inlet} - T_{c,inlet})} \quad (3.21)$$

The placement of the air recuperator in the system was thought just after the solar collector. Air exiting the solar collector reach the inlet cold side of the recuperator while a second fan draws air from the room at constant temperature of 20 °C in the recuperator inlet hot side. As both air sides have exchanged heat in the recuperator, the outlet cold side air reaches the LHTES unit and, on the other hand, the outlet hot side air is pushed out from the room to the external ambient. Doing so, heavy air that needs to be changed, exchanges heat with the fresh air before it is expelled from the room. For this reason, the hot side air inlet temperature was set up constant and equal to 20 °C (see inputs in Table 20).

To obtain an optimal use of the recuperator it was also thought that a control system, after having read the temperature of air exiting the solar collector, would command the second fan on the hot side of the recuperator to work. In particular, if the outlet air temperature from the solar collector is lower than 18°C the control system actuates the fan to have, at least, a sufficient temperature difference to let heat be exchanged and, on the contrary, if the outlet air exiting the solar collector is higher or equal to 18°C the fan is off and the fresh air leaves the recuperator without having exchanged heat. The operating scheme of the new system, referred to ventilation time from 9am to 5 pm (as experimented in Paragraph 2.6), is shown in Figure 42. On the contrary, as already shown in temperature measurements, in the simulated ventilation time, air is virtually supplied to the office room. Applying the mass balance means to consider air flow supplied equal to air flow extracted from the room and so when the recuperator is not working, air is considered taken from the room from the outlet duct through natural ventilation.

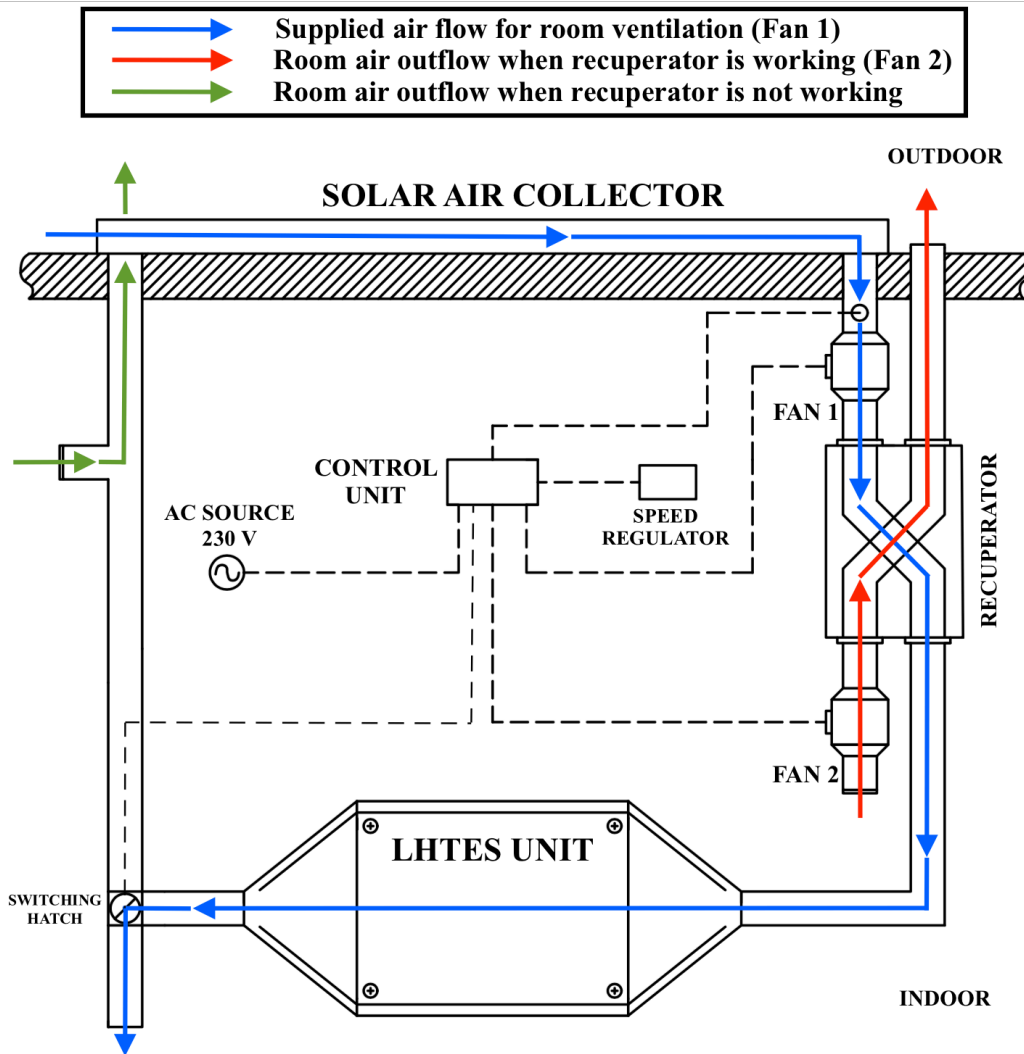


Figure 42. Scheme of the system with recuperator in TRNSYS simulations.

Before analyzing the system throughout the overall heating season the working of the system described in Figure 42 along the 6 days of temperature measurements was evaluated. The scheme of the system as it appears in TRNSYS software is shown in Figure 43. Type65d were removed simply to have a better clearness in the picture. Differently from validations, this time it was necessary to insert information about ventilation time for which air mass flow rate in the system is not constant throughout the day but it was 0.012 kg/s from 9 am to 5 pm and it was zero the remaining hours. Following this purpose, Type14 was inserted, which can employ a time dependent forcing function, which has a behavior characterized by a repeated pattern as the air mass flow rate function that was required to insert. Thus, the outlet set up function

solar collector outputs. The outlet cold side temperature is read as inlet value in the LHTES unit model.

The functioning of the simulated system from November 30 to December 5 is illustrated in Figure 44 where both curves relative to the inlet (outlet of collector) and outlet cold side air temperature with also the profile of fan 2 air mass flow rate along the time are inserted.

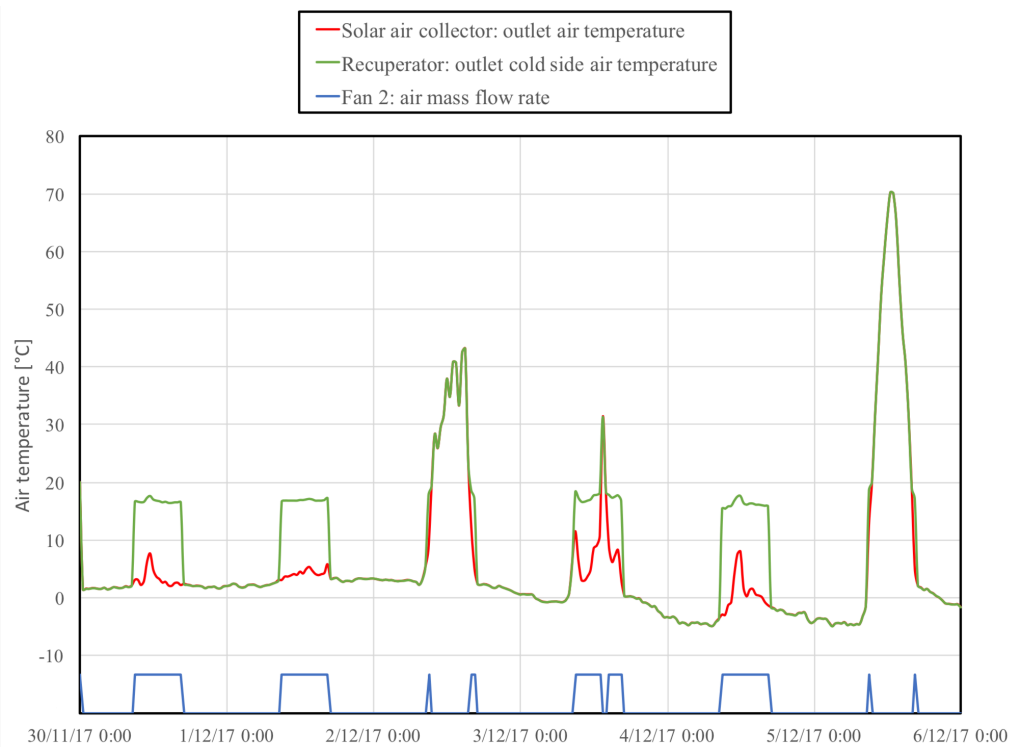


Figure 44. Working of the recuperator in the simulated system.

The control system worked perfectly. Indeed, fan 2 switched to off power during no ventilation hours and when the solar collector outlet air temperature was higher than 18 °C. Clearly, when fan 2 is not working the solar collector outlet air temperature coincides with the recuperator outlet cold side air temperature. On November 30, December 1 and December 4, fan 2 operated in the overall ventilation hours due to the absence of solar radiation that heated the air and then, on those days, the recovered heats from the heat exchanger, shown in Table 21, are the highest. On the other hand, on December 2 and December 5 the recuperator functioning showed its minimum influence limited to the first and the last 30 minutes of the ventilation time.

	Recovered heat [Wh]
November 30	1297
December 1	1230
December 2	167
December 3	905
December 4	1487
December 5	109
Total	5194

Table 21. Recovered heat.

3.9 Annual simulations.

Once models were validated the performance of the system throughout the year was evaluated. The yearly simulation was realized both for the current system installed in Ljubljana (SAC and LHTES unit) and for the system described in the previous paragraph constituted by SAC, recuperator and LHTES unit.

Figure 45 and Figure 46 show the scheme of the yearly simulation of the system composed of SAC and LHTES unit and the system composed of solar collector, recuperator and LHTES unit, respectively. The yearly weather and radiation files distributed with TRNSYS are generated using Meteonorm software that collects data from more than 1000 worldwide weather stations. Files are available in TMY2 (Typical Meteorological Year) standardized format which are composed of data sets of stochastic hourly values of solar radiation and meteorological elements for one year period. Thus, these values represent typical rather than extreme conditions of a general worldwide location. The function of Type15 on both Figure 45 and Figure 46 is to read the file referred to Ljubljana available in TRNSYS directory to have the typical hourly meteorological and radiation values throughout the year. Once orientation parameters of the solar collector (slope of the collector surface equal to 90° and azimuth of collector surface equal to 17°) were set in Type15, the solar collector model could read all the inputs from Type15. The function of Type14h is to simulate the fan working exclusively over the ventilation hours.

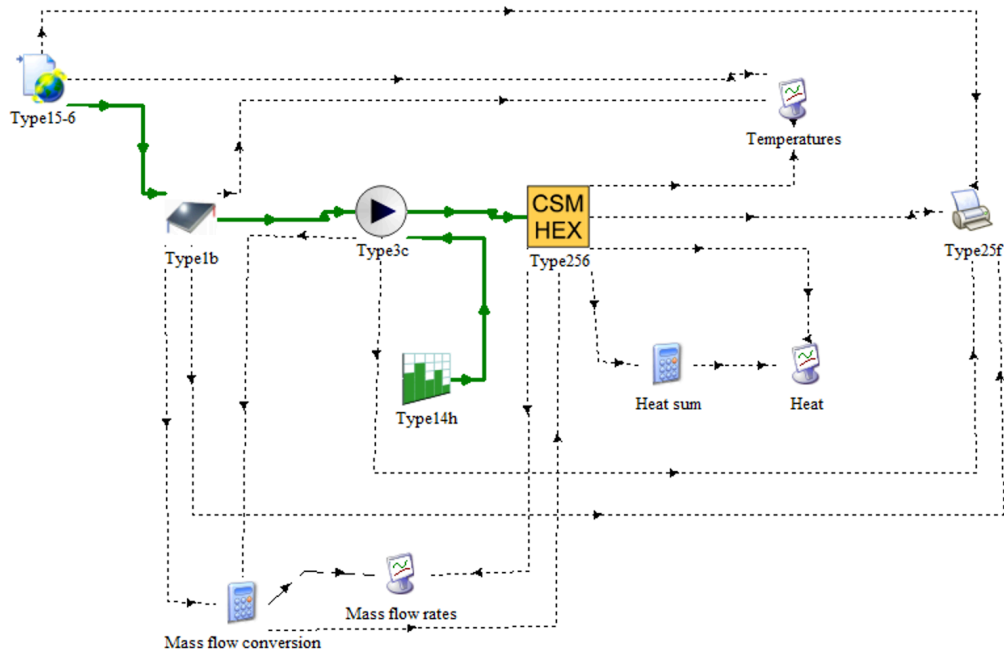


Figure 45. Annual simulation of the system composed of solar collector and LHTES unit.

Following the standardized format of the file a simulation time step of 1 hour was set up and because the simulation needed to be performed annually the simulation start time was the first day of the year and the simulation stop time the 365th day of the year.

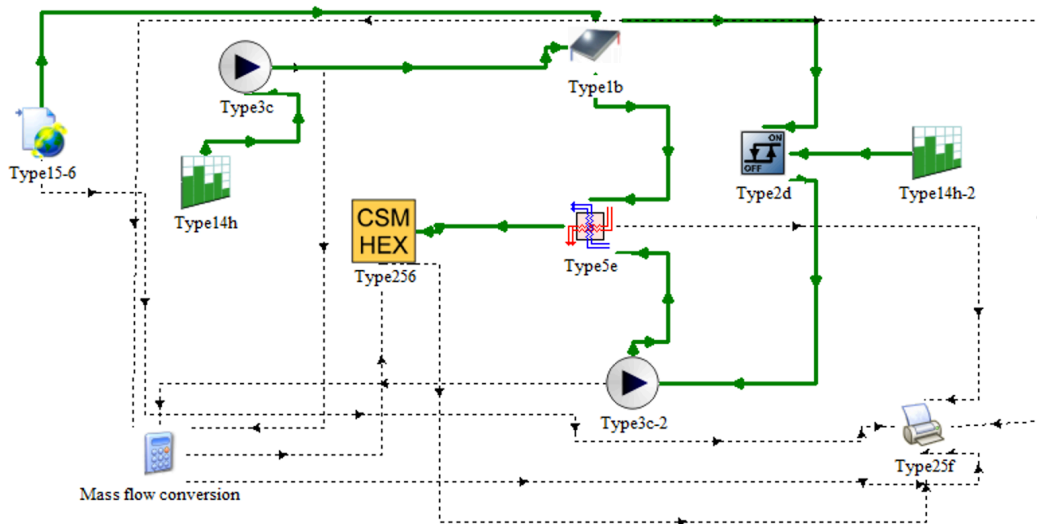


Figure 46. Annual simulation of the system composed of solar collector, recuperator and LHTES unit.

3.9.1 Results

The aim of this work is to evaluate the performance of the system in the heating season and for this reason the results obtained throughout the year were filtered reporting exclusively the presumable heating season months for Ljubljana, from October to April. The results are shown taking into account the equations described in Paragraph 2.6. What really changes using equations in Paragraph 2.6 is that discretization time (Δt_i) was one hour for yearly simulations (differently from 2 minutes time step of measurements), the LHTES unit thermal losses are automatically considered in the evaluation of the heat stored/released of Eq.(2.7) from the mathematical model implemented in the software, and the office room temperature ($T_{room,i}$) is virtually constant and equal to 20 °C. The results are shown comparing three different systems as summarized in Table 22. The system outlet air temperature is considered to evaluate the total heat gained in Eq.(2.8) or in Eq.(2.9) and the useful heat through Eq.(2.10), Eq.(2.11) and Eq.(2.12).

	System		
	Solar air collector	Solar air collector and LHTES unit	Solar air collector, recuperator and LHTES unit
Simbol	SAC	SAC+LHTES	SAC+REC+LHTES
System outlet air temperature - Air temperature supplied to the room	Is the outlet air temperature from solar air collector	Is the outlet LHTES unit air temperature obtained in simulation of Figure 45	Is the outlet LHTES unit air temperature obtained in simulation of Figure 46

Table 22. The three systems compared in the heating season simulation

Figure 47 shows the external temperature and the outlet air temperatures of each system ordered from the largest to the smallest value and taken exclusively in the ventilation hours throughout the overall heating season (from October to April).

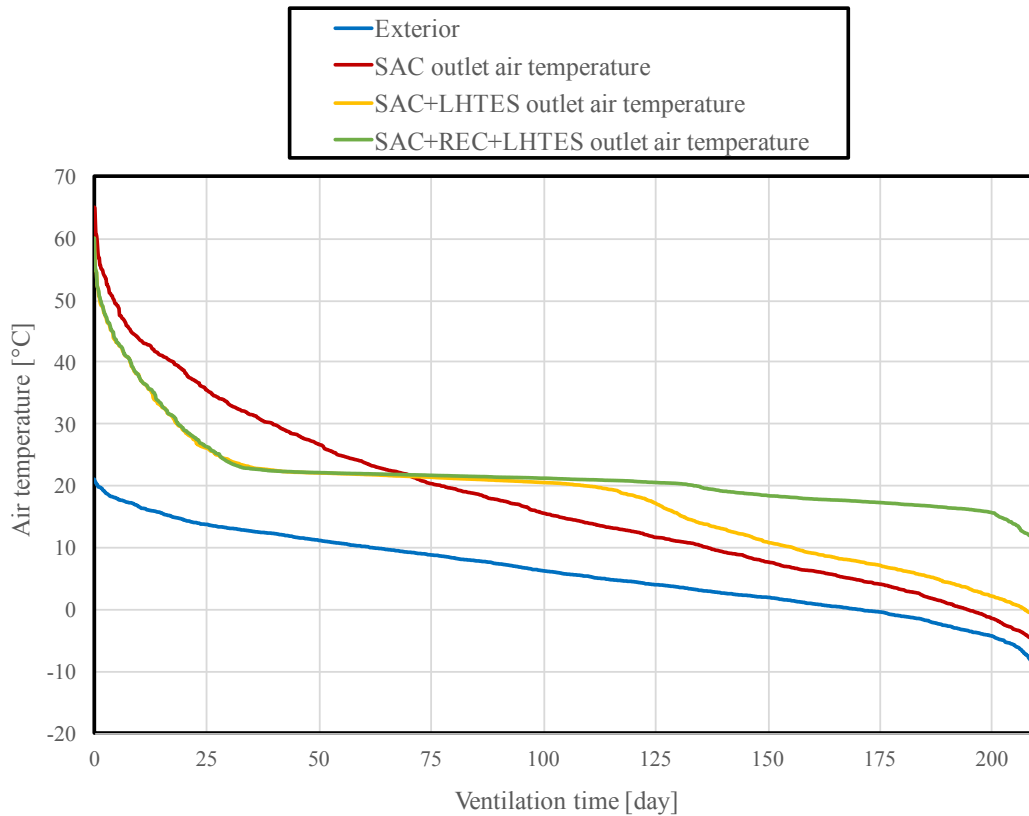


Figure 47. Outlet air temperatures for different systems during ventilation time.

It is noticeable that adding the LHTES unit to the SAC not only levels the temperature range between the highest and lowest heating season air temperature but the LHTES unit, and particularly the PCM melting point close to the desired room temperature, increased the frequency with which the supplied air temperature was found at around 20°C, about the 36% of the total ventilation time. Further adding the recuperator, the curve SAC+LHTES recorded an improvement in the part characterized by lower temperatures with a further leveling of the curve around the 20 °C. The system with the recuperator reached the design ventilation temperature about half of the total ventilation time. The orange and the green curves are coincident for almost all of the first part because the recuperator does not work with temperatures higher than 18 °C. All data in the following tables and figures are reported taking into account only the ventilation time.

The bar chart of Figure 48 shows the levels of total heat gained for each system in each month of the heating season compared with the heat required by ventilation losses and Table 23 reports the results.

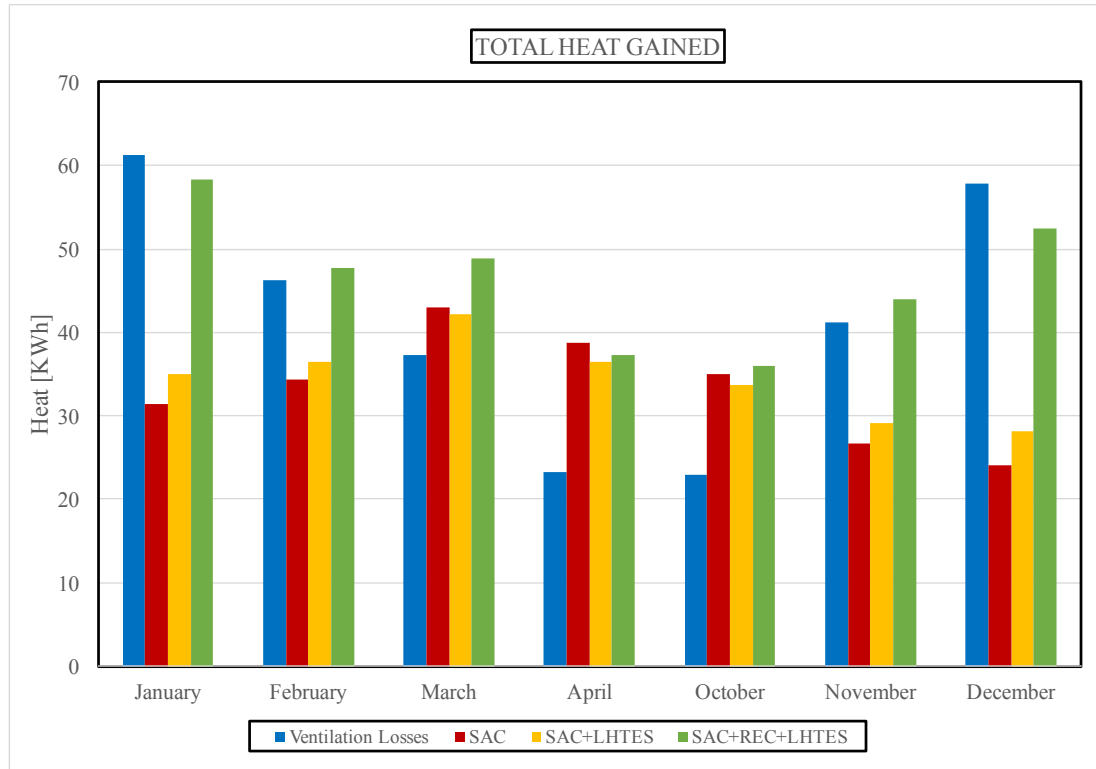


Figure 48. Total heat gained for each kind of system in the heating season.

The higher the level of ventilation losses the colder the month associated and vice versa. The total heat gained for the SAC and SAC+LHTES systems is higher than the ventilation losses only for the hotter months that are March, April and October while the system with air recuperator for all months except for the colder ones that are January and December and where the highest total heat gained differences between the first two system and the third one (almost twice in January and doubled values in December) are shown.

	Required [kWh]	Total heat gained [kWh]		
	Ventilation Losses	SAC	SAC+LHTES	SAC+REC+LHTES
January	61.2	31.4	34.9	58.4
February	46.2	34.3	36.5	47.7
March	37.3	43.1	42.1	48.9
April	23.3	38.8	36.5	37.3
October	22.9	35.0	33.6	36.1
November	41.3	26.6	29.1	43.9
December	57.8	24.1	28.2	52.4
Heating season	289.9	233.2	240.9	324.6

Table 23. Total heat gained resulted from the annual simulations.

In order to show values of the recuperator weight in the system, Table 24 reports the recovered heat, the hours and the percentage of usage of the recuperator in each month and over the entire heating season. As already confirmed from the previous total heat gained values, the air recuperator worked mainly in January (30.8 KWh of recovered heat with a usage that covered 79% of the global ventilation time) and in December (31.4 KWh of recovered heat with a usage that covered the 82% of the global ventilation time) while its influence on the system was restricted in April (3.3 KWh of recovered heat, about the 10% of the colder months and a rate of usage time of 22%) and in October. Its positive influence is marked by the overall heating season values, with a global recovered heat of 119,8 KWh (about the 41% of the global heating season ventilation losses) and a usage time of 58% of the time throughout the entire heating season.

	Recovered heat [KWh]	Recuperator usage time [h]	Recuperator usage time rate [%]
January	30.8	196	79%
February	17.4	149	67%
March	11.1	117	47%
April	3.3	53	22%
October	5.6	93	38%
November	20.2	172	72%
December	31.4	203	82%
Heating season	119.8	983	58%

Table 24. Values associated to the recuperator throughout the heating season.

The bar chart of Figure 49 gives information about the heat stored and released from the LHTES unit, either for the SAC+LHTES system and the SAC+REC+LHTES system, instead Table 25 reports the correspondent values. Regarding the SAC+LHTES system, the released heat in the colder months is higher than the stored heat differently as recorded in March, April and October.

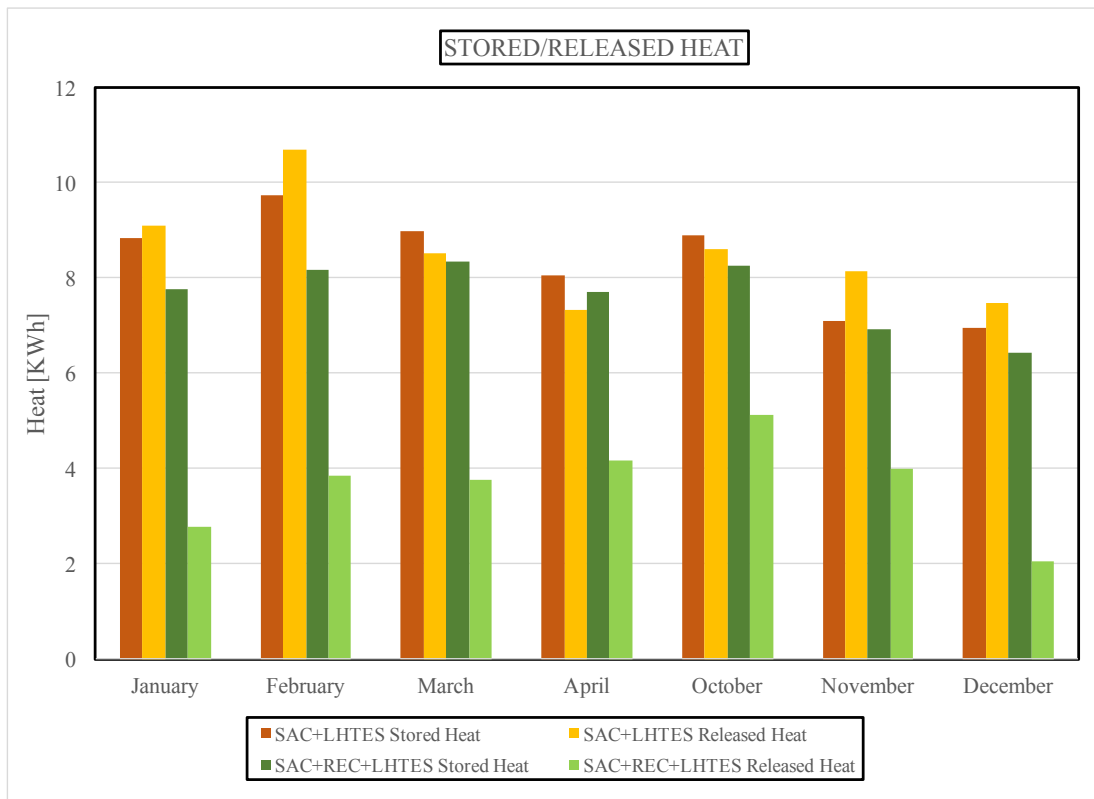


Figure 49. Stored and released heat either for the SAC+LHTES system and for the SAC+REC+LHTES system throughout the heating season.

February is characterized by the highest values of stored and released heat for the SAC+LHTES system and this is due to the coexistence of colder monthly air temperatures and at the same time of a greater frequency of sunny days, respect to the other cold months like January or December. Indeed, higher temperature differences help to exchange heat, both to store or release heat. On the other hand, the system with air recuperator maintained the monthly stored heat always lower than stored heat of the SAC+LHTS system but the difference is even more striking for the released heat because the recuperator makes heat being released from the storage even less

frequently. This is because with the addition of the recuperator it is more difficult to find LHTES unit inlet air temperature lower than that of the PCM. Indeed, the stored heat for the SAC+REC+LHTES system for the entire heating season of 53.6 KWh is about twice that of the released heat, differently from the SAC+LHTES system for which these two values are practically the same.

	SAC+LHTES		SAC+REC+LHTES	
	Stored heat	Released heat	Stored heat	Released heat
January	8.8	9.1	7.8	2.8
February	9.8	10.7	8.2	3.9
March	9.0	8.5	8.3	3.8
April	8.1	7.3	7.7	4.2
October	8.9	8.6	8.3	5.1
November	7.1	8.1	6.9	4.0
December	7.0	7.5	6.4	2.1
Heating season	58.6	59.9	53.6	25.7

Table 25. Stored and released heat in the storage in the second and third kind of system throughout the heating season.

To highlight how the total gained heat is distributed throughout the ventilation time it is important to distinguish the useful heat from the wasted heat. Table 26 shows the heat required, the useful heat and the coverage rate (illustrates also in the bar chart of Figure 50), in percentage, obtained by the ratio of the second for the first.

	Required heat [kWh]	Useful heat [kWh]			Coverage rate [%]		
		SAC	SAC+LHTES	SAC+REC+LHTES	SAC	SAC+LHTES	SAC+REC+LHTES
January	61.2	22.7	31.3	54.1	37%	51%	88%
February	46.2	24.4	33.2	43.4	53%	72%	94%
March	37.3	23.3	28.8	35.2	62%	77%	94%
April	23.3	18.9	22.5	23.2	81%	96%	99%
October	22.9	15.7	20.7	22.7	69%	91%	99%
November	41.3	16.0	22.8	37.4	39%	55%	91%
December	57.8	18.7	26.7	50.4	32%	46%	87%
Heating season	289.9	139.6	185.9	266.4	48%	64%	92%

Table 26. Useful heat and coverage rate throughout the heating season from all the 3 systems.

February showed the largest values of useful heat for all the systems: this confirmed what said for this month, composed of cold, but at the same time, more frequent sunny days. It is noticeable that there is always an increase by passing from the first to the second system and from the second to the third system and so, this implies real improvements both by adding the LHTES unit and the recuperator. The useful heat increases respectively from 139.64 KWh to 185.92 KWh (+33%) and from 185.92 KWh to 266.38 KWh (+43%) in the global heating season. Passing directly from the first to the third system the useful heat almost doubled. The useful heats and so the rates of coverage increase as the room supplied air temperature reaches at least or is close more frequently to 20°C and thus, they increase from colder to warmer months. The LHTES unit has mitigated the time mismatch between solar radiation availability and heat demand by storing excess solar energy and by releasing it subsequently.

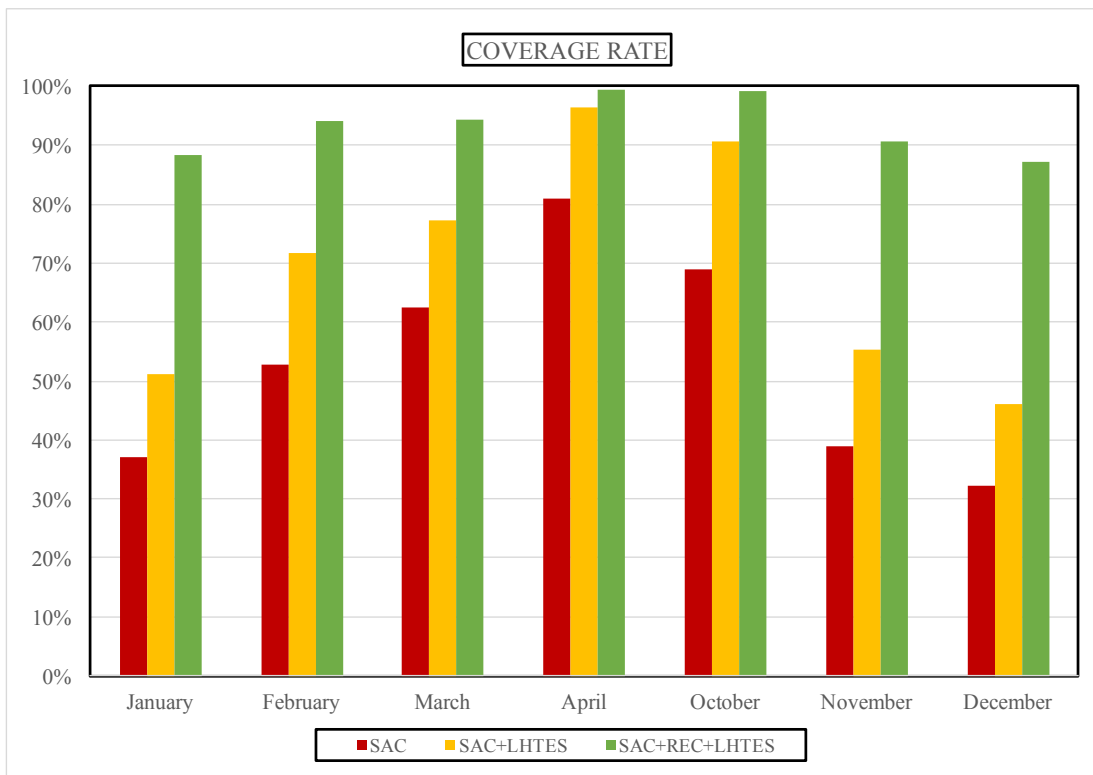


Figure 50. Monthly coverage rates for each system.

For this reason, the useful and rate of coverage are always higher in SAC+LHTES system respect to SAC system. The further addition of the recuperator recovered the

useful heat that otherwise would have been wasted to the external environment. Differently from the first two systems the third one maintains the rate of coverage high throughout the months passing from the lowest percentage of 87% in December to the highest one of 99% in April while, in the same months, the SAC system passes from 32% to 81% and the SAC+LHTES system from 46% to 96%.

In Table 27 the information about the total coverage time and the percentage of the total coverage time for each system and for each month of the heating season is given. To have a better visual idea, the total coverage time rates are shown in the bar chart of Figure 51. The general trend follow that of coverage rate of Figure 50 but differences from one month to another are more pronounced, in particular for the system with air recuperator. The latter differences are due to frequent supplied air temperature which is a little lower than the design room temperature of 20°C that keeps the useful heat close to the required heat but at the same time, even though the temperature is, for instance, 19°C is not sufficient to completely cover the ventilation losses and the time is not counted.

	Total coverage time [h]			Total coverage time rate [%]		
	SAC	SAC+LHTES	SAC+REC+LHTES	SAC	SAC+LHTES	SAC+REC+LHTES
January	48	61	91	19%	25%	37%
February	66	94	139	29%	42%	62%
March	116	166	184	47%	67%	74%
April	154	210	228	64%	88%	95%
October	131	201	230	53%	81%	93%
November	63	91	111	26%	38%	46%
December	41	50	78	17%	20%	31%
Heating season	619	873	1061	36%	51%	63%

Table 27. Total coverage time and total coverage time rate of the 3 systems.

Adding the LHTES unit the total coverage time throughout the heating season increased by 254 hours, from 619 hours to 873 hours with an increase of 40% while the total coverage time ratio increased from 36% to 51%. Further adding the recuperator, the total coverage time throughout the heating season increases by 442

hours (71% more) and by 188 hours (22% more) respectively for the SAC system and the SAC+LHTES system while the total coverage time rate reaches the 63%.

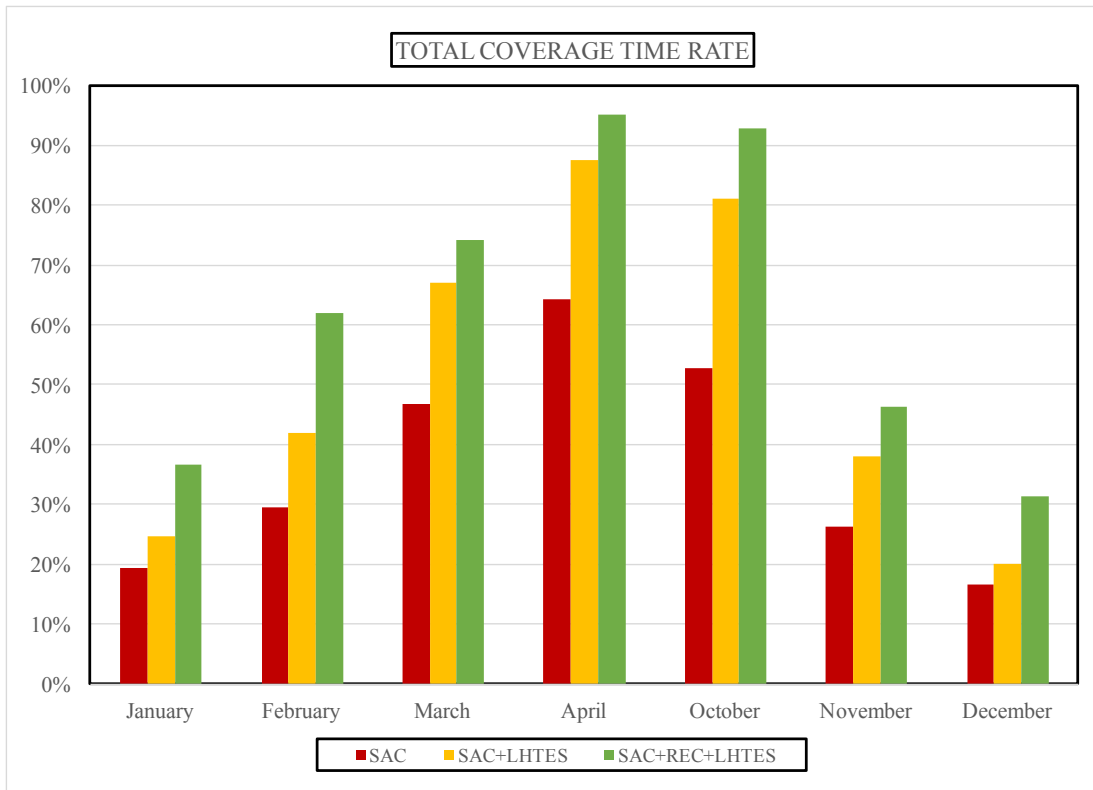


Figure 51. Monthly total coverage time rate for the 3 systems

What it is really important in the evaluation of the energy savings is the additional heat that the system would need to reach the design conditions of 20°C throughout the overall ventilation time. Figure 52 accurately shows the monthly additional heat required for each system and the values are listed in Table 28. A general positive impact by adding components to the basic system composed of only the SAC is noticeable. Firstly, by adding the LHTES the monthly additional heat needed decreases of about 8 KWh for most of the months except for April and October where the additional heat decreases of 3.6 KWh and 5 KWh, respectively. Considering the overall heating season, it decreased from 150.3 to 104.0 KWh and so the SAC+LHTES would need 31% of less external energy respect to the SAC system to reach the design conditions. Even higher differences are found by adding the recuperator, above all for the colder months. Indeed, in December, for instance, the additional heat decreases of

31.8 KWh (81% less) respect the SAC system and of 23.7 KWh (76% less) respect the SAC+LHTES system. The additional heat for the system with the recuperator is, in any case, very low in each month, reaching value practically negligible in April and October. In the entire heating season the SAC+REC+LHTES system would need only 23.6 KWh of additional energy, about 6 times less respect to the SAC system value and about 4.5 times less than the SAC+LHTES system value.

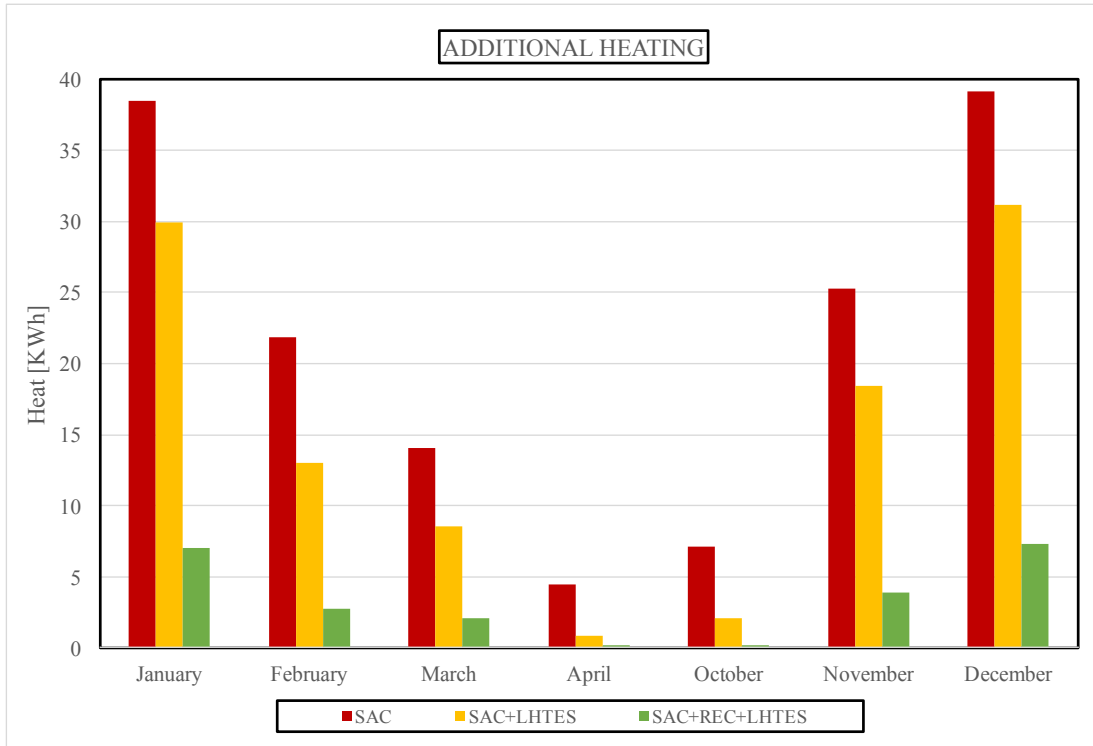


Figure 52. Monthly additional heat for each system.

	Additional Heat [kWh]		
	SAC	SAC+LHTES	SAC+REC+LHTES
January	38.5	29.9	7.1
February	21.8	13.1	2.8
March	14.0	8.5	2.1
April	4.5	0.8	0.2
October	7.1	2.1	0.2
November	25.2	18.4	3.9
December	39.2	31.1	7.4
Heating season	150.3	104.0	23.6

Table 28. Monthly additional heat for each system

In conclusion, in Table 29 the values of the electric energy consumed by Fan 1 and by Fan 2 (the latter associated only to the system with recuperator), the effectiveness and the global effectiveness in each month and in the overall heating season are reported. The different monthly fan 1 consumptions are due to different number of days in each month while the energy spent in each month for fan 2 are indicative of the recuperator usage, maximum in December and in January (1.3 KWh) and minimum in April (0.3 KWh). The overall usage of fan 2 is just over half of that of fan 1, sign of a recuperator usage of about half of the heating season overall ventilation time. The effectiveness and the global effectiveness of SAC+REC+LHTES system need to also take into account the energy required by fan 2, and thus are calculated with:

$$\varepsilon_{with\ rec.} = \frac{Q_{useful}}{E_{el.Fan1} + E_{el.Fan2}} \quad (3.22)$$

$$\varepsilon_{glob,with\ rec.} = \frac{Q_{vent}}{E_{el.Fan1} + E_{el.Fan2} + Q_{additional}} \quad (3.23)$$

	El. Energy [KWh]		Effectiveness			Global Effectiveness		
	Fan1	Fan2	SAC	SAC+LHTES	SAC+REC+LHTES	SAC	SAC+LHTES	SAC+REC+LHTES
January	1.6	1.3	14.3	19.7	19.0	1.5	1.9	6.2
February	1.4	1.0	17.0	23.1	18.2	2.0	3.2	8.9
March	1.6	0.8	14.7	18.1	15.1	2.4	3.7	8.4
April	1.5	0.3	12.3	14.6	12.4	3.9	9.8	11.5
October	1.6	0.6	9.9	13.1	10.4	2.6	6.2	9.6
November	1.5	1.1	10.4	14.9	14.2	1.5	2.1	6.3
December	1.6	1.3	11.7	16.8	17.5	1.4	1.8	5.6
Heating season	9.3	5.0	15.1	20.1	18.6	1.8	2.6	7.7

Table 29. Fan consumptions, effectiveness and global effectiveness.

The effectiveness grows by adding the LHTS unit to the SAC in each month with maximum value in February (17 for SAC system and 23.1 for SAC+LHTES system) and with a value throughout the heating season increased by 5.1 points. Adding the recuperator, the monthly effectiveness, respect to the SAC system, always increased except for November while the monthly effectiveness always decreased respect to

SAC+LHTES system. Instead, the global effectiveness rises by adding the LHTES unit and further the recuperator. The maximum and the minimum monthly values of the global effectiveness are recorded respectively in April and in December for all the 3 systems.

Chapter 4

Final conclusions

4.1 Conclusions.

Experimentations were performed on the system installed at the University of Ljubljana. The velocity depended mainly on the position along the duct cross section while a less evident dependence was recorded on air temperature. Even if both influences acted during measurements, by averaging the values a constant value of 1.3 m/s was assumed, to which correspond 10.27 l/s volumetric flow rate and 0.012 kg/s air mass flow rate. This mass flow rate guaranteed the maximum level of the ventilation system quality in relation to the standard requirements per person in a single office. The positive impact of the LHTS unit on the system was analyzed through measurements in a hypothetical ventilation time from 9 am to 5 pm. The results throughout the 5 days of measurements are summarized in Table 30.

			SAC	SAC+LHTES
From January 22 to January 26	Ventilation Losses [Wh]	Value	6013	6013
	Total heat gained [Wh]	Value	13084	12233
		+/- Δ(%)	/	-7%
	Useful heat [Wh]	Value	5390	5996
		+/- Δ(%)	/	+11%
	Coverage rate [%]	Value	90%	99%
	Total coverage time [h]	Value	27.7	36.0
		+/- Δ(%)	/	+30%
	Total coverage time rate [%]	Value	71%	92%
	Additional heat [Wh]	Value	622	17
+/- Δ(%)		/	-97%	

Table 30. Global results from measurements.

Even though the total heat gained globally decreased by 7% by adding the storage to the SAC, sign of a greater stored heat (2034 Wh) than the released heat (1470 Wh) in the LHTES unit, what is important is how this energy is used along in time. Indeed, the useful heat increased by 11% with the storage with a coverage rate of 99% against the 90% of the SAC system. Furthermore, the total coverage time rose by the 30% (8.3 hours more) with a total coverage time rate of 92% against the 71% of the SAC system. The introduction of the storage almost reduced to zero the additional heat of 622 Wh needed for the SAC system.

TNSYS software was used as a simulation tool of the investigated system. The validation of the LHTES unit and the SAC mathematical model was based on temperature measurements performed from November 30 and December 5. The simulation of the storage showed a good agreement with measurements with a MAE throughout the 6 days of only 0.9 °C and a maximum absolute error of 5.9 °C while worse results were achieved for the SAC with high absolute errors in correspondence of solar peaks with a maximum of 21.5 °C but despite this, the MAE maintained relatively low with a value throughout the 6 days of 4.4 °C. The annual simulations were performed by comparing three different systems: the first two were the same analyzed in the measurements (SAC and SAC+LHTES systems) and the third took into account the addition of an air recuperator with 80% effectiveness between the SAC and the LHTES unit. The overall results throughout the heating season (from October to April) are summarized in Table 31. The positive aspects are increasingly marked from SAC system by adding both the LHTES, firstly, and the recuperator, secondly. The total heat gained rose respectively by 3% and by 39%. The useful heat, from 139.6 KWh increased by 33% with the storage and almost doubled for the system with recuperator, reaching a coverage rate of 92%. The same conclusions applied for the total coverage time throughout the heating season of 619 hours guaranteed by the SAC system that reached 873 hours (+41%) and 1061 hours (+71%) respectively for the second and the third system. The SAC system reached at least 20°C the 36% of the overall heating season ventilation time, the SAC+LHTES system about half of the time and the SAC+REC+LHTES system the 63% of the time. The annual energy savings were identified on the decreasing of the additional heat of 31% (from 150.3 KWh to

104.0 KWh) by adding the storage, and on the striking decreasing of 84% (from 150.3 KWh to 23.5 KWh) by adding the recuperator and storage to the SAC.

		SAC	SAC+LHTES	SAC+REC+LHTES	
Heating season	Ventilation Losses [KWh]	Value	289.9	289.9	289.9
	Total heat gained [KWh]	Value	233.2	240.9	324.6
		+/- Δ(%)	/	+3%	+39%
	Useful heat [KWh]	Value	139.6	185.9	266.4
		+/- Δ(%)	/	+33%	+91%
	Coverage rate [%]	Value	48%	64%	92%
	Total coverage time [h]	Value	619	873	1061
		+/- Δ(%)	/	+41%	+71%
	Total coverage time rate [%]	Value	36%	51%	63%
	Additional heat [KWh]	Value	150.3	104.0	23.5
+/- Δ(%)		/	-31%	-84%	

Table 31. Global results from annual simulations.

In conclusion, the system composed of SAC and LHTES unit installed in Ljubljana provided an idea for intelligent usage of an inexhaustible, green and renewable energy source as the solar one. The problem of this source is its random and intermittent nature and thus the unbalance between energy supply and energy demand. The storage correctly helped to level this mismatch. This work has shown the usage of solar collector with latent storage for the purpose of office ventilation but other applications could be developed. Improvements and further studies of analogue systems could improve space heating through high energy savings and environmental issues, responding to the need of more efficient and sustainable energy systems.

REFERENCES

- [1] I. E. A. IEA, “Energy Efficiency Indicators Highlights (2017 edition),” *Int. Energy Agency*, p. 102, 2017.
- [2] H. Mehling and L. F. Cabeza, *Heat and cold storage with PCM: an up to date introduction into basics and applications*. 2008.
- [3] A. Sharma, V. V. Tyagi, C. R. Chen, and D. Buddhi, “Review on thermal energy storage with phase change materials and applications,” *Renewable and Sustainable Energy Reviews*, vol. 13, no. 2. pp. 318–345, 2009.
- [4] R. K. Sharma, P. Ganesan, V. V. Tyagi, H. S. C. Metselaar, and S. C. Sandaran, “Developments in organic solid-liquid phase change materials and their applications in thermal energy storage,” *Energy Convers. Manag.*, vol. 95, pp. 193–228, 2015.
- [5] A. Abhat, “Low temperature latent heat thermal energy storage: Heat storage materials,” *Sol. Energy*, vol. 30, no. 4, pp. 313–332, 1983.
- [6] B. Zalba, J. M. Marín, L. F. Cabeza, and H. Mehling, “Review on thermal energy storage with phase change: Materials, heat transfer analysis and applications,” *Applied Thermal Engineering*, vol. 23, no. 3. pp. 251–283, 2003.
- [7] L. F. Cabeza, H. Mehling, S. Hiebler, and F. Ziegler, “Heat transfer enhancement in water when used as PCM in thermal energy storage,” *Appl. Therm. Eng.*, vol. 22, no. 10, pp. 1141–1151, 2002.
- [8] J. Fukai, M. Kanou, Y. Kodama, and O. Miyatake, “Thermal conductivity enhancement of energy storage media using carbon fibers,” *Energy Convers. Manag.*, vol. 41, pp. 1543–1556, 2000.
- [9] A. Mills, M. Farid, J. R. Selman, and S. Al-Hallaj, “Thermal conductivity enhancement of phase change materials using a graphite matrix,” *Appl. Therm. Eng.*, vol. 26, no. 14–15, pp. 1652–1661, 2006.
- [10] S. Himran, A. Suwono, and G. A. Mansoori, “Characterization of alkanes and

- paraffin waxes for application as phase change energy storage medium,” *Energy Sources*, vol. 16, no. 1, pp. 117–128, 1994.
- [11] V. V. Tyagi and D. Buddhi, “PCM thermal storage in buildings: A state of art,” *Renewable and Sustainable Energy Reviews*, vol. 11, no. 6. pp. 1146–1166, 2007.
- [12] J. Paris, M. Falardeau, and C. Villeneuve, “Thermal storage by latent heat: A viable option for energy conservation in buildings,” *Energy Sources*, vol. 15, no. 1, pp. 85–93, 1993.
- [13] G. A. Lane, “Low temperature heat storage with phase change materials,” *Int. J. Ambient Energy*, vol. 1, no. 3, pp. 155–168, 1980.
- [14] M. M. Alkilani, K. Sopian, M. Alghoul, M. Sohif, and M. Ruslan, “Review of solar air collectors with thermal storage units,” *Renew. Sustain. Energy Rev.*, vol. 15, pp. 1476–1490, 2010.
- [15] A. Oliver, “Thermal characterization of gypsum boards with PCM included: Thermal energy storage in buildings through latent heat,” *Energy and Buildings*, vol. 48. pp. 1–7, 2012.
- [16] D. Feldman, D. Banu, and D. W. Hawes, “Development and application of organic phase change mixtures in thermal storage gypsum wallboard,” *Sol. Energy Mater. Sol. Cells*, vol. 36, no. 2, pp. 147–157, 1995.
- [17] E. M. Alawadhi and H. J. Alqallaf, “Building roof with conical holes containing PCM to reduce the cooling load: Numerical study,” *Energy Convers. Manag.*, vol. 52, no. 8–9, pp. 2958–2964, 2011.
- [18] K. Yanbing, J. Yi, and Z. Yinping, “Modeling and experimental study on an innovative passive cooling system - NVP system,” *Energy Build.*, vol. 35, no. 4, pp. 417–425, 2003.
- [19] U. Stritih and V. Butala, “Energy savings in building with a PCM free cooling system,” *Stroj. Vestnik/Journal Mech. Eng.*, vol. 57, no. 2, pp. 125–134, 2011.
- [20] K. Lin, Y. Zhang, X. Xu, H. Di, R. Yang, and P. Qin, “Experimental study of the thermal performance of under-floor electric heating system with shape-stabilized PCM plates,” *Gaojishu Tongxin/Chinese High Technol. Lett.*, vol. 15, no. 4, 2005.
- [21] S. O. Enibe, “Performance of a natural circulation solar air heating system with

- phase change material energy storage,” *Renew. Energy*, vol. 27, no. 1, pp. 69–86, 2002.
- [22] P. Thantong and P. Chantawong, “Experimental study of a solar wall collector with PCM towards the natural ventilation of model house,” in *Energy Procedia*, 2017, vol. 138, pp. 32–37.
- [23] A. E. Kabeel, A. Khalil, S. M. Shalaby, and M. E. Zayed, “Improvement of thermal performance of the finned plate solar air heater by using latent heat thermal storage,” *Appl. Therm. Eng.*, vol. 123, pp. 546–553, 2017.
- [24] Z. Y. Wang, Y. H. Diao, L. Liang, Y. H. Zhao, T. T. Zhu, and F. W. Bai, “Experimental study on an integrated collector storage solar air heater based on flat micro-heat pipe arrays,” *Energy Build.*, vol. 152, pp. 615–628, 2017.
- [25] A. E. Kabeel and K. Mečárik, “Shape optimization for absorber plates of solar air collectors,” *Renew. Energy*, vol. 13, no. 1, pp. 121–131, 1998.
- [26] A. A. El-Sebaei, S. Aboul-Enein, M. R. I. Ramadan, S. M. Shalaby, and B. M. Moharram, “Investigation of thermal performance of double pass-flat and v-corrugated plate solar air heaters,” *Energy*, vol. 36, no. 2, pp. 1076–1086, 2011.
- [27] E. Osterman, “Sistem z latentnim hranilnikom toplote za ogrevanje in hlajenje prostorov: doktorska disertacija,” Ljubljana, 2015.
- [28] M. Kofalt, “Nadgradnja sistema z latentnim hranilnikom toplote za ogrevanje in hlajenje stavb: diplomsko delo,” Ljubljana, 2016.
- [29] R. Kozelj, “Izboljšava prezračevanja z latentnim hranilnikom toplote; magistrsko delo,” Ljubljana, 2017.
- [30] U. Stritih *et al.*, “PCM thermal energy storage in solar heating of ventilation air—Experimental and numerical investigations,” *Sustain. Cities Soc.*, vol. 37, pp. 104–115, 2018.
- [31] S. Medved and C. Arkar, “Correlation between the local climate and the free-cooling potential of latent heat storage,” *Energy Build.*, vol. 40, no. 4, pp. 429–437, 2008.
- [32] “Test report according to EN 12975- 1:2006+A1:2010/EN ISO 9806:2013,” *Fraunhofer Inst. Sol. Energy Syst. ISE Freiburg, Ger.*, 2016.
- [33] E. Osterman, K. Hagel, C. Rathgeber, V. Butala, and U. Stritih, “Parametrical analysis of latent heat and cold storage for heating and cooling of rooms,” *Appl.*

- Therm. Eng.*, vol. 84, pp. 138–149, 2015.
- [34] S. A. Klein, W. A. Beckman, J. W. Mitchell, and J. A. Duffie, “TRNSYS Mathematical Reference,” *Trnsys 17*, vol. 4, p. 474, 2014.
- [35] S. N. Al-Saadi and Z. Zhai, “A new validated TRNSYS module for simulating latent heat storage walls,” *Energy Build.*, vol. 109, pp. 274–290, 2015.
- [36] E. Halawa and W. Saman, “Thermal performance analysis of a phase change thermal storage unit for space heating,” *Renew. Energy*, vol. 36, no. 1, pp. 259–264, 2011.
- [37] P. Charvát, L. Klimeš, and M. Ostrý, “Numerical and experimental investigation of a PCM-based thermal storage unit for solar air systems,” *Energy Build.*, vol. 68, no. PARTA, pp. 488–497, 2014.
- [38] Agencija Republike Slovenije za Okolje, “Podatki samodejnih postaj.” [Online]. Available: <http://www.meteo.si/met/sl/app/webmet>.

ACKNOWLEDGEMENTS

Firstly I would like to thank the University of Ljubljana that gave me the opportunity to carry out the research developed in this work and in particular Prof. Uros Stritih that was always available and the PhD student Rok Kozelj that supported me and followed me in the four months in Ljubljana.

I obviously want to thank my relator at Politecnico di Torino, Prof. Marco Carlo Masoero that was always available and answered promptly to my questions or doubts. I want to thank one of my best friends, Filippo De Grazia that motivated me to make the decision to study abroad. Now that I finished my experience abroad I am happy about the choice made less than one year ago.

Special thanks I want to make to my family, and in particular to my brother Giacomo, for all these years of study. I hope I can repay of all their efforts and sacrifices that they did to allow me to study.

I want to thank my group of friends in Torino, in particular Fabrizia Litterio, that the fate wanted us to meet exactly during our first day at Politecnico, and my special friends from Palermo, Federico Giuffrida and Alessandro Gagliano. With you the weight of the study was lighter and less stressful.

I can't forget to thank the best flatmate ever, Andriy Lavrynenko with whom I changed four times the flat in two years in Torino.

I want to thank all the new friends that I made during the short period in Ljubljana. You gave me even more reasons to travel in the future.

Lastly, a special thank goes to my grandpa Giulio and my grandmas Rossana and Teresa that always believed in me and this goal is also because of them.